

Nucleate boiling on passive and active flexible microstructured surfaces

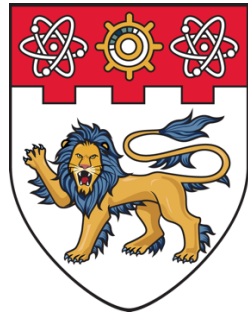
Nguyen, Thien Binh

2018

Nguyen, T. B. (2018). Nucleate boiling on passive and active flexible microstructured surfaces. Doctoral thesis, Nanyang Technological University, Singapore.

<https://hdl.handle.net/10356/88657>

<https://doi.org/10.32657/10220/45955>



**NANYANG
TECHNOLOGICAL
UNIVERSITY**

SINGAPORE

**NUCLEATE BOILING ON PASSIVE AND
ACTIVE FLEXIBLE MICROSTRUCTURED
SURFACES**

**NGUYEN THIEN BINH
SCHOOL OF MECHANICAL AND AEROSPACE ENGINEERING
2018**

NUCLEATE BOILING ON PASSIVE AND ACTIVE FLEXIBLE MICROSTRUCTURED SURFACES

by
NGUYEN THIEN BINH

School of Mechanical and Aerospace Engineering

A thesis submitted to the
Nanyang Technological University
in partial fulfilment of the requirements for the degree of
Doctor of Philosophy

January 2018

Abstract

Nucleate boiling is an efficient heat transfer process, which is crucial for numerous industrial applications such as cooling of electronic devices, spray cooling, mixing and cooling in nuclear power plant. Common methods to enhance the heat transfer rate in nucleate boiling, include modification of wettability and surface roughness using structured surfaces. While the physical mechanisms of boiling phenomena on smooth surfaces have been extensively investigated, studies of boiling processes on structured surfaces have been lacking, in particular on surfaces fabricated with passive structures such as micro-structures, nano-structures, and micro-nano hybrid structure, as well as on surfaces fabricated with active structures.

The first part of this thesis focuses on enhancement of boiling heat transfer using surfaces fabricated with passive nanopillars. The pillar length and surface area enhancement ratio were varied and demonstrated to correlate with the heat transfer coefficient of the boiling process. Furthermore, a predictive model of critical heat flux and critical temperature for boiling on such surfaces is proposed which shows that the predicted results are consistent with the experimentally measured ones.

The second part focuses on the dependence of convective boiling heat transfer on actuation of strip arrays fabricated on a surface. Actuation of the strip array as a novel method was introduced to dissipate the heat from the surface in a controllable way. By regulating the frequency of actuation, the heat flux through the surface can be controlled dynamically. Also, a model was derived which related the enhancement of convective heat transfer with the extra mass transfer rate caused by the array actuation. During the derivation, a new coefficient was proposed which represented for the extra mass transfer process, which can be used to further develop the model with different properties of actuators such as shape, stiffness or surface roughness.

The last part is an exploratory research on the nucleation, growth and detachment of individual vapour bubbles generated from a heated cavity with the present of a nearby actuated strip. It was proposed to fabricate on the heated surface an actuated strip and a micro-cavity with a precise position and size. The dynamics of the vapour bubble using high-speed imaging coupled with measurement of the local temperature on the heated surface using micro-sensors fabricated on the surface were studied. It was found that the actuation caused the bubble to oscillate around the cavity and to depart faster from the surface with a smaller departure diameter.

Acknowledgements

Firstly, I would like to express my sincere gratitude to my advisor Prof. Tran Anh Tuan and my co-supervisor Dr. Ng Sum Huan Gary of SIMTech for the continuous support of my Ph.D. study and related research, for their patience, motivation, and immense knowledge. Their guidance helped me in all the time of research and writing of this thesis. I could not have imagined having better advisors and mentors for my Ph.D. study.

Besides my advisors, I would like to thank the rest of my thesis committee: Prof. Claus-Dieter Ohl and Prof. Fei Duan, for their insightful comments and encouragement, but also for the hard questions which motivated me to widen my research from various perspectives.

I gratefully acknowledge the funding received towards my Ph.D. from the A*STAR research funding, Project ID 1425203142. I am also grateful to the funding received through the NTU Scholarship, Nanyang Technological University, Singapore to undertake my Ph.D.

I am grateful to my project collaborators in the Indian Institute of Technology Bombay and the University of Pittsburgh. In particular, I would like to thank Prof. Amitabh Bhattacharya and Prof. Paul W. Leu for their good advice and support on my project.

My sincere thanks also go to Dr. Yu Hao, Dr. Liu Dong Dong, Dr. Nabeel Rashin and Dr. Roberto Gonzalez, who provided me an opportunity to join the project, and to Mr. Yuan Kee Hock who gave access to the laboratory and research facilities. Without their precious support it would not be possible to conduct this research.

I thank my fellow laboratory mates for the stimulating discussions, for the sleepless nights we were working together before deadlines, and for all the fun we have had in the last four years.

Last but not the least, I would like to thank my family: my parents for supporting me spiritually throughout the writing of this thesis and my life in general.

Contents

Abstract	ii
Acknowledgements	iii
List of Tables	viii
List of Figures	ix
Nomenclature	xiv
Publications Arising from This Thesis	xvii
1 Introduction	1
1.1 Summary of aims and methods	4
1.2 Project motivation and objectives	4
1.3 Project scope	5
1.4 Thesis outline	6
2 Literature review	7
2.1 Qualitative description of nucleation process	8
2.1.1 Initial growth of a nucleate bubble	8
2.1.2 Growth and detachment of a nucleate bubble	9
2.2 Classical boiling heat transfer models	11
2.3 Numerical studies	14
2.4 Experimental studies	14
2.4.1 Investigation of surface temperature during bubble nucleation using micro-heaters and micro-sensors	15
2.4.2 Studies on nucleation site interaction and bubble coalescence.	17

2.4.3	Verifying microlayer thickness using laser interference	18
2.4.4	Studies on the effect of surface modifications to pool boiling	19
2.4.4.1	Surface wettability.	22
2.4.4.2	Surface morphological alternation with porous coatings.	23
2.4.4.3	Artificial fins and nano/microstructures.	26
2.5	Classification of boiling condition and general heating methods	29
2.5.1	Studies on boiling with different liquid temperature condition: saturated and subcooled boiling	29
2.5.2	Typical heating method and data correlation using in recent experimental approach.	30
3	Design and fabrication of experimental setup and components	33
3.1	Design and fabrication of the boiling rig	33
3.1.1	Boiling rig for pool boiling on passive nanostructured surface	34
3.1.2	Boiling rig design for boiling with actuated pillar and PIV	37
3.1.2.1	Design of reflex mirror	38
3.1.2.2	Design of magnetic field pattern	38
3.2	Design and fabrication of the microheater and microsensor	41
3.2.1	Design of the microheater	41
3.2.2	Design of the microheater integrated with microsensor	43
3.3	Fabrication of an array of actuators on silicon substrate	45
3.3.1	Array of single pillars	45
3.3.2	Array of Nickel strips	48
4	Heat transfer enhancement on passive nano-structured surfaces	50
4.1	Experiment procedure and data validation for pool boiling	50
4.1.1	Experimental scheme	50
4.1.2	Heat flux and wall superheat interpolation	52
4.1.3	Results on pool boiling validation	54
4.2	Properties of experimental substrates	55
4.3	Results and discussion.	58
4.3.1	Experimental result and observations	58

4.3.2	Mechanism of heat transfer enhancement on nanopillar substrates.	62
4.3.3	Prediction of critical heat flux temperature on nanopillar substrates	67
5	Study of heat transfer enhancement on actuated strip arrays	70
5.1	Experimental setup and procedures	71
5.2	Experimental substrate and actuation scheme	73
5.3	Results and discussion	75
5.3.1	Experimental result	75
5.3.2	Proposed model for convective heat transfer on actuated structure	78
5.3.3	Non-dimensional relationship of heat transfer process and actuation of strips array.	82
5.4	Summary	85
6	Experimental study of bubble nucleation on a microheater	86
6.1	Hydrodynamic behaviour of a single bubble nucleated on a microheater	87
6.1.1	Experimental setup and procedures	87
6.1.2	Results and discussion on nucleation of individual vapour bubble	88
6.2	Dynamic heat flux and wall temperature beneath a nucleate bubble .	94
6.2.1	Experimental setup and procedures	94
6.2.2	Results and discussion	95
6.3	Hydrodynamic behaviour of a nucleate bubble interacted with actuated strip	100
6.3.1	Experimental setup and procedures	100
6.3.2	Results and discussion	102
7	Conclusions and future work	109
7.1	Conclusions	109
7.1.1	Nucleate boiling on passive nanopillar structured substrate. .	109
7.1.2	Convective heat transfer on actuated Nickel strips-array. . . .	110
7.1.3	Nucleation of individual vapour bubbles on microheater and microsensor.	111

7.2	Future work	112
7.2.1	Further analysis on nucleate boiling on nanopillars array by varying more parameters of the structure.	112
7.2.2	Design actuators with varied shape, size and surface roughness	112
7.2.3	Velocity field measurement using PIV	113
	References	115
A	Fabrication of passive nanopillar array on test substrate	133
B	Validation of pool boiling data	135
C	Uncertainty analysis for heat flux and wall temperature	136
D	Bubble departure diameter and releasing frequency at the onset of nucleate boiling	139
E	Nanostructure sizes	140
F	Relation between the critical heat flux q_c and the spreading velocity v_s	141
G	Extra experiment to measure spreading velocity v_s on heated sub- strates	142
H	Uncertainty analysis for heat flux in heat loss measurement	144
I	Numerical verification for the method used to estimate heat loss	146
I.1	Method used to estimate heat loss.	146
I.2	Numerical method to validate heat loss calculation	147
J	Sputtering processes used to fabricate microheater	150
K	Fabricating of the microcavity	152

List of Tables

2.1	Summary of pool boiling on modified surface.	19
3.1	Technical specifications for microheater.	43
3.2	Technical specifications for microheater and microsensor.	43
3.3	Summary on the micro-heater/sensor design.	45
4.1	The physical properties of components in the boiling rig.	54
4.2	Surface area enhancement ratio r calculated for each substrate.	57
5.1	Actuated mode used in the experiment, the angular amplitude is kept almost constant with varied frequency.	74
E.1	Size of samples in the experiment with surface area enhancement ratio r calculated for each sample.	140

List of Figures

1.1	A typical boiling curve with three main regimes.	3
2.1	Nucleation at a base cavity.	8
2.2	Bubble growth and detachment.	9
2.3	The balancing between buoyancy force and surface tension force on a vapour bubble.	10
2.4	Mechanisms of heat transfer in nucleate boiling.	11
2.5	Bubble heat transfer mechanism suggested by Mikic and Rohsenow.	12
2.6	Single FC72 bubbles growing on a surface.	15
2.7	Location of the 16 sensors of the silicon substrate.	16
2.8	Types of direct bubble – bubble interaction.	17
2.9	The process of measuring of microlayer thickness and value of micro- layer measured for ethanol and water.	19
2.10	Sample of a laser-made biphilic pattern on a stainless-steel foil.	22
2.11	Photo-induced superhydrophilicity.	23
2.12	Shape of the honeycomb porous plate.	23
2.13	(a) Unit cell representation of the structure. (b) Fabricated structures with different size of unit cell.	24
2.14	(a) Stable and (b) Unstable boiling pattern.	25
2.15	(a) ZnO on Al and (b) ZnO on Cu structures.	25
2.16	Copper test sections with cavities.	26
2.17	Test substrate with micro cavities, copper porous pillars and combi- nation of copper porous pillars with nano-porous coating.	27
2.18	Bi-conductive surfaces to tailor spatial variations in surface temper- ature.	28

2.19	Structured surface and methodology of boiling experiments in Dhillon study.	28
2.20	Pool boiling is classified as saturated and subcooled boiling (a) Saturated and (b) Subcooled pool boiling.	30
2.21	Heating method and measurement of q'' and ΔT_{sat}	31
3.1	Scheme to estimate the heat loss to the surrounding environment. . .	34
3.2	Design of the boiling rig for passive pool boiling experiment.	35
3.3	Wall-rig part was manufactured by stainless-steel.	36
3.4	The second design of the boiling rig for boiling experiment with actuated pillar and PIV.	38
3.5	Incident beam and area of interest (4×4 mm).	39
3.6	Magnetic field direction of two cases: with and without permanent magnet.	40
3.7	Arrangement of electromagnet (horizontal changing field) and permanent magnet (vertical static field).	41
3.8	Structure of microheater - first design.	42
3.9	Structure of microheater/sensor - second design.	44
3.10	Young Modulus E depend on the ratio Crosslinker:PDMS.	46
3.11	Setup to locate the array of nickel pillars on silicon substrate.	47
3.12	A sample of nickel arrays on silicon substrate.	47
3.13	The fabrication of an array of Nickel strips.	49
4.1	The schematic of boiling set up experiment.	51
4.2	The schematic of parameter controlling and measurement.	52
4.3	Heat flux measurement.	53
4.4	Boiling curve of bare silicon with Zuber and Rohsenow models. . . .	55
4.5	SEM images showing nanopillar substrates of different pillar heights l and corresponding surface area enhancement ratio r	56
4.6	Total effective enhancement area A_1	56
4.7	Properties and surface area enhancement ratio r of four substrates. .	58
4.8	Representative snapshots showing boiling phenomenon on the smooth substrate and the nanopillar substrate with $l = 1390$ nm at several surface temperatures T	59

4.9	Heat flux q versus wall superheat ΔT for smooth and nanopillar substrates.	60
4.10	Dependence of critical heat flux, CHF temperature, and Leidenfrost temperature on r	62
4.11	Schematics showing similarities between the rewetting process in pool boiling and the spreading process from a capillary, in particular at the three-phase contact line	64
4.12	Critical heat flux temperature T_c predicted versus the measured values for different substrates	69
5.1	Measured parameters and arrangement of experimental setup.	71
5.2	Scheme of periodic signal supplied from the electromagnet and arrangement of high speed camera.	72
5.3	Substrate with array of Nickel strips and characteristic parameters.	73
5.4	Experimental observation of different case of wall temperature and actuated frequency.	75
5.5	Heat flux q in relation with actuated frequency f and wall temperature T	76
5.6	Relation between liquid temperature T_l and actuated frequency f	77
5.7	Control volume for heat transfer across the bulk liquid.	79
5.8	Data collapses and shows the relation between the enhanced thermal properties of the system and the improved mass transfer rate.	81
5.9	Relation between Nu and Gr in the passive case.	82
5.10	Relation between Nu and $Re^{1/2}$ for different non-zero actuation frequencies f . The dashed line indicates the scaling $Nu \sim Re^{1/2}$	83
5.11	(a) Relation between $Nu/Re^{1/2}$ and $Gr^{1/4}/Re^{1/2}$. The dashed line indicates $C_{Re} + C_{Gr}Gr^{1/4}/Re^{1/2}$, where C_{Re} and C_{Gr} are obtained via a least squares fit of the data; (b) $Nu/(C_{Re}Re^{1/2} + C_{Gr}Gr^{1/4})$ vs $Gr^{1/4}/Re^{1/2}$	84
6.1	Experimental setup to used study nucleate boiling	87
6.2	Representative snapshots and results of a bubble nucleated	90
6.3	Bubble diameter D_b as a function of the heating time t_h , for different values of power per unit area P	91

6.4	Dependence of delay time t_d , departure diameter D_b , and departure frequency f_d , on the average temperature of the substrate.	93
6.5	Experimental setup with two microsensors embedded on top and bottom side of the substrate, the space surrounding the cuvette is partial vacuum to ensure thermal insulation.	94
6.6	Representative snapshots of a bubble nucleated on top of the microsensor at average surface temperature of 68.1 °C.	95
6.7	Dynamic local heat flux and wall temperature beneath a nucleate bubble at average surface temperature of 68.1°C.	96
6.8	Definition sketch for a bubble rising in saturated bulk liquid, ϕ is the velocity potential of the flow surrounding the vapour bubble.	98
6.9	(a) Schematic drawing of the boiling rig and (b) dimension of substrate and actuators. (c) A snapshot of bubble nucleated from the cavity with the presence of the strip in passive case.	101
6.10	Representative snapshots of a bubble nucleated with the present of an actuated strip ($f = 30$ Hz and $\alpha = 30$ degree). The average surface temperature is close to boiling point of FC72 (56.3°C)	102
6.11	(a) Dependence of departure diameter D_b and strip frequency f for different angular amplitude. (b) Dependence of departure frequency f_d and strip frequency f for different angular amplitude.	103
6.12	A schematic drawing of forces act on the vapour bubble with the presence of an actuated strip during its growing cycle.	105
6.13	A plot of ratio $r_c = D_a \sin(\alpha_t) / F_b$ shows the contribution of drag force to the upward force over one cycle of actuation. The negative value means the opposite direction of D_a	107
7.1	PIV image recorded for 10 Hz actuated pillar. The result is shown for rigid pillar (top) and soft pillar (bottom).	113
7.2	One frame of PIV recorded for 10 Hz actuated pillar. The result is in vorticity (1/s), shear stress and velocity.	114
A.1	The fabrication steps of silicon nanopillar pattern.	133
C.1	Relative uncertainty calculated for heat flux (a) and wall temperature (b) at boiling regime.	138

D.1	Dependence of bubble departure diameter and releasing frequency on the height of nanostructures at the onset of nucleate boiling. For the smooth surface, $l = 0$. the departure diameter tends to be smaller for structured surfaces, while there is a significant jump in bubble releasing frequency from the smooth surface to the nanostructured surfaces.	139
F.1	Linear relation between the critical heat flux q_c and the spreading velocity vs highlighting that the spreading velocity could be used as a key parameter for predicting the critical heat flux for non-polar dielectric fluids with low surface tension, e.g., FC-72.	141
G.1	Experiment setup to measure spreading velocity v_s on heated substrates	142
H.1	Relative uncertainty calculated for heat flux q_{12} for all substrates at boiling regime.	145
I.1	Schematic drawing of the model: heat fluxes q_{12} and q_{23} are calculated on the shaded area A , whereas the heat loss q_{loss} is considered on four wall area A_s between the shaded area.	146
I.2	3D model of the copper rod with boundary conditions.	148
I.3	Simulation result at critical heat flux condition for bare silicon ($q = 15 \text{ W}\cdot\text{cm}^{-2}$, $T = 100 \text{ }^\circ\text{C}$) (a) Temperature distribution on the copper rod; (b) Temperature along the centre line of the copper rod with highlighted T_1 T_2 and T_3	148
I.4	Validation results for FC-72 on bare silicon substrate: heat loss of simulation model is plotted with heat loss calculated by tested method for various heating temperature.	149
J.1	Sputtering processes used to fabricate microheater.	151
K.1	Etching processes used to fabricate micro-cavity.	152

Nomenclature

Acronyms

CHF Critical Heat Flux

FC-72 Perfluorohexane

ICP/RIE Inductively Coupled Plasma Reactive Ion Etching

PDMS Polydimethylsiloxane

TCL Three-phase Contact Line

Greek Symbols

α Angular amplitude, radian

μ Dynamic viscosity, Pa·s

Ω Volume rate of liquid evaporated at three-phase contact line, $\text{m}^3 \cdot \text{s}^{-1}$

ρ Mass density, $\text{kg} \cdot \text{m}^{-3}$

σ Surface tension, $\text{N} \cdot \text{m}^{-1}$

θ Contact angle of FC-72 on silicon surface, degree

ξ Effective mass transfer ratio

Roman Symbols

ΔT Superheat temperature, K

Δx Thickness of thermal resistance layer, m

C_p Specific heat, $\text{J} \cdot \text{kg}^{-1} \cdot \text{K}^{-1}$

C_{sf}	Rohsenow experimental coefficient
D_b	Departure diameter of single bubble, mm
f	Actuated frequency, Hz
f_d	Bubble releasing frequency, Hz
g	Acceleration of gravity, $\text{m}\cdot\text{s}^{-2}$
h_{fg}	Latent heat of evaporation, $\text{J}\cdot\text{kg}^{-1}$
K	Coefficient of Zuber's model, $K = 0.131$
k	Thermal conductivity, $\text{W}\cdot\text{m}^{-1}\cdot\text{K}^{-1}$
l	Height of nanopillar, nm
m	Power index of Rohsenow model, $m = 0.33$
n	Power index of Rohsenow model, $n = 1.7$
P	Input flux, $\text{MW}\cdot\text{m}^{-2}$
p	Pitch between nanopillars, nm
q	Heat flux through the substrate surface, $\text{W}\cdot\text{cm}^{-2}$
q_c	Critical heat flux, $\text{W}\cdot\text{cm}^{-2}$
R	Total thermal resistance, $\text{K}\cdot\text{m}^2\cdot\text{W}^{-1}$
r	Surface area enhancement ratio
T	Substrate surface temperature, $^{\circ}\text{C}$
T_{sat}	Saturation temperature of a liquid at atmospheric pressure, $^{\circ}\text{C}$
t_d	Delay time, s
v	Spreading velocity of liquid on test surface, $\text{mm}\cdot\text{s}^{-1}$
V_c	Total volume of one cycle movement of actuated strip, m^3
V_e	Effective volume of one cycle movement of actuated strip, m^3

Superscripts

n Nanopillar substrate

s Smooth substrate

Subscripts

b Boiling

C Boiling critical point

c Copper

ca Capillary

d Dry

g Glue

h Heating

L Leidenfrost point

l Liquid

n Natural convection

p Projected

r Room condition

S Spreading

s Silicon

v Vapour

w Substrate surface

Publications Arising from This Thesis

A) Publications with peer review process

1. T. B. Nguyen, D. Liu, M. I. Kayes, B. Wang, N. Rashin, P. W. Leu, T. Tran. Critical heat flux enhancement in pool boiling through increased rewetting on nanopillar array surfaces. *Scientific Reports*, 6, 2018.
2. H. Yu, T. B. Nguyen, S. H. Ng, T. Tran. Mixing control by frequency variable magnetic micropillar. *RSC Advances*, 6(14):11822-11828, 2016.

B) Conference

1. T. B. Nguyen, N. Rashin, H. Yu, T. Tran. Experimental study of vapour bubbles in nucleate boiling. *The International Workshop on Nanoscience and Nanotechnology: Opportunities for Academia and High Tech Industry Joint 4th Asia-Pacific Chemical and Biological Microfluidics Conferences*. Danang, Vietnam, November 2015.

Chapter 1

Introduction

Boiling is a natural phenomenon that takes place when a liquid is heated to its saturation temperature. One of the most common situations for boiling to occur is when a liquid comes into contact with a heated surface with temperature sufficiently higher than the liquid's saturation temperature. Boiling can be considered as the most efficient heat transfer method, due to its main mechanism to remove heat is latent heat, which is essential higher than other heat transfer process such as conduction or force convection. It allows to reduce size and volume of heat exchanger devices and enhance the operating performance of thermal element in industry and power plants. Therefore, boiling plays a crucial and increasingly important role in various industrial applications, especially in energy production such as power plane, nuclear reactor, automotive engine cooling, steel industry, metallurgy and electronics cooling [1, 2].

A cooling system using boiling process can be very flexible in practical. It can handle very high heat fluxes, as in a nuclear reactor, where the heat flux needed to remove up to 10–15 MW/m². Also, it works well with electrical devices, which need to operate at moderate heat flux and low surface temperature (below 80 °C). One of the most important application of nucleate boiling is the cooling system encountered in nuclear facilities. Inside the nuclear reactors, nucleate boiling occurs at significant flow rates through the reactor. The vapour bubbles are taken away from the heat transfer surface and are carried along the liquid flow. Moreover, the nucleate bubble at the surface effectively disrupts the stagnant liquid layer and therefore significantly improves the heat transfer process from hot surface to bulk fluid.

Nowadays, boiling can be found in more and more applications, which is previ-

ously the field of other heat transfer process such as conduction or force convection. One example of the development of boiling application is in the field of modern automotive design. The traditional design concepts for engine cooling are almost depended on force convection, which may not enough for the new engine to operate at its maximum load conditions. In a recent study, Steiner *et al.* suggested a combination system, in which the cooling mechanism can be switched from convection to nucleate boiling depend on the engine loading [3].

The cooling application of nucleate boiling can also be used in the heat exchange equipment in extreme environments such as deep ocean and space. National Aeronautics and Space Administration (NASA) have recently started the project Nucleate Pool Boiling eXperiment (NPBX) to investigate heat transfer process and bubble hydrodynamic in microgravity. This data is very important to optimize the design of heat exchange equipment in submarine or in the spaceship.

Due to the development of dielectric coolant liquid, boiling can be applied safely in cooling application of electrical devices, which require relative low operation temperature (usually not higher than 80 °C). Liquid cooling for electrical devices can be either convective cooling through a heat pipe system as in a gaming PC or immersion cooling for large data centres, in which nucleate boiling directly occurs on the hot surface of the target chipset.

Another application of nucleate boiling is the thermal inkjet print head. Thermal inkjet technology uses heat to eject a thin jet of ink from the print head to the substrate. A microscopic heater is put inside the ink chamber and is close to the print nozzle. Once it is activated, a vapour bubble will be nucleated and expands rapidly in a very short duration, causing the ink to explode onto the paper.

Despite its importance in such engineering applications, the lack of understanding of the mechanistic mechanism of the boiling phenomenon leads to inefficient utilisation of boiling in such applications. [4] Situations in which boiling occurs can be broadly classified into two categories: flow boiling and pool boiling. In the former case, the boiling liquid is forced to move along a hot solid surface, whereas in the latter case, the liquid is heated by a hot surface and forced into motion by natural buoyancy [1, 2].

In order to obtain better insight and physical understanding of the boiling process and how it depends on contributing factors such as temperature, liquid, and solid

properties, numerous boiling experiments consisting of a heated surface surrounded by a stationary liquid have been carried out. Several different boiling regimes with distinct hydrodynamic and thermal behaviours have been identified: pure convective, nucleate boiling, transition boiling, and film boiling. Typically, these regimes are characterised using a boiling curve, which is the relation between the surface heat flux q and the surface superheat (Figure 1.1). Here the surface superheat is defined as $\Delta T = T - T_{sat}$, where T and T_{sat} are the surface temperature and saturation temperature of the liquid, respectively.

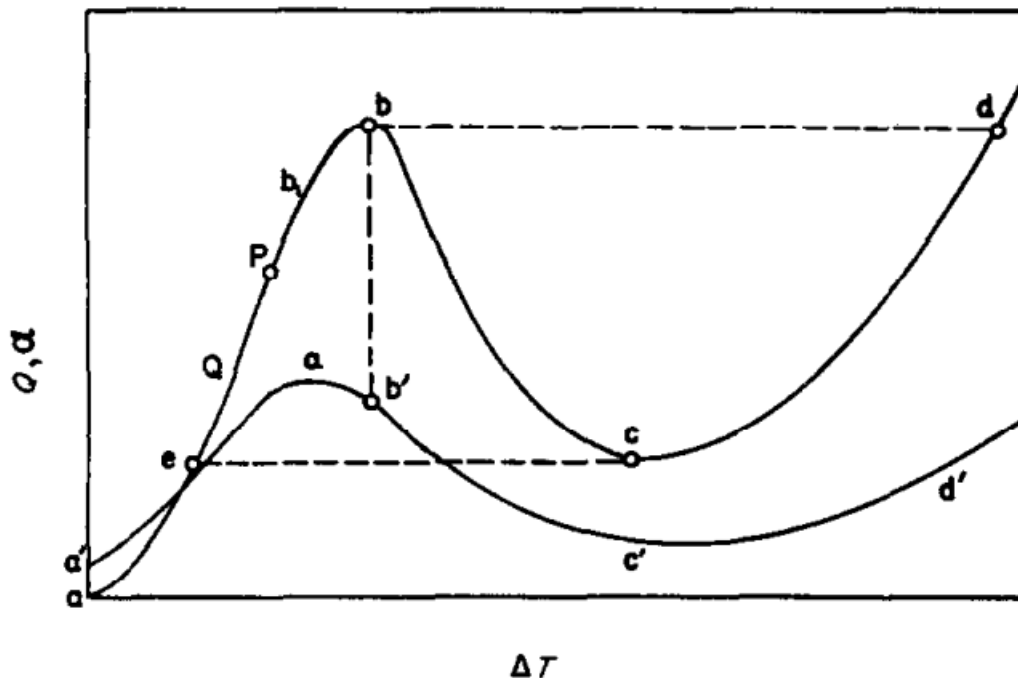


Figure 1.1: The original boiling curve by Nukiyama: $Q - \Delta T$ ($abcd$) curve with four main regimes: pure convection (close to point a), nucleate boiling (from a to b), transition boiling (from b to c) and film boiling (from c to d). The second curve in this plot ($a'b'c'd'$) shows the relation of the corresponding heat transfer coefficient α and surface superheat ΔT [5].

Based on the boiling curve, there are two important parameters normally used to measure the pool boiling performance: critical heat flux (CHF) and heat transfer coefficient (HTC). CHF is the maximum heat flux that a surface can transfer to a boiling liquid before the individual bubbles coalesce into an insulating vapour layer

and determines the maximum power density that could be handled by a boiling heat transfer device. HTC can be defined as the ratio of the heat flux to the difference between the surface temperature and the saturation temperature of the liquid and hence it describes the thermodynamic efficiency of the boiling exchange [1, 6].

1.1 Summary of aims and methods

The consensus of numerous investigations on boiling heat transfer is that transient conduction and micro-convection are the most dominant mechanisms of heat dissipation from a heated surface. Thus, enhancement of the heat transfer rate, which is the main goal of most practical applications, can be achieved by improving the transient conduction mechanism, in particular by using different types of porous materials to modify the surface properties. Nonetheless, heat transfer enhancement using micro-convection has not been fully explored. The project's aim is therefore to improve the heat transfer rate in the boiling processes with the focus on the enhancement of the micro-convection mechanism. This can be done by using actuated flexible structures fabricated on the heated surface.

To achieve this objective, there are several major steps that need to be conducted. The first one includes design, fabrication, and calibration of a boiling rig that enables measurement of the heat flux across the heated surface. This rig should also be integrated with a mechanism to actuate the flexible structure. The second step consists of design, fabrication and calibration of a micro-heater on top of the substrate. This allows precise control temporally and spatially of the nucleation of a vapour bubble. In the third step, active or passive flexible microstructures are to be fabricated on top of the boiling surface. The performance of the modified surfaces in nucleate boiling heat transfer will be evaluated thereafter using the boiling rig.

1.2 Project motivation and objectives

Electronic cooling is one of many technological applications that require effective heat removal at relatively low surface temperature. This is because electronics components can properly operate only if the temperature does not exceed 70°C. Traditional heat removal methods, either single phase or two-phase cooling ones,

have been relying on passive means such as surface enhancement or modification of the cooling liquid. Active methods such as forced cooling might require excessive power consumption and space to install the necessary components such as fans or pumps, which is a significant drawback to its enhancement on heat transfer efficiency.

The main objective of the proposed project is to develop an understanding of the hydrodynamics, heat transfer, and phase change of the nucleate boiling process, which includes nucleation, growth, detachment or possible collapse of an individual vapour bubble, on a controlled surface fabricated with magnetically-actuated (passive/active) flexible micro-structures. This understanding will then be used to pinpoint the parameter range for which the heat transfer rate from the surface is maximised for a given surface temperature

By introducing a novel element into the boiling process, namely, passive/active flexible micro-structures, the aim is to enhance either the mixing in the thermal boundary layer adjacent to the surface or the mass transferring inside the liquid body, and therefore the heat transfer rate. This relies on the fact that the heat transfer rate due to nucleate boiling on smooth surfaces is generally dominated by the micro-convection induced by the dynamics of vapour bubbles. Active actuation of the micro-structures, as well as elasto-capillary effects, provide extra mechanisms to induce micro-convection, thus potentially enhance the heat transfer rate, especially for applications that need to be operated at moderate temperature.

1.3 Project scope

This study focuses on the mechanism of boiling heat transfer on passive and active micro-structured surfaces. The scope will be included with multiple tasks:

- (i) Design and build boiling rigs for the experiments.
- (ii) Design and fabricate of microheater and microsensor on boiling surfaces.
- (iii) Fabricate actuated strip or pillar array onto the substrate surface.
- (iv) Conduct the experiments on passive and active substrate.
- (v) Discuss and analyse the results to better understand the mechanism of the boiling phenomenon.

1.4 Thesis outline

The report comprises seven chapters, namely, introduction, literature review, design and fabrication of experimental setup and components, the three chapters with experimental methods and results and finally conclusions and future work.

In the chapter *Literature review*, we will explore in detail reported investigations relevant to the study of nucleate boiling on active and passive flexible microstructured surfaces. First, detailed description of evolution of vapour bubbles formed on the heated surface will be provided. This will be followed by descriptions of various theoretical models and numerical simulations on mechanisms such as transient conduction, contact line heat transfer, and microlayer evaporation. Experimental conditions and measurement techniques will also be presented in sufficient detail. These includes heating and sensing methods, boiling data using liquid crystal, microlayer evaporation, effects of surface modifications, bubble coalescence, and saturated and subcooled boiling. A summary of recent experimental study on boiling enhancement using various surface modification methods will also be provided.

The chapter *Design and fabrication of experimental setup* will provide detailed description of the design of the experimental setup. It consists of design and fabrication of boiling rig, microsensor, microstructures and actuated structures. This chapter will explore these manufacturing techniques and will present the effort made in various stages of fabrication process.

In next three chapters *Experimental methods and results*, we will discuss various experimental conditions, methodologies, and results. This chapter consists of data validation of the boiling rig and measuring method, tests on the operation of micro-heater to induce a single bubble with a power pulse, experimental study of vapour bubbles in nucleate boiling in ethanol, a predictive model of CHF and critical temperature of the nanopillar substrates (passive) and a model of heat transfer enhancement due to extra-convective on actuated flexible structures.

Finally, the chapter *Conclusion and future work* will present main conclusions from the presented studies and future works.

Chapter 2

Literature review

Nucleate boiling is an effective heat transfer process that takes place when the rate of heat transfer across a heated surface to the surrounding liquid is below the critical heat flux (CHF). This complex phenomenon comprises various physical processes such as transfer of mass, momentum, energy, and phase transition during evolution of vapour bubbles that are formed on the heated surface [4]. In this chapter, we will provide an overview of the boiling process and related studies in three main sections.

First, we would like to introduce a qualitative description of the nucleation process, which will give us a fundamental understanding on the hydrodynamic behaviour of an individual vapour bubble such as initial growth, growth and detachment process. This section provides important information on cavity properties, pressure condition and critical diameter of a vapour bubble.

In the next section, we will introduce three classical models of boiling heat transfer on smooth surface, which is used as the initial assumption in most of recent studies. These models include transient conductive, contact line heat transfer and microlayer heat transfer.

The last section will provide the overview of recent studies on boiling heat transfer. We will review the recent experimental studies in multiple aspects such as experimental approach, measuring methods, substrate fabrications and the new proposed mechanism of each approaching respectively.

2.1 Qualitative description of nucleation process

2.1.1 Initial growth of a nucleate bubble

The process of inducing an individual bubble from a heated surface typically involves a micro-scale cavity on the surface and a liquid-vapour interface inside the cavity (see Figure 2.1). At the beginning, subcooled liquid enters the cavity and forms an interface between the cool liquid and trapped air. This liquid-vapour interface is stabilised when the vapour pressure P_g is less than the system pressure P_0 . The pressure difference between P_g and P_0 is known as the Laplace pressure and can be used to estimate the curvature R of vapour bubble:

$$\Delta P = P_g - P_0 = \frac{2\sigma}{R} \quad (2.1)$$

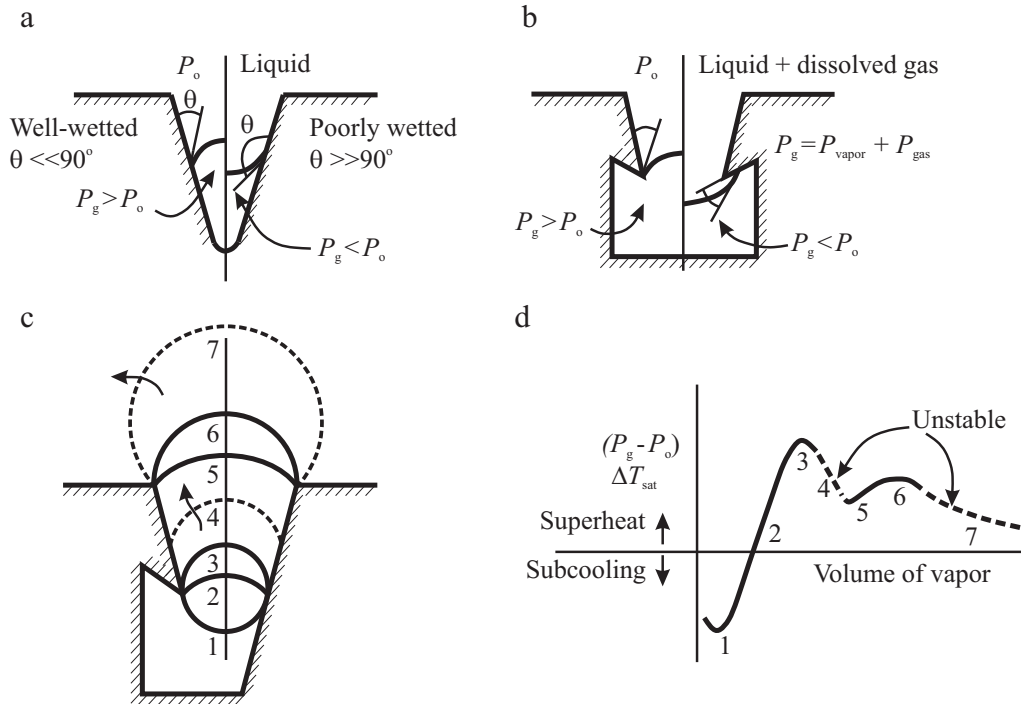


Figure 2.1: Nucleation at a base cavity [7].

The contact angle between the cavity surface and this interface layer depends on the wettability of the cavity surface. For a poorly wetted surface, the contact angle will be larger than 90° (Figure 2.1a). Reversal of inter-facial curvature when θ is

much less than 90° requires a re-entrant geometry (Figure 2.1c). When the cavity surface is heated, the vapour pressure inside the cavity increase gradually until the curvature of vapour-liquid interface reverses (contact angle $\theta > 90^\circ$). At this point, the trapped vapour become unstable to growth by evaporation and the growth of the vapour is faster until a visible bubble emerges from the cavity (Figure 2.1b).

At some point during the growth of bubble from the cavity, the local surface temperature fluctuates and makes the bubble's growth rate unstable. This is due to the fact that heat from the superheated surface is lost to the vapour bubble causing it to expand and the local surface temperature to temporarily decrease.

2.1.2 Growth and detachment of a nucleate bubble

Once a bubble emerges from the cavity, it grows continuously to reach a time dependent radius, $R(t)$ in the form of a hemisphere (Figure 2.2). It is noted that the hemisphere is partly separated from the superheated surface by a thin layer of liquid. This layer, which is typically called microlayer, grows almost linearly with the radius of the bubble until it reaches the value ranging from a few microns for small, fast-growing bubbles to tens of microns under slow-growing bubbles in pool boiling at low surface superheat [7].

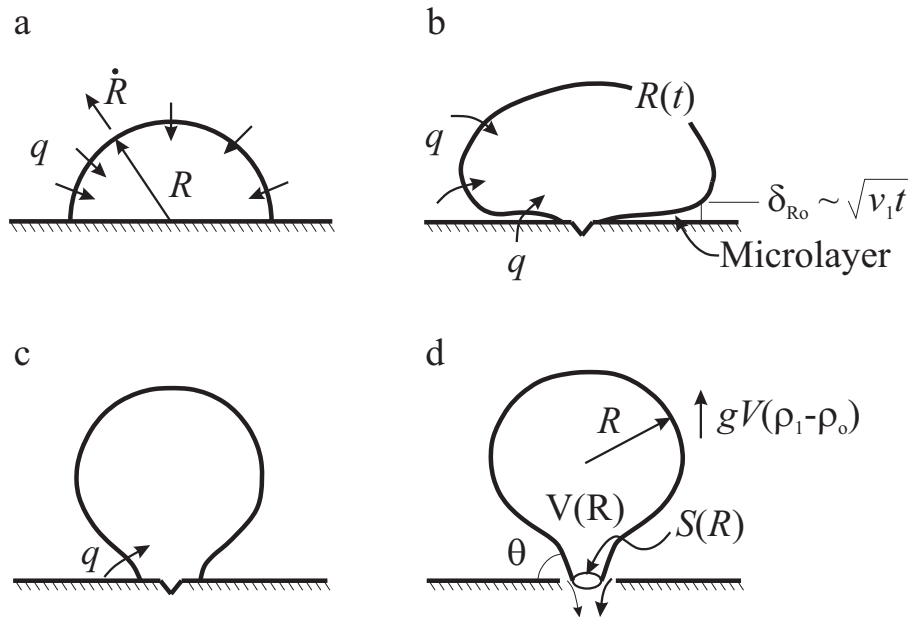


Figure 2.2: Bubble growth and detachment [7].

During this period, the microlayer of liquid acts as a conductive layer between the superheated solid surface and the bubble, as well as a reservoir to supply vapour to the bubble. During the growing period of the bubble, its boundary layer contacts with cooler liquid that is further away from the superheat surface. The growth rate of the bubble decreases and the effect of the hydrostatic and hydrodynamic force become stronger due to the increasing volume of the bubble. Fritz [8] was the first to correlate the bubble departure diameter by balancing surface tension force and buoyancy in related with contact angle (Figure 2.3).

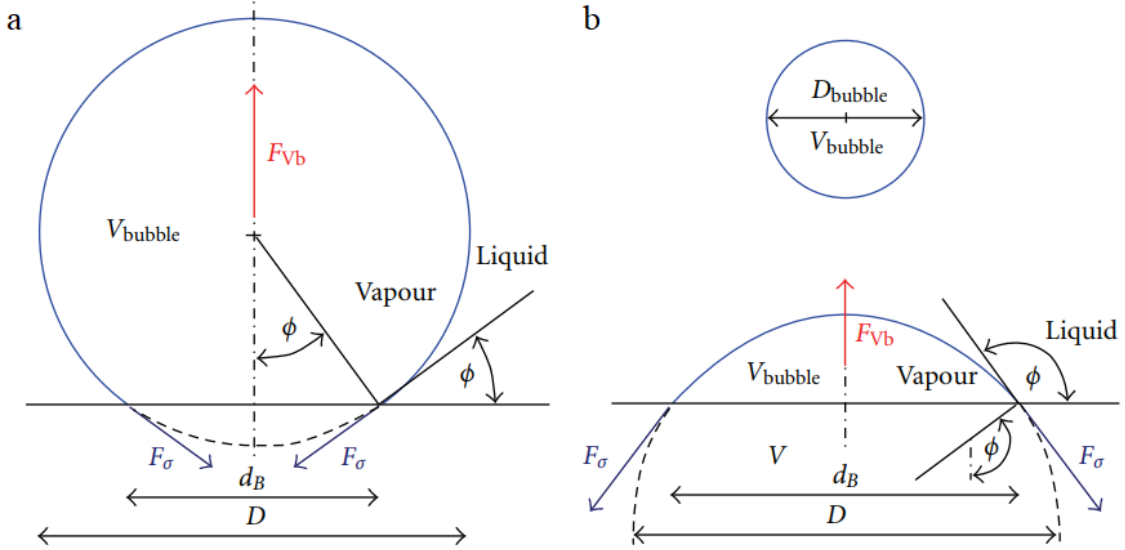


Figure 2.3: The balancing between buoyancy force and surface tension force on a vapour bubble. (a) On a hydrophilic surface and (b) On a hydrophobic surface [8].

$$gV(\rho_l - \rho_g) = p\sigma \sin\theta. \quad (2.2)$$

where $V = (4/3)\pi R^3 f_1(\theta)$ is the volume of vapour bubble and $p = 2\pi R f_2(\theta)$ is the perimeter of vapour bubble base. In these equations, the modified geometry functions $f_1(\theta)$ and $f_2(\theta)$ are used to account for the difference between full spherical shape and the real shape of the bubble, which is entrapped.

Thus:

$$D = 2R \simeq 0.0208\theta \sqrt{\frac{\sigma}{g(\rho_1 - \rho_2)}}. \quad (2.3)$$

Several mechanisms of heat transfer during the departure of the bubble from the solid surface can be summarised in Figure 2.4

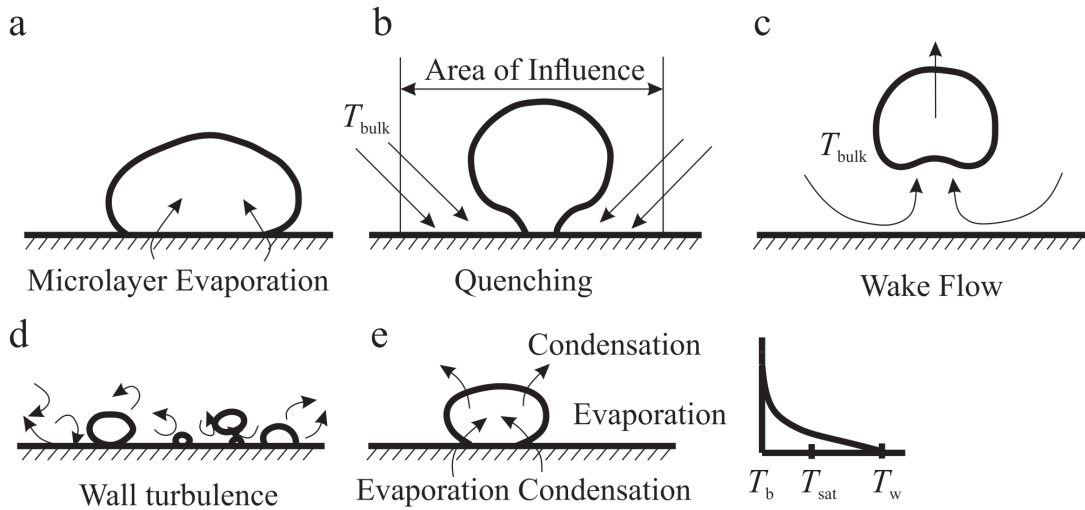


Figure 2.4: Mechanisms of heat transfer in nucleate boiling. (a) Conduction between the superheat solid surface and the vapour bubble across the microlayer of liquid; (b) Transient conduction between the replaced cool liquid bulk around the bubble on the surface when the bubbles round off and detach; (c) Localised convective cooling by the cool liquid around when the bubble detach; (d) Turbulence of the liquid close to the surface; (e) Evaporation at the base and condensation between the vapour bubble and the upper cooler liquid. The plot shows the distribution of temperature along vertical direction of the bubble from heated base [7].

2.2 Classical boiling heat transfer models

Several models were proposed regarding the transfer of energy to vapour bubbles during the nucleate boiling process. The different mechanisms of isolated bubble heat transfer have led to emergence of several mutually exclusive models [9–15]. Among these models, enhanced convection, transient conduction, contact line heat transfer, and microlayer evaporation have been the most prominent mechanisms

[16]. Most of the classical models on bubble nucleation considered bubble agitation and micro-convection the primary heat transfer mechanisms.

Transient conduction model.

Mikic and Rohsenow [17] proposed a bubble heat transfer model based on the work of Han and Griffith [18]. The model relied on the assumption that a departing bubble pulled along the superheated liquid volume immediate to the bubble with an area double the diameter of the departing bubble. This model is illustrated in Figure 2.5.

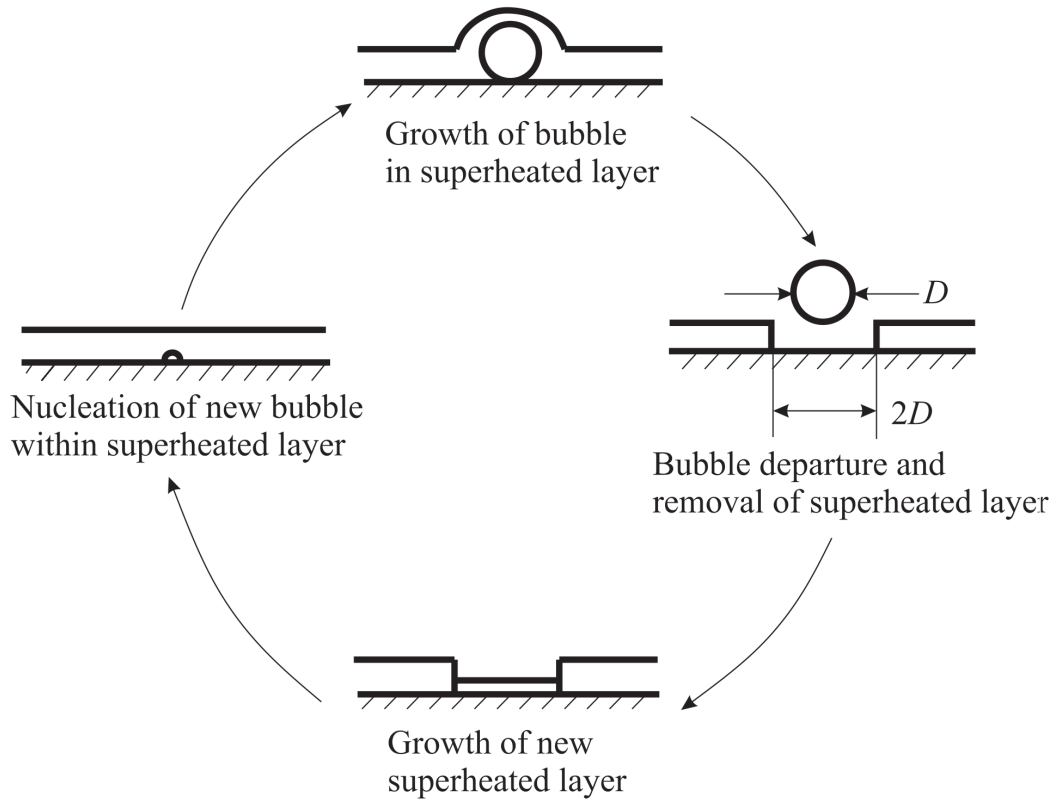


Figure 2.5: Bubble heat transfer mechanism suggested by Mikic and Rohsenow [16].

In the transient conduction model, the heat transfer from the surface during the bubble growth was not considered. Transient conduction into the bulk liquid after bubble departure was considered as the major mode of heat transfer.

Contact line heat transfer model.

Stephan and Hammer [19] developed a contact line heat transfer model based on the assumption that the principal heat transfer was evaporation of a thin liquid meniscus at the three-phase contact line. The meniscus near the contact line can be stretched to very thin, high heat transfer region in which liquid molecules cannot evaporate due to molecular adhesion forces. The evaporation rate therefore is affected by two competing effects. On the one hand, the evaporation rate increases with increasing film thickness due to reduction in of the adhesion force. On the other hand, decreasing the film thickness leads to a larger temperature gradient and hence larger conduction heat transfer through the film. Thus, the most favourable conditions for high rate of heat transfer happen at moderate film thickness, which occurs when the adhesion forces are small enough while still maintaining high rate of heat conduction across the film. As the film becomes thicker, the conduction resistance dominates leading to lower rates of heat transfer. In this model Stephan and Hammer assumed that heat could be transferred through the micro-region and the macro-region of a growing bubble. Here the micro-region refers to the vicinity of the three-phase contact line and the macro-region describes the liquid adjacent to the micro-region and the surface.

Microlayer heat transfer model.

Snyder and Edwards [20] proposed that it was possible for growing bubbles to trap a thin liquid layer at the surface that would eventually evaporate and transfer a significant amount of energy. Moore and Mesler [21] reported the temperature fluctuations on the surface under the bubbles and Hendricks and Sharp [22] showed fast reduction in surface temperature associated with bubble growth. The microlayer heat transfer model predicted a significant heat transfer below the bubble during its growth due to the evaporation of microlayer and a slight heat transfer outside of the bubble footprint. This model assumed that the heat transfer at the time of bubble departure was only due to the evaporation of the residual microlayer.

2.3 Numerical studies

Due to the large number of involving physical parameters, numerical simulation provides a valuable tool to study nucleate boiling heat transfer. Son and Dhir [23] conducted a numerical study of nucleate boiling on a horizontal surface at high heat fluxes by solving the equations governing conservation of mass, momentum and energy in the liquid and vapour phases. The simulation was based on the level set method in order to investigate the effects of surface superheat, nucleation site density, and waiting period on bubble dynamics. Sanna *et al.* [24] performed a numerical investigation of nucleate boiling heat transfer on thin substrates. The authors also discussed the capability of the proposed numerical model to reproduce experimental results for various conditions and analysed the obtained results for a large number of nucleation sites.

Genske and Stephan [25] studied heat transfer during growth of single vapour bubbles through numerical simulation. In this paper the authors divided the area around a single growing bubble into: a small, ring-shaped zone between heating surface and bubble called micro-region, the bubble itself, and its surrounding liquid referred to as the macro-region. Zhuan and Wang [26] reported the results obtained from numerical simulations of nucleate boiling in micro-channel. They analysed the Marangoni heat transfer through the bubble surface and compared with the incipient heat flux at the onset of nucleate boiling in micro-channels using VOF multiphase flow model. Narumanchi *et al.* [27] conducted numerical simulations of nucleate boiling in impinging jets, which occur in electronics cooling applications. They have used Eulerian multiphase model and validated the numerical results for boiling water and R113 jets, against existing experimental data in the literature.

2.4 Experimental studies

In order to gain better insight into the physical mechanism of the boiling process, it is necessary to obtain quantitative data of the relation between the bubble dynamics and the surface conditions such as temperature and heat transfer rate. Numerous experiments [28–63] were conducted to gain more insight and verify the models.

2.4.1 Investigation of surface temperature during bubble nucleation using micro-heaters and micro-sensors

There are several reports where researchers have designed microheaters [64–73] and microsensors [74–81] with different shapes for boiling experiments. Yaddanapuddi and Kim used microheater arrays, which consisted of small heaters and sensors, to obtain detailed measurement of the surface temperature and its spatial distribution under an individual bubble. While an individual bubble was induced at a micro heater, the other micro heaters were kept at constant temperature by a feed-back circuit. The required power for each micro heater to maintain its temperature was measured. The measured power indicated the heat transfer across each heater as shown in Figure 2.6 [82].

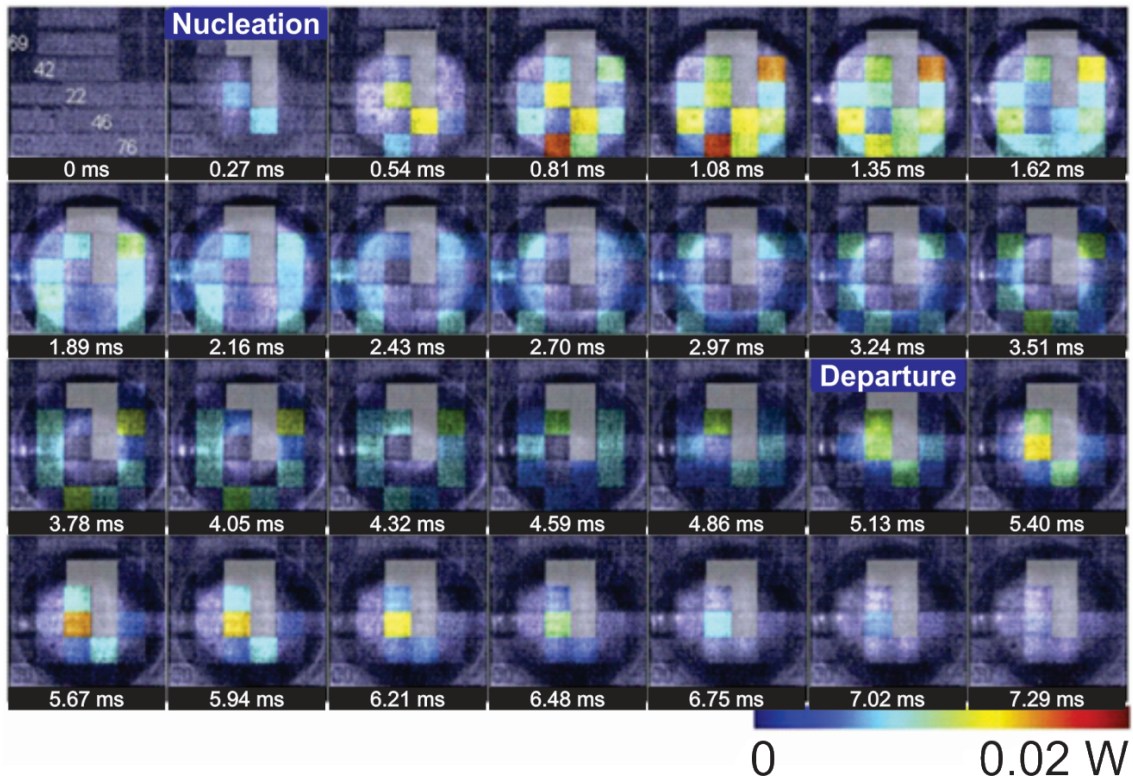


Figure 2.6: Single FC72 bubbles growing on a surface [82].

Demiray and Kim conducted a similar experiment with a smaller array of micro heaters [83]; each micro heater was of $0.1 \times 0.1 \text{ mm}^2$ in dimensions. Their results showed that conduction and micro-convection during bubble growth and after bub-

ble departure were the major mechanisms through which energy was supplied to the bubble. Additional heat transfer measurements and comparison with a simple model under sliding and oscillating bubbles also indicated that transient conduction during the rewetting process was dominant. A schematic of boiling substrate with 16 temperature micro sensors designed by Hutter *et al.* [4] is shown in Figure 2.7. The substrate was made of silicon, with a micro-fabricated heater on the back and 16 temperature micro-sensors, with an artificial cavity etched in the geometrical centre of each sensor layout, distributed in two rows on the front side. They have used this substrate to study the interactions between bubbles during nucleate boiling.

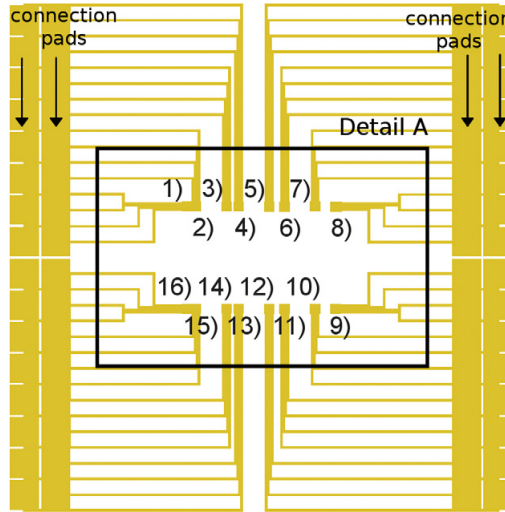


Figure 2.7: Location of the 16 sensors of the silicon substrate [4].

Moghaddam and Kiger [38] performed direct measurements of the heat transfer rate under isolated bubbles nucleated from an artificial site by using two layers of temperature sensors. They measured the temperature change at a distance very close to the nucleate site (20-40 μm). They divided the inducing of the bubble into two cases: with and without waiting time base on various temperature of the heater. They indicated that microlayer heat transfer accounted for between 16.3% and 28.8% of the total heat transfer, and the combination of transient conduction and micro-convection was the remainder for the cases without waiting time between bubbles. They also confirmed that the transient conduction and micro-convection were the most dominant mechanisms in terms of heat transfer rate. Moreover, the micro-convection became more important when the surface temperature increased.

2.4.2 Studies on nucleation site interaction and bubble coalescence.

Chai *et al.* [84] conducted boiling experiments on surfaces of different materials and different thicknesses to explore interactions of bubbles generated from different nucleation sites. Zhang and Shoji [85] investigated the average bubble departure frequency of two artificial cavities on a thin silicon surface for different dimensionless cavity spacing and found out three significant effect factors of nucleation site interactions: hydrodynamic interaction between bubbles, thermal interaction between nucleation sites, and horizontal and declining bubble coalescences. Coulibaly *et al.* [86] studied bubble coalescence during subcooled nucleate pool boiling using constant surface temperature as boundary conditions. They reported that coalesced bubble size and departure frequency decreased with the increase of subcooling. Bubble coalescence was classified by Buyevich and Webbon [87] into three different categories, as shown in Figure 2.8.

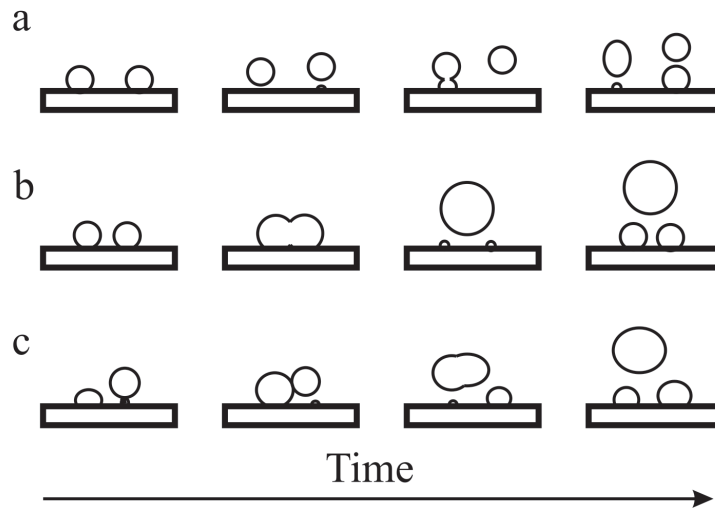


Figure 2.8: Types of direct bubble – bubble interaction (a) vertical coalescence; (b) horizontal coalescence and (c) declining coalescence [4].

Bonjour *et al.* [49] reported that the coalescence of bubbles from three artificial sites showed higher heat transfer coefficients than single site. Chen and Chung [88] conducted experiment on bubbles coalescence during nucleate boiling with micro-heaters and found an increase in bubble departure frequency and an enhancement

in surface heat transfer rate with the bubble coalescence. Hutter *et al.* analysed interactions between bubbles nucleated from artificial cavities during nucleate pool boiling on a silicon substrate with integrated microsensors [4]. Bi *et al.* [89] experimentally studied the effects of the nucleation site spacing on the bubble coalescence characteristics with a microheater array with five nucleation sites. The nucleation site was about $300 \times 300 \mu\text{m}$ and the dimensionless spacing were 0.49, 0.80, 0.98 and 0.94.

2.4.3 Verifying microlayer thickness using laser interference

Utaka *et al.* [90] conducted a study of the structure of microlayers in nucleate boiling of water and ethanol at atmospheric pressure. Sharp [91] measured the microlayer thickness by interferometric method and reported that it is $4.2 \mu\text{m}$ for water. With the same method, Jawurek [92] found the microlayer thickness for ethanol on a glass surface to be $0.5 \mu\text{m}$. However, experimental studies by Wagner and Stephan [93] indicated that microlayer evaporation only had an insignificant role in bubble heat transfer.

Voutsinos and Judd [95] used a laser light source to measure the thickness of microlayer in dichloromethane and reported a range from 1 to $6 \mu\text{m}$. Utaka and Nakamura [90] employed a laser extinction method by using a specially designed device comprised of a thin optical fibre in a thin tube of stainless steel. This method allowed direct thicknesses measurement of microlayers under a vapour bubble and a simultaneous high-speed recording of bubble dynamics. They observed a linearly increase of microlayer thickness with distance from the bubble site. The results obtained by Yabuki and Nakabeppu [96] also support those obtained by Utaka and Nakamura [90]. As this method failed to determine the initial microlayer thickness effectively, Utaka *et al.* [90, 94] developed a method to measure the microlayer thickness during early stages of bubble formation. A schematic of the laser measurement system used by Utaka *et al.* [94] is shown in Figure 2.9.

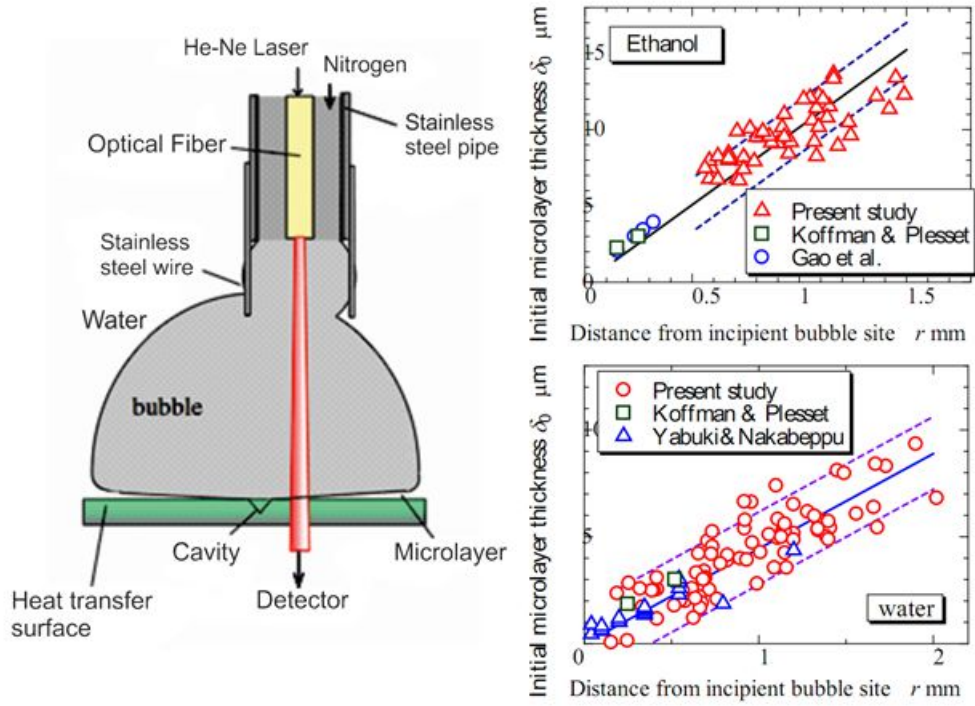


Figure 2.9: The process of measuring of microlayer thickness and value of microlayer measured for ethanol and water [94].

2.4.4 Studies on the effect of surface modifications to pool boiling

Surface modification of the superheated surface is one of the most effective ways to improve the heat transfer coefficient in nucleate boiling. Several studies [97–108] in this area are useful for validating nucleate boiling models (Table 2.1).

Table 2.1: Summary of pool boiling on modified surface.

Reference	Configuration	Experimental condition	Liquid	Major conclusion
Ng <i>et al.</i> [109]	Copper-foam metal	Subatmospheric pressure	water	Improved CHF and heat transfer

Continued on next page

Table 2.1 – continued from previous page

Reference	Configuration	Experimental condition	Liquid	Major conclusion
Vazquez and Kumar [110]	Nichrome ribbon heater surface	Heat flux up to 1000 kW/m ² , 1 atm	water	Improved CHF and heat transfer
Ahn <i>et al.</i> [97]	Oxidized zirc alloy surfaces	Heat flux up to 2000 kW/m ²	water	Improved CHF
Benjamin <i>et al.</i> [98]	Stainless steel and Aluminium with different polished surface.	Power supply: 3 kW	n-Hexane	Improved CHF and heat transfer
Chen <i>et al.</i> [99]	Silicon nanowires (20–300 nm in diameter, 40–50 μm long) and copper nanowires (200 nm in diameter and 40–50 μm long) over plain Si and SiO ₂ substrates	Heat flux up to 300W/cm ² , 1 atm	DI water	Larger than 100% improvement of CHF
Hendricks <i>et al.</i> [101]	ZnO deposition on Cu and Al substrates with average surface roughness ranging from 79.6 to 5863.2 nm	Heat flux up to 1000 kW/m ² , 1 atm	water	Heat transfer enhanced, improved CHF up to 2.56 times
Kim <i>et al.</i> [104]	Silicon plate with an array of ZnO nanorods of height ranging from several hundred nanometres to over 1 μm	Heat flux up to about 2350 kW/m ²	water	Improved HT, about 2.2 times improvement in CHF

Continued on next page

Table 2.1 – continued from previous page

Reference	Configuration	Experimental condition	Liquid	Major conclusion
Li <i>et al.</i> [105]	Copper nanorods of 40–50 nm in diameter and pitch 50 nm, nanorod height 450 nm on Cu substrate	Heat flux up to 170 W/cm ²	water	Improve heat transfer and CHF
Ho <i>et al.</i> [111]	Plain Al-6061 surface and AlSi10Mg intrinsic micro-cavity and micro-fin surfaces fabricated by SLM	Heat flux up to 47.9 W/cm ² and 70% enhancements in heat transfer coefficient	FC-72	Improve heat transfer and CHF
Ho <i>et al.</i> [112]	Carbon nanotube (CNT) coated surfaces with different orientations	Heat flux up to 20.1 W/cm ² and heat transfer coefficient 0.45 W/cm ² K	FC-72	Improve heat transfer and CHF in compare with bare surface, the enhancement in CHF reduces with surface angle
Pranoto <i>et al.</i> [113]	Graphite foam with different structures (block and fins) and thermophysical properties	Heat flux up to 120 W/cm ²	FC-72 and HFE-7000	Improve heat transfer coefficient for block structures
Jin <i>et al.</i> [114]	Highly conductive graphite foam	Heat flux up to 112 W/cm ²	FC-72 and HFE-7000	Improve CHF and reduce thermal resistant

This surface modification approach usually includes either treatments to enhance surface wettability, or surface morphological alternation with porous coatings, artificial fins and nano/microstructures:

2.4.4.1 Surface wettability.

Matevz *et al.* [115] used a hydrophobic/superhydrophilic PDMS-Silica patterned surface (Figure 2.10) made by a laser in their boiling experiment. In this study, they investigated the effect of wettability transition from hydrophobic to superhydrophilic on saturated boiling. By using high-speed IR camera, they confirmed that the increased wettability reduced the bubble contact diameter, allowed a higher density of active nucleation sites, and delayed the dry-out. Therefore, the superhydrophilic surface exhibited a larger critical heat flux enhancement than the biphilic surface with differently sized hydrophobic spots. However, surfaces with larger hydrophobic spot promoted boiling incipience and showed higher heat transfer coefficients at low heat fluxes.

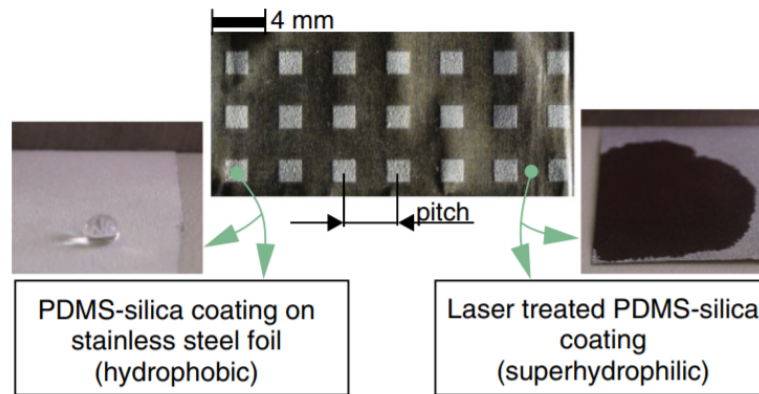


Figure 2.10: Sample of a laser-made biphilic pattern on a stainless-steel foil [115].

Takata *et al.* [108] applied a well-known phenomenon in which TiO_2 surface changes its wettability under UV light to their boiling experiment. The contact angle for water on TiO_2 surface reduce dramatically to nearly zero when being exposed with UV light. This exhibited a CHF enhancement up to two times larger the normal surface. They also found that the Leidenfrost temperature increases as

the contact angle decreases.

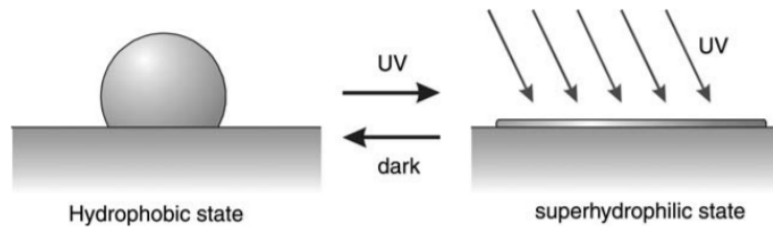


Figure 2.11: Photo-induced superhydrophilicity [115].

2.4.4.2 Surface morphological alternation with porous coatings.

Mori and Okuyama [116] investigated the enhancement of the critical heat flux in saturated pool boiling using honeycomb porous media. The schematic of their experiments setup is shown in Figure 2.12. They reported an increase in CHF with the decrease of height of the honeycomb porous plate on the heated surface. The reported CHF value was about 2.5 times that of a plain surface (1.0 MW/m^2). They concluded that the porous plate must have micro-pores with strong capillary suction and vapour escape channels in order to enhance the CHF. Also, the arrangement of honeycomb porous plates on the heated surface may remove the high heat flux over the large heated surface area.

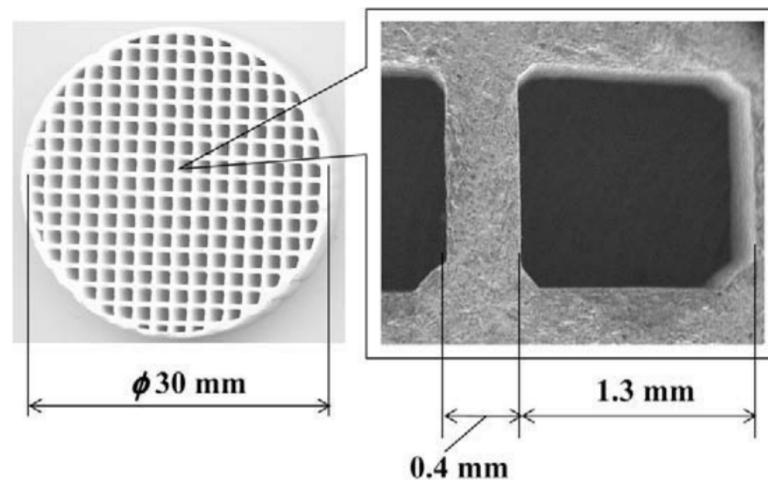


Figure 2.12: Shape of the honeycomb porous plate [116].

Wong and Leong investigated the enhancement of saturated pool boiling heat transfer using an innovative porous lattice structures produced by Selective Laser Melting [117]. The structure used in the experiment was a repeating geometry of octet-truss unit cell as in Figure 2.13.

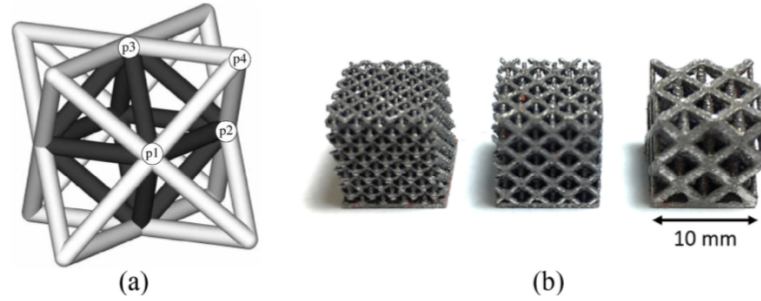


Figure 2.13: (a) Unit cell representation of the structure. (b) Fabricated structures with different size of unit cell [117].

All structured substrates showed a significant enhancement in critical heat flux (CHF) and a large delay in Leidenfrost temperature in compare with the bare surface, which means that the modified substrates are able to maintain high level of heat flux even at relative high surface temperature. The enhancement in heat transfer coefficient was measured up to $1.35 \text{ W/cm}^2\cdot\text{K}$, which is among the highest value reported for FC-72 on porous surfaces. Furthermore, they also observed two modes of boiling with different size of the structure: the stable mode, in which the liquid return pathway was separated with the vapour path and the unstable mode, in which there was a disruption in the liquid replenishment pathway (Figure 2.14).

For surface modification at smaller scales, Hendricks *et al.* [101] used nanostructures fabricated on aluminium and copper surfaces to improve the pool-boiling heat transfer. In this work, nanostructures made of ZnO were deposited on Al and Cu substrates (Figure 2.15). They observed a CHF of 82.5 W/cm^2 with water as fluid for ZnO on Al, in comparison with a CHF of 23.2 W/cm^2 for bare Al surface with a surface superheat reduction of $25\text{--}38 \text{ }^\circ\text{C}$. These critical heat flux values on ZnO surfaces correspond to a heat transfer coefficient of $\sim 23,000 \text{ W}\cdot\text{m}^{-2}\cdot\text{K}^{-1}$ [101].

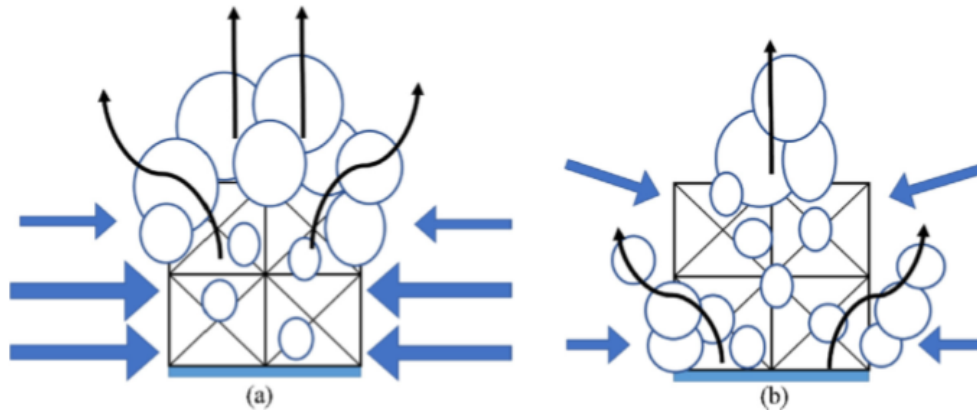


Figure 2.14: (a) Stable and (b) Unstable boiling pattern [117].

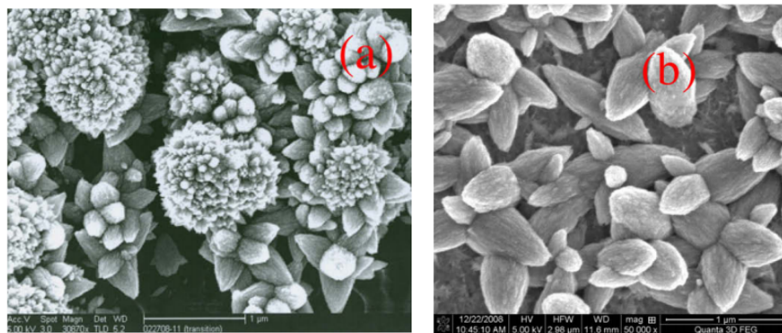


Figure 2.15: (a) ZnO on Al and (b) ZnO on Cu structures [101].

2.4.4.3 Artificial fins and nano/microstructures.

Zhong *et al.* [118] studied the effect of inclined surfaces with artificial cavities on saturated boiling. They found that the inclination angle has significant effect on critical heat flux and surface superheat. There is an optimum angle that maximize CHF and this enhancement is even amplified further by increasing the deep of cavities on the test surfaces. Compared with the plain surface the CHF increases on the downward-facing surfaces with cavities were not significant.

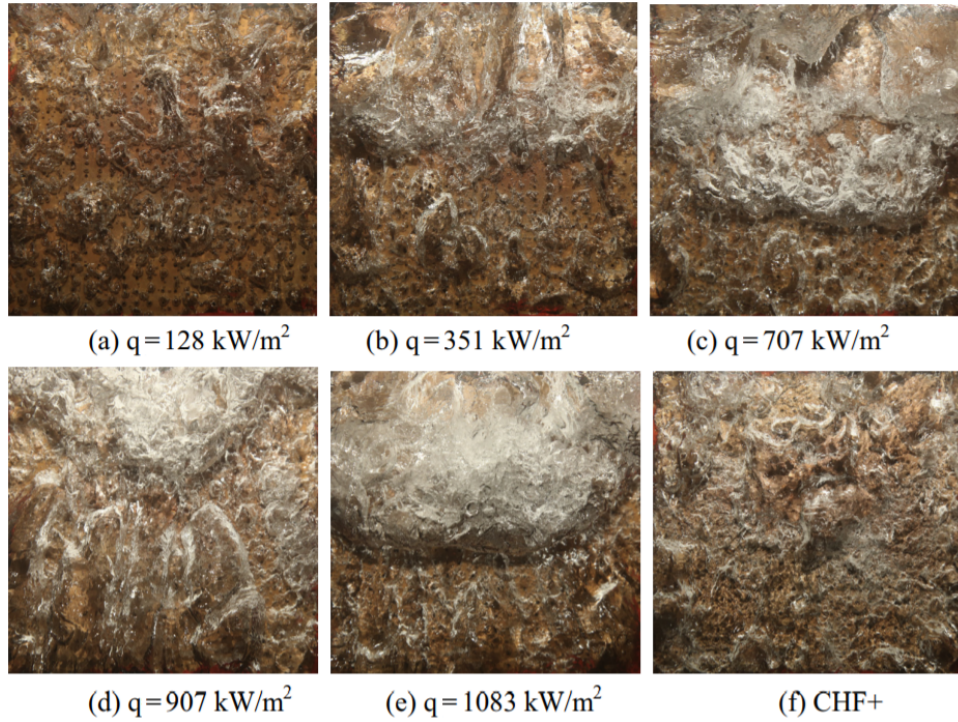


Figure 2.16: Copper test sections with cavities [118].

Li *et al.* [119] carried a series of boiling experiment on various substrates modified with multi scale structures. First, they used copper nanocavity surface to examine the role of contact angles in lateral Rayleigh-Taylor wavelength to vertical Kelvin-Helmholtz wavelength for the onset of CHF. On the second set, they investigated the effect of pillar pitch on hydrodynamic instability at CHF. Last, a multiscale copper structure is studied to examine the collective role of both millimetre, microscale and nanoscale structures on CHF and HTC of pool boiling. The experimental results show a better enhancement of combined nanostructures and porous pillar than that

of individual structures.

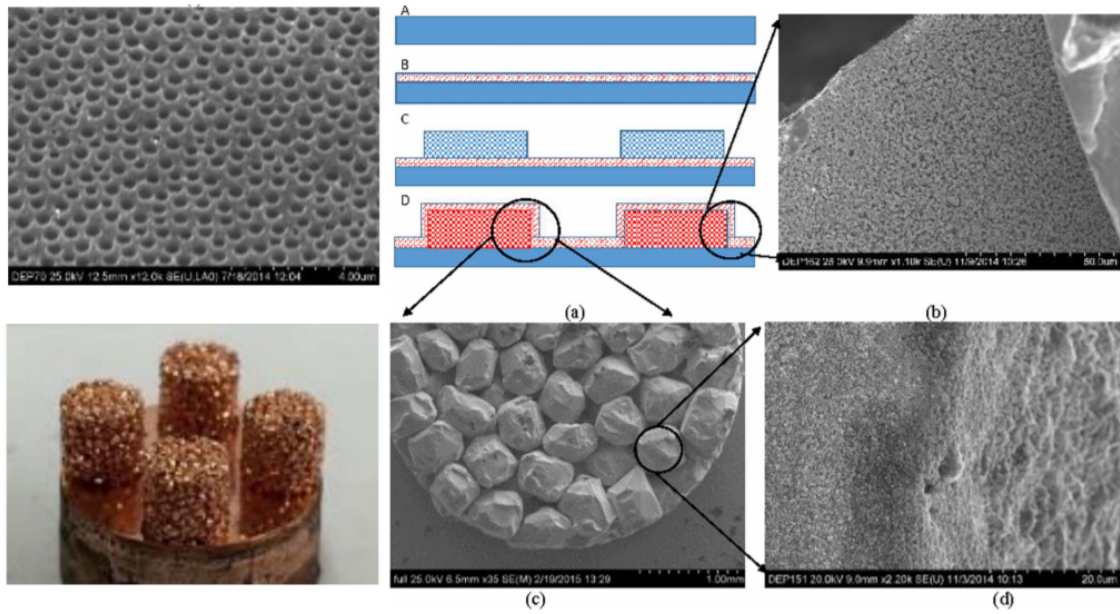


Figure 2.17: Test substrate with micro cavities, copper porous pillars and combination of copper porous pillars with nano-porous coating [119].

Rahman *et al.* [120] reported a new method to improve boiling heat transfer by integrating an array of non-conductive strips onto the substrate surface. The modified surface created a liquid and vapour pathway inside the liquid body, in which the liquid and vapour will have their own separating movement path and therefore increase the heat transfer efficiency. By replacing 18% of the surface with a non-conductive epoxy, they achieved five times more heat transfer rate at the same superheat temperature.

Dhillon *et al.* [121] and Rahman *et al.* [122] have conducted a systematic experiment on the effect of rewetting and wickability on pool boiling. They also proposed their own model to explain the phenomenon observed. The common conclusion is that the rewetting and wickability had a significant role on the extra heat transfer through the hot surface. This extra heat is due to extra liquid which is wicked to the surface by micro/nano-combined structures.

Generally, most of the reported studies on surface modification utilised small-scale layers of structures deposited on to the heated surface. This method, while improves heat transient conduction, prevents micro-convection, which is one of the

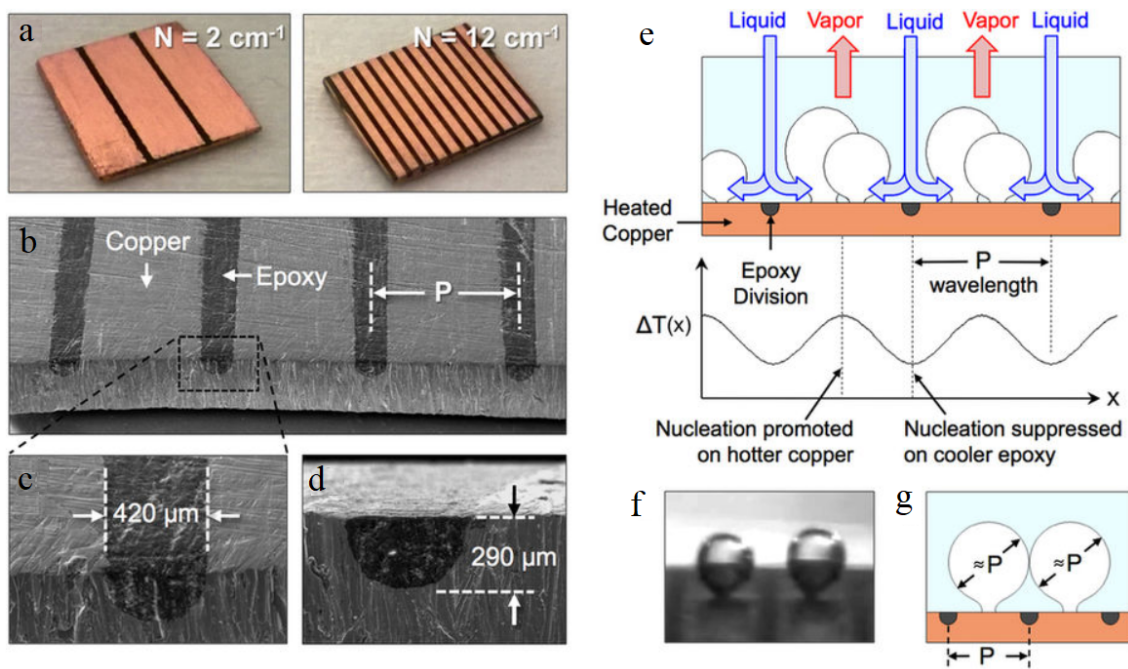


Figure 2.18: Bi-conductive surfaces to tailor spatial variations in surface temperature [120].

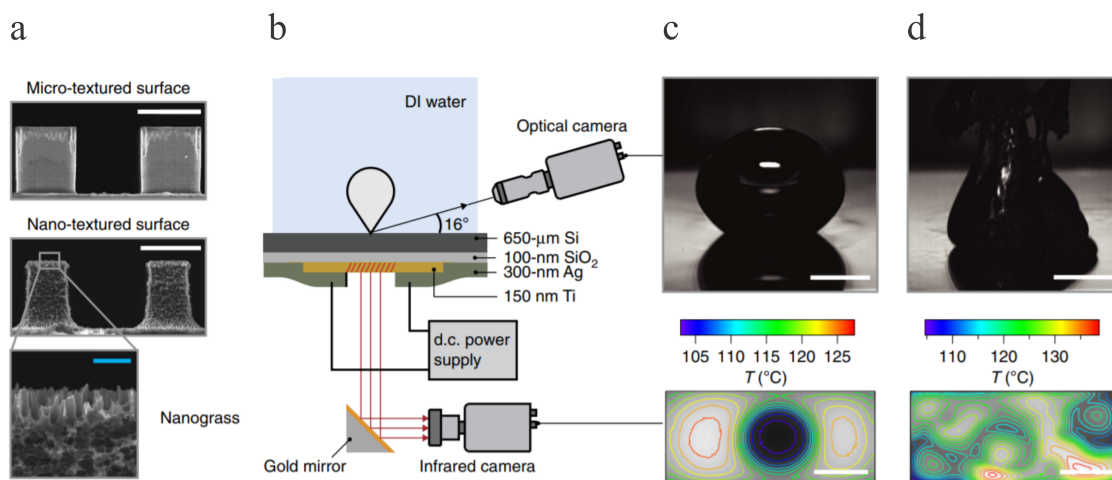


Figure 2.19: Structured surface and methodology of boiling experiments in Dhillon study [121].

most dominant mechanisms of nucleated boiling.

Most of the modelling approaches of nucleate boiling give a lower result of heat transfer coefficient than in reality. The possible reasons are the sensitivity of nucleate boiling to the micro-geometry of the surface and its wettability. In other words, small changes in these two factors may result in significant change in locations, as well as numbers of nucleation sites. Thus, a detailed experimental study of how a bubble is induced and detached from a nucleation site will allow better control of the boiling heat transfer process.

2.5 Classification of boiling condition and general heating methods

In this section, we would like to introduce the classification of boiling experiment that are usually considered in most of recent experiment as the first important boundary condition. Also, the general heating methods as well as the data correlation will be described as a preparation steps for our next experiment in the proceeding chapters.

2.5.1 Studies on boiling with different liquid temperature condition: saturated and subcooled boiling

According to the heating method, general pool boiling experiments can be divided into saturated pool boiling and subcooled pool boiling. In a typical saturated pool boiling experiment, illustrated in Figure 2.20a, the whole liquid is kept at a temperature equal or slightly higher than the boiling point. The vapour from the boiling process will be cooled by a condensing unit placed far from the pool. This condensing process can be controlled to keep the constant vapour pressure inside the pool. In saturated pool boiling, the bubble burst at a free surface. The detached bubble move upward to the free surface cannot condense back to the hot liquid; it collapses on this free surface.

In a typical subcooled pool boiling experiment, illustrated in Figure 2.20b, the temperature of the working liquid is lower than the boiling point. This condition can be achieved by cooling along the pool surface. Either the boiling vessel must

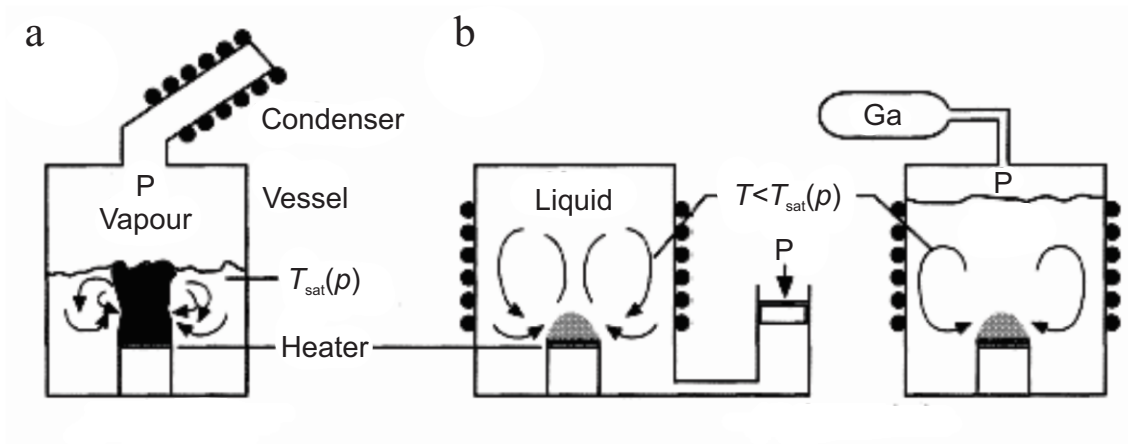


Figure 2.20: Pool boiling is classified as saturated and subcooled boiling (a) Saturated and (b) Subcooled pool boiling [123].

be connected to a separate vessel in which the pressure is controlled, or there must be a gas space above the pool. The vapour in this case cannot escape since it is condensed back to the liquid before reaching the top surface. The subcooled pool boiling is usually used for studying of individual bubble whereas the saturated pool boiling is applied to the experiments with high heat flux.

Coulibaly *et al.* [86] reported the effects of the subcooling on bubble shape, size, and departure time. It is worth mentioning that during subcooled boiling on biphilic and super hydrophobic surfaces, bubbles could be nucleated and grow even at nominally negative surface superheats [1, 124].

2.5.2 Typical heating method and data correlation using in recent experimental approach.

In boiling experiment, the heating scheme by means of electrical resistance is preferred because it allows accurate control of the input heat flux and relatively compact size of the boiling pool. The electrical resistance can be used in several ways [123] as follows:

- (i) The thin plate heater.

Here, a thin electrically conductive plate is used as a heater as shown in Figure 2.21a, through which a current applied for uniform heating. The input heat is calculated from the current and the voltage across the heater. It can

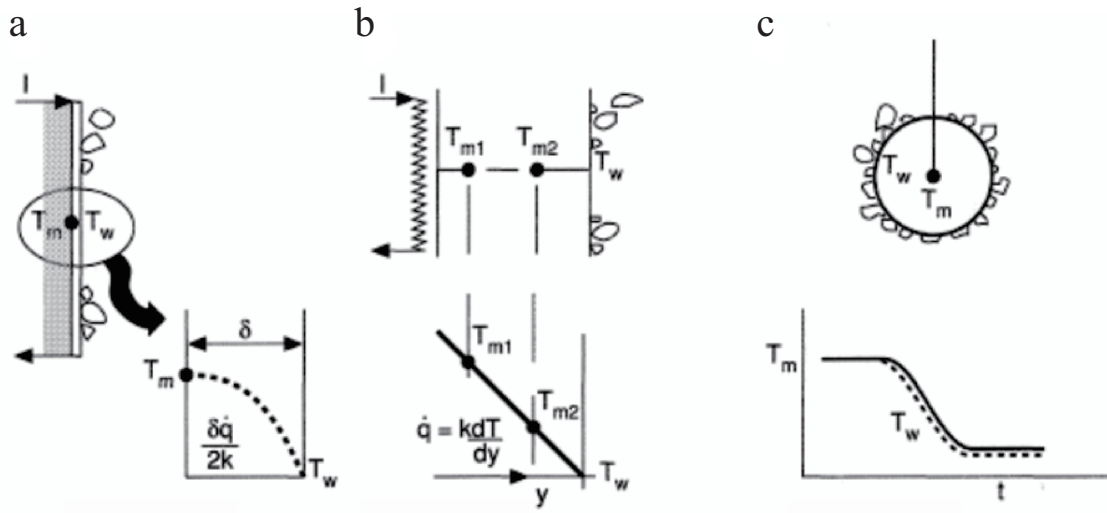


Figure 2.21: Heating method and measurement of heat flux and surface superheat. (a) Thin plate heater; (b) Thick base heater and (c) Heater as a calorimeter. [123].

be measured by attaching temperature sensor such as thermocouple, thermistor or thermochromics liquid crystal on the non-boiling surface of the heated surface. The temperature on the boiling surface will then be derived by using heat transfer equation. Instead of the thin plate, a very thin layer of electrically conducting material such as gold can be deposited on an insulating substrate such as glass. If this layer is so thin and transparent, the boiling process can be observed from the bottom of the glass slide. The disadvantage of using the deposit layer as a heater is difficulty in bonding with the base and typical low thermal conductivity of the base (except for sapphire).

(ii) The thick base heater.

This kind of heater consists of a thick block made of high thermal conductivity material such as copper or aluminium. One side of this block is heated by an electrically insulated resistor and the other side is in contact with the liquid. Thermocouples are attached along the heat transfer direction of the block to measure the temperature gradient and then heat flux will be calculated. The temperature of the boiling surface can also be extrapolated, Figure 2.21b.

(iii) Heater as a calorimeter.

In certain experiments, which demands heater with specific shape, such as

sphere, the heater is pre-heated before embedded into liquid pool. The change in temperature is measured by a thermocouple integrated on the heater. The reading can be calculated back to retrieve the temperature at the boiling surface by the transient temperature gradients within the heater. This method is often used for the study of transition boiling, Figure 2.21c.

Each heating method has its advantage on calculating the heat flux and temperature on the boiling surface. Thin plate heater provides a convenient way to observe the boiling process from bottom-up direction and trivial way of calculation. However, it is difficult to fabricate, and the back base usually has a low thermal conductivity. The thick base heater is simple to set up, but the calculation is little complex since many factors such as the geometry of the block or thermocouple calibration are needed to be considered. The calorimeter is just used in some specific case that need the special shape of the heater.

While the heating method is important to the experimental set-up of the boiling, the micro-geometry and wettability of the boiling surface are two factors that have a strong effect to the nucleate and transition boiling. Thus, there are several studies [125, 109, 126–130, 110] of boiling heat transfer with different kinds of heating method considering effects of heater size and orientation.

Chapter 3

Design and fabrication of experimental setup and components

3.1 Design and fabrication of the boiling rig

Design of the boiling rig is based on the saturated pool boiling (Figure 2.20a) to ensure that it can be used for the case with high heat flux. The design is subjected to the following conditions. The boiling setup should allow precise measurement of the surface temperature gradient from which heat flux is calculated (Figure 2.21b). The design should ensure minimum heat loss to the side of insulated wall and provide a stable heat transfer across the heated surface. It also should provide a good control on the liquid inside the pool in terms of pressure control, stable temperature outside the pool, condensing unit and circular flow in/out the pool.

The heat flux calculation is based on the heating method in Figure 2.21b, in which a thick base is used as a heater and is made of material with high thermal conductivity such as copper or aluminium (Figure 3.1). The heat flux is calculated using the temperature gradient, which is resulted from the temperature measured by several thermocouples at three different points on the heat transfer direction. The method to calculate heat flux will be described in more detail in Chapter 4. In addition to optimising the design, one of the most important factors is the heat loss to the surrounding environment q_{loss} . It is estimated using Eqs. 3.1-3.3 (the

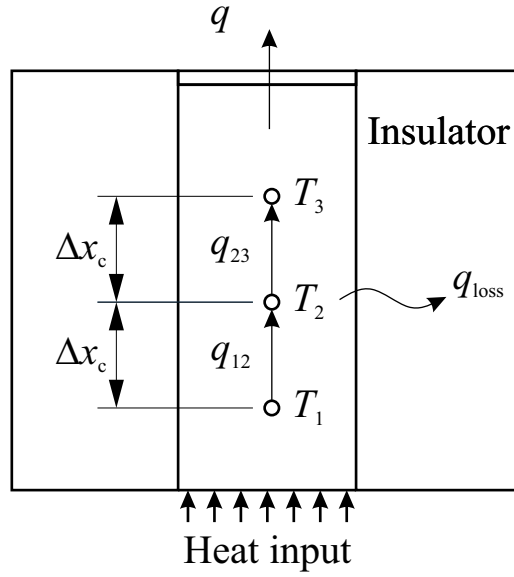


Figure 3.1: Scheme to estimate the heat loss to the surrounding environment.

uncertainty of heat flux measurement is described in Appendix H)

$$q_{12} = k \frac{T_1 - T_2}{\Delta x}. \quad (3.1)$$

$$q_{23} = k \frac{T_2 - T_3}{\Delta x}. \quad (3.2)$$

$$\%q_{loss} = \frac{q_{23} - q_{12}}{q_{12}} \times 100. \quad (3.3)$$

Based on these targets and notes, we will go through the boiling rig designs used in the next three experiments.

3.1.1 Boiling rig for pool boiling on passive nanostructured surface

In this design, a cylindrical 400 W cartridge heater was used as an original heat source. Heat is transferred from the cartridge heater to the silicon substrate through a long copper rod, which was thermally insulated with surrounding environment by a thick rod of Teflon. The test substrate was placed on top of the copper rod with its end exposed from the Teflon base. A very thin layer of silicon thermal glue (thermal

conductivity $k_g = 1.8 \text{ W}\cdot\text{m}^{-1}\cdot\text{K}^{-1}$) was applied between the test substrate and the copper surface to eliminate air gap and to improve heat transfer to the substrate. The temperature gradient along the main heat transfer direction was recorded by three thermocouples embedded along the centre line of the copper rod. There was also another thermocouple put inside the copper rod to control the power input to the cartridge heater through a PID controller.

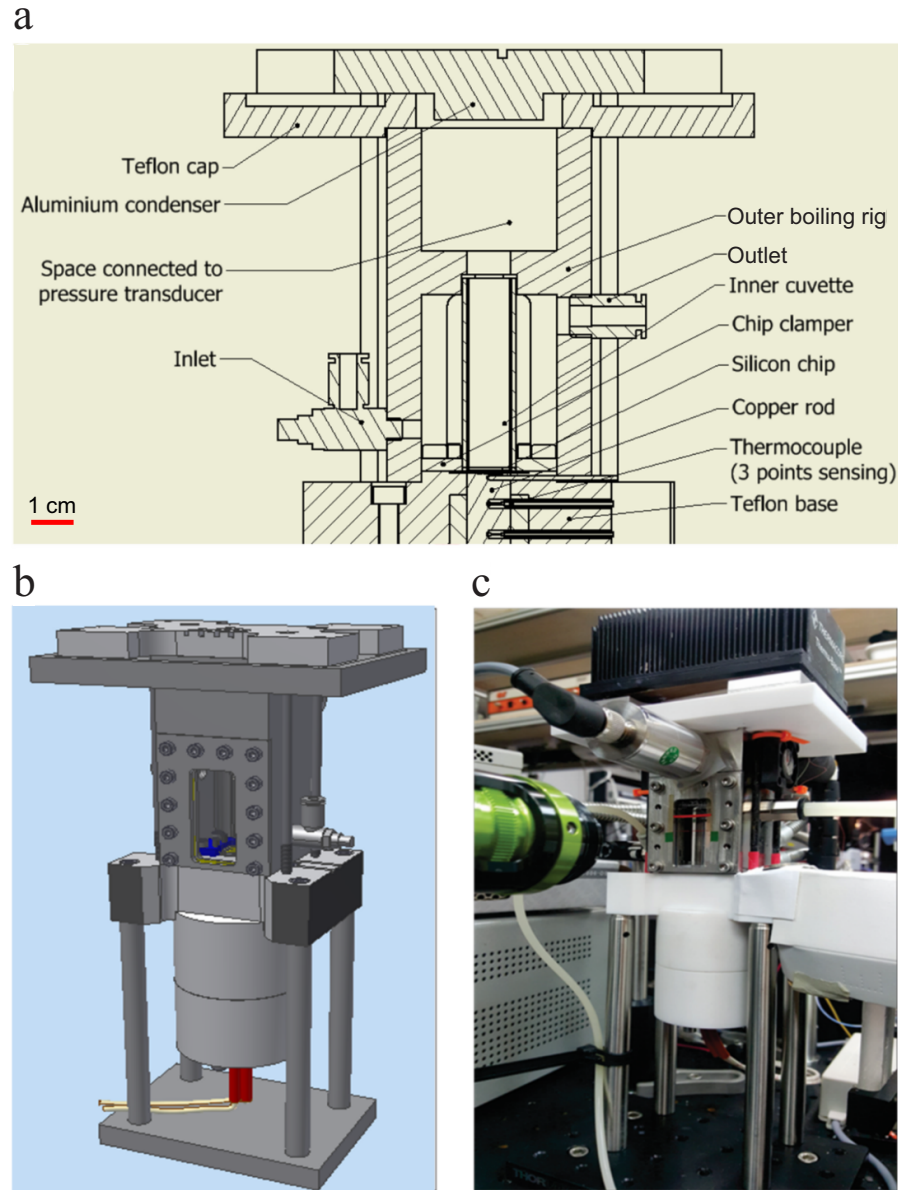


Figure 3.2: First design of the boiling rig for passive pool boiling experiment. (a) Schematic view of the boiling rig; (b) Three-dimensional model the boiling rig and (c) Real image of the rig.

The upper parts of the set up included the module for test liquid containing and a condensing module. Test liquid was kept within the space constrained by the substrate below and a rectangular glass cuvette at four sides. This glass cuvette has its two ends opened and was pressed against the substrate by a stainless steel rig (Figure 3.3). This rig part is designed to have an upper space that is connected to a pressure transducer and a lower space to be attached with the top end of the cuvette. The upper and lower space is connected to each other by a through hole so that the pressure inside the cuvette is the same to the pressure that the pressure transducer read. The pressure transducer is connected to the part by G1/4 screw to ensure the air-tight condition. In addition to keep the test liquid temperature stable, hot water was circulated between the cuvette and the stainless-steel rig through the inlet and outlet line attached on the outer rig. (Figure 3.2).

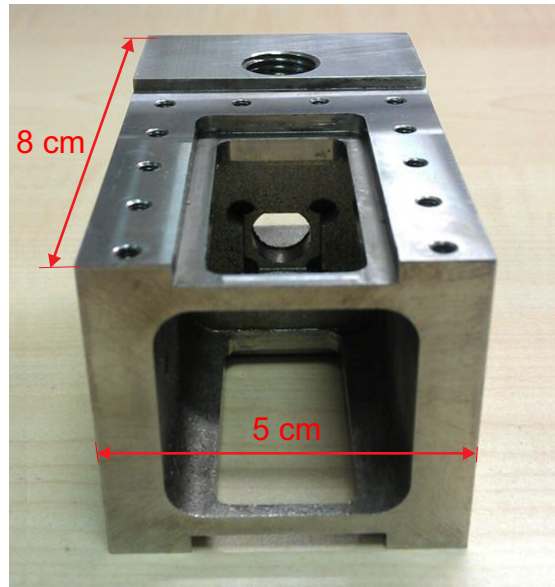


Figure 3.3: Wall-rig part was manufactured by stainless-steel.

The condensing module is put on top of the stainless-steel rig and it includes an aluminium cap, a peltier unit, a cooling fan and a cooling controller box. The peltier has a square shape with a thickness of several millimetres and two working sides. When it is provided with electric power, its bottom side will be cooled down and the top will be heated. We used the cool side to apply to the aluminium cap and the other hot side was attached to a high-speed cooling fan. This allows to

adjust the cooling power by regulating the power input to the peltier unit through a PID controller.

A validation of this setup has been carried out for pool boiling of FC-72 on smooth silicon surface and it shows good agreement with other theoretical models. The details on this validation result will be described in the next chapter.

3.1.2 Boiling rig design for boiling with actuated pillar and PIV

The previous design of boiling rig can be used for saturated boiling experiments on passive structure substrate. However, we also need to conduct boiling experiment with the presence of actuated pillar and laser light source, which is needed for flow field measurement using PIV. This design of the boiling rig was planned to meet these demands.

This rig was developed from the previous design with two electromagnets integrated inside the chamber as in Figure 3.4 Two electromagnets are placed next to the cuvette side walls to maximise the magnetic field surrounding the actuated pillar. There are also two permanent magnets on top of the cuvette to maintain a static vertical magnetic field. The detail in magnet arrangement will be discuss in next part.

As for the PIV measurement, the rig is added a Right-Angle Prism Mirror (MRA10-E02 Thorlab) on top to reflect the laser light sheet to the interested area close to the actuator. The space surrounding the cuvette is keep in partial vacuum condition by a vacuum pump. The cuvette is opened on its top side, made it possible for the vapour rise to the upper condenser, where the liquid is condensed by circulated cool water (circulated water flow through the aluminium condenser part) and return to the bulk liquid downward. A pressure transducer is integrated on the wall of the condenser to follow the vapour pressure inside. The substrate is heated by the copper rod placed below and its sides are insulated by a thick base of Teflon. Thermocouples are inserted to the centre of the copper rod to measure the temperature gradient along the heat transfer direction, which can be used to calculate heat flux and substrate surface temperature as discussing in Chapter 4.

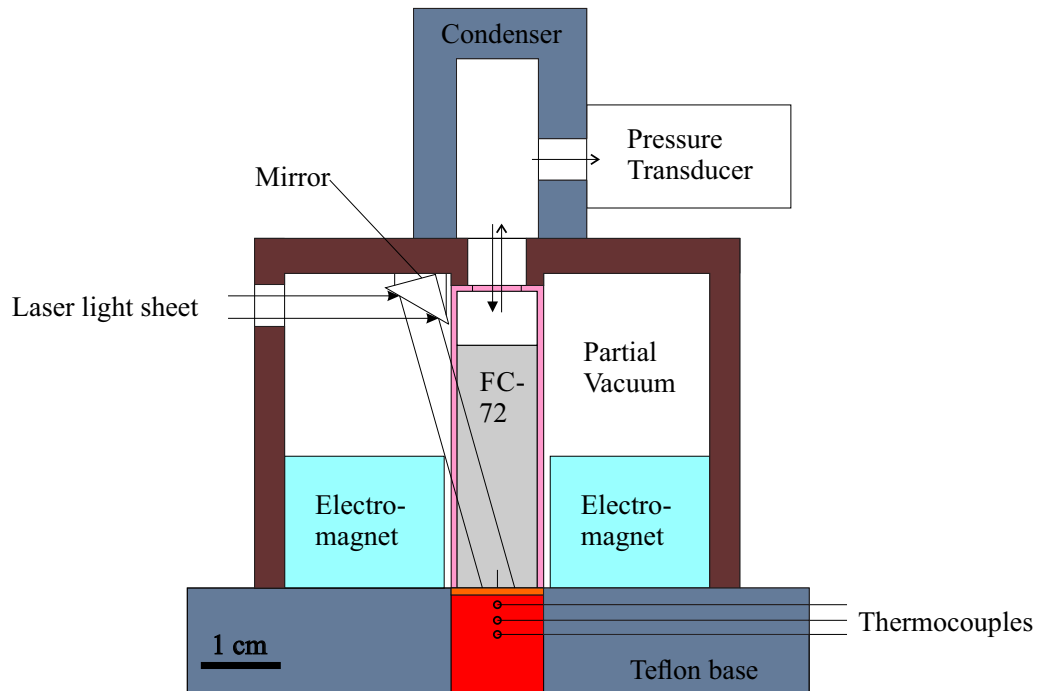


Figure 3.4: The second design of the boiling rig for boiling experiment with actuated pillar and PIV.

3.1.2.1 Design of reflex mirror

The laser beam cannot be shined from the top of the cuvette due to the condenser unit. Even if the light could come from the top side, the visual recording would not be clear due to the violent boiling below. The best direction for the light is shining directly from the side. However, the side of the cuvette is blocked by the electromagnet. The alternative solution is to shine the laser beam from the side which is not blocked and reflex it to the area of interest using a mirror. The reflex mirror (MRA10-E02 Thorlab) has been mounted inside the rig and tilted an angle of 30 degrees. This allows the area of interest (4×4 mm) around the pillar to be shined by laser light sheet as in Figure 3.5.

3.1.2.2 Design of magnetic field pattern

The magnetic field used to drive the actuated pillar depends on the magnetism properties of the pillar. The ferromagnetic metals such as Iron or Nickel is just attracted and align itself to the magnetic line. If a nickel wire is put into a magnetic field, it will align its length to the magnetic line in a direction so that its movement

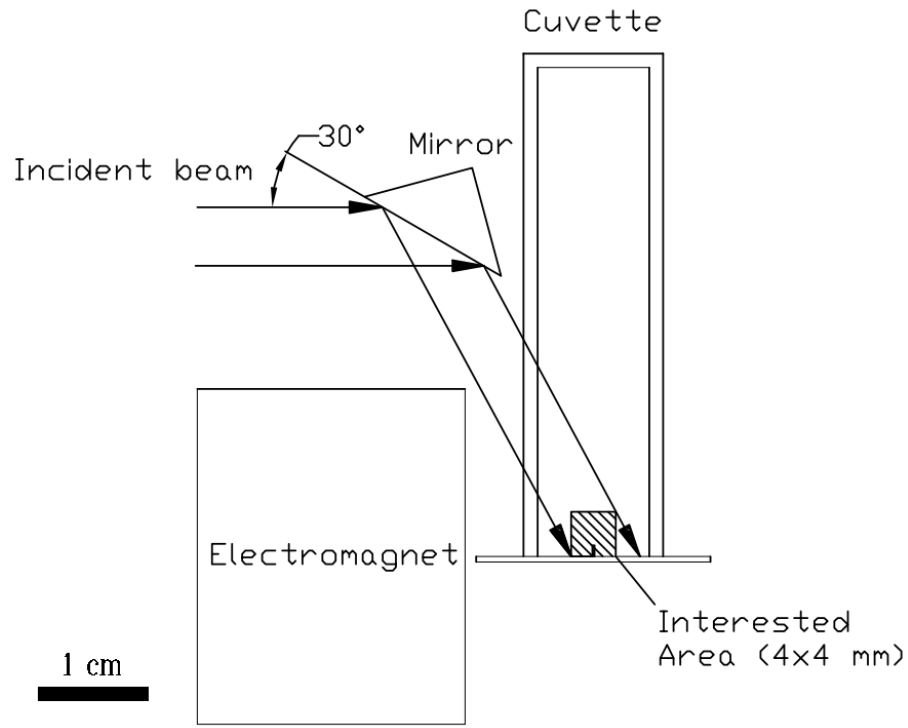


Figure 3.5: Incident beam and area of interest (4×4 mm).

is minimised, which means it does not depend on the direction of magnetic field. Therefore, a good way to drive a nickel pillar is to generate a magnetic field that can change its direction continuously. If the magnetic field direction is changed suddenly, the pillar will follow its natural trend: align to the closest magnetic line and the control on pillar's movement will be lost at this point. In chapter 4, we plan to use nickel wire and nickel strips as actuator material. Therefore, a pattern of driven magnets is considered in this design to generate a proper magnetic field for both cases.

The magnetic field line generated by a pair of electromagnets (Stephenson Gobin Type 58, 24VDC, 3.8W, 230N) is almost parallel in horizontal plane as shown in Figure 3.6a. The magnetic strength is around 20 mT measured at the centre of the substrate and slightly increase to 25 mT at the side close to the electromagnet. When the direction of magnetic field changes from left to right or vice versa, its angle to the horizontal direction changes suddenly from 0 degree to 180 degrees on the same magnetic line. Since the magnetic field direction is changing so fast on the same magnetic line, the nickel pillar just keeps its old position instead of moving to the other side. To solve this issue, we add a pair of N52 Grade Neodymium magnets

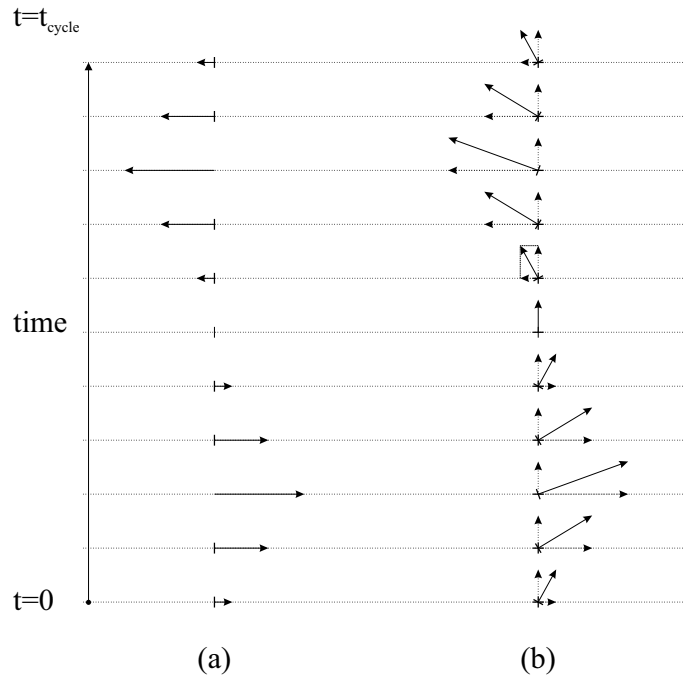


Figure 3.6: Magnetic field direction of two cases: (a) without permanent magnet and (b) with permanent magnet.

(0.5 T close to the magnet surface) to the set-up which can generate a static vertical magnetic field as in Figure 3.7. Magnetic field strength measured at the centre of the substrate is reduced to 35 mT due to long distance from the magnets. The total magnetic line is now the sum up of two vectors, one is the dynamic horizontal field by electromagnet and one is the static vertical field by permanent magnet. As shown in Figure 3.6b, the results vector has its direction changing continuously from side to side, which can drive the nickel wire in a more controllable way. The detail in the movement of nickel wire under this magnetic field is discussed in Chapter 4.

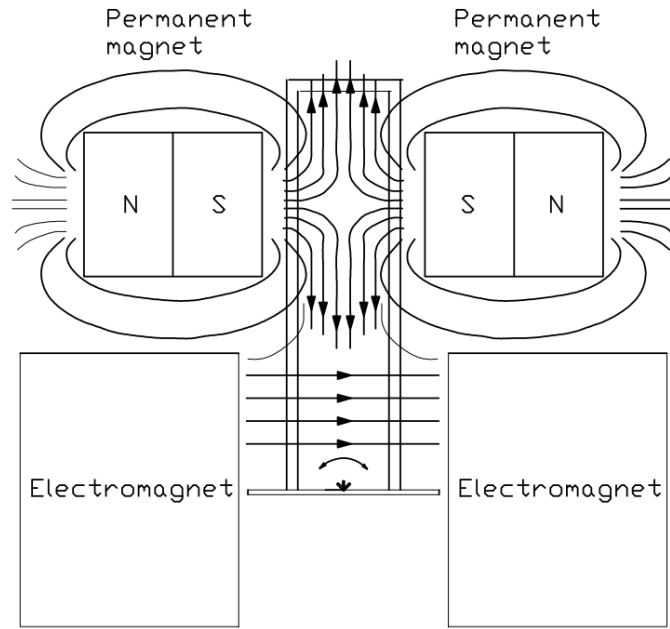


Figure 3.7: Arrangement of electromagnet (horizontal changing field) and permanent magnet (vertical static field).

3.2 Design and fabrication of the microheater and microsensor

3.2.1 Design of the microheater

The pattern of the microheater is designed as presented in Figure 3.8. A micro-cavity is located at the centre of the micro heater for bubble generation. The diameter of the cavity is $40 \mu\text{m}$ and $20 \mu\text{m}$ depth. The material of lead-out path is gold and the microheater layer is Platinum. On the top of this microheater, a layer of SiO_2 is deposited to ensure the heater is electrical insulation when operating. The leading layer is connected to outside at four corners of the silicon substrate.

The layer-by-layer structure of micro-heater is made by sputtering method as follows (detail of the sputtering method used is described in Appendix J). The surface of silicon substrate is considered the bottom layer. There is an intermediate layer of SiO_2 , without this the other layer will be easily detached from the silicon surface. A thin layer of platinum is deposited on SiO_2 to form the micro heater layer. A gold layer is also deposited on the SiO_2 layer and contacts with micro-heater layer

to form a leading layer. Finally, another layer of SiO_2 is deposited on the top to protect the microheater and act as an electrical insulator. The minimum resistance of the Pt layer is $\sim 400 \Omega$, which can reduce the power consumption and high heat concentration (on the area of 1 mm^2). The structure of the microheater (red layer) and the lead-out layer (yellow) are illustrated in Figure 3.8.

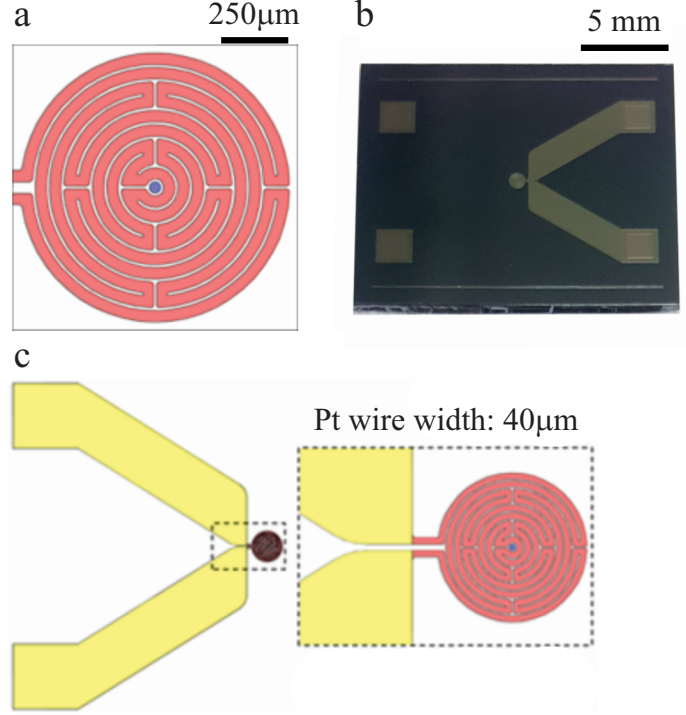


Figure 3.8: Structure of microheater - first design: (a) Design layer microheater (red layer) and microcavity, (b) Real image of the microheater and (c) Leading layer of the microheater.

The resistance is calculated as follows:

$$\frac{R_{Pt}}{R_{Au}} = \frac{\rho_{Pt}}{\rho_{Au}} \times \frac{L_{Pt}}{L_{Au}} \times \frac{W_{Au}}{W_{Pt}}. \quad (3.4)$$

$$\frac{R_{Pt}}{R_{Au}} \simeq \frac{10.6}{2.44} \times \frac{14.4}{8.4} \times \frac{600}{40} = 112. \quad (3.5)$$

where R_{Pt} , R_{Au} are the respective resistances of Pt and Au. L_{Pt} , L_{Au} are their corresponding lengths and W_{Pt} , W_{Au} are their corresponding widths whereas ρ_{Pt} ,

ρ_{Au} are their bulk electrical resistivities.

The technical specifications of the design of microheater are in Table 3.1.

Table 3.1: Technical specifications for microheater.

Specification	Value
Cavity diameter (μm)	40
Pt wire spacing (μm)	10
Width of Pt heater wire (μm)	40
Heater length (mm)	14.4
Heater area (%)	57.6
Heater resistance (Ω)	400
Pt thickness (μm)	170

3.2.2 Design of the microheater integrated with microsensor

The sensor is integrated into this micro heater. It is expected to measure the average temperature surrounding the bubble cavity. The structure of microheater (red layer), lead-out layer (yellow) and integrated sensor (green) are depicted in Figure 3.9.

The technical specification of the design of microheater and microsensor are given in Table 3.2.

Table 3.2: Technical specifications for microheater and microsensor.

Specification	Value
Cavity diameter (μm)	40
Pt wire spacing (μm)	10
Width of Pt heater wire (μm)	40
Heater length (mm)	11.9
Heater area (%)	47.6
Heater resistance (Ω)	400
Pt thickness (μm)	140
Pt film ρ ($\text{n}\Omega\cdot\text{m}$)	465

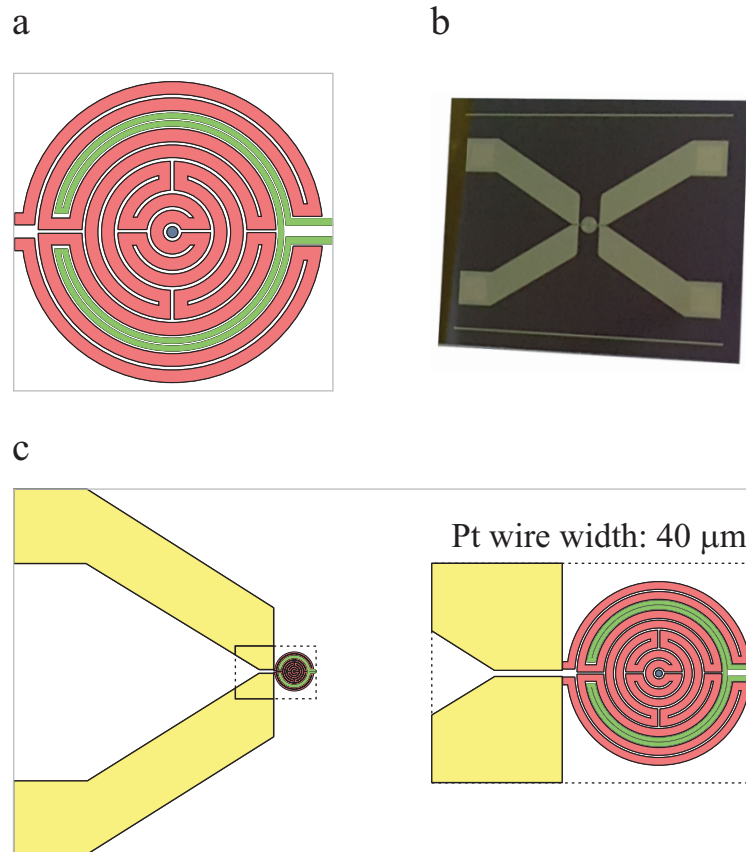


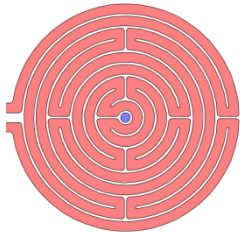
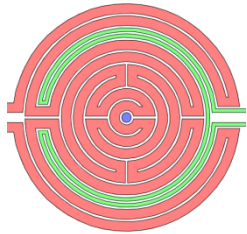
Figure 3.9: (a) Structure of microheater (red layer), lead-out layer (yellow) and integrated sensor (green), (b) Real image of the substrate, (c) The leading wire position on the substrate.

The resistance is calculated from Eq. (3.6) as follows.

$$\frac{R_{Pt}}{R_{Au}} = \frac{10.6}{2.44} \times \frac{11.9}{8.4} \times \frac{600}{40} = 92. \quad (3.6)$$

The designs of all fabricated microheaters are summarised in Table 3.3.

Table 3.3: Summary on the micro-heater/sensor design.

Design	Design I	Design II
Icon		
Cavity diameter (μm)	40	40
Pt wire spacing (μm)	10	10
Sensor wire width (μm)	-	15
Heating wire width (μm)	40	40
Pt area %	57.6	47.6
$\frac{W_{Au}}{W_{Pt}}$ at interconnection	15	15
$\frac{R_{Pt}}{R_{Au}}$	>112	>92

3.3 Fabrication of an array of actuators on silicon substrate

3.3.1 Array of single pillars

In this section, a method to fabricate a pattern of nickel pillar is introduced. Nickel wire was used as one of the main parts of the pillar due to its good magnetism properties. Nickel can also work well in boiling liquid without rusting, so that it will not contaminate the working liquid.

The basic idea is to keep the nickel wire standing onto silicon substrate using PMDS as an elastic glue. By this way, the nickel wire can be actuated by standing on an elastic layer of PMDS and its bending angle depend directly on the stiffness of this PDMS layer. In this experiment, we used the ratio 30:1 for PMDS and curing agent, whose young modulus E is much smaller than the standard ratio 10:1. This reduced ratio can increase the flexibility of PMDS up to 10 times [131].

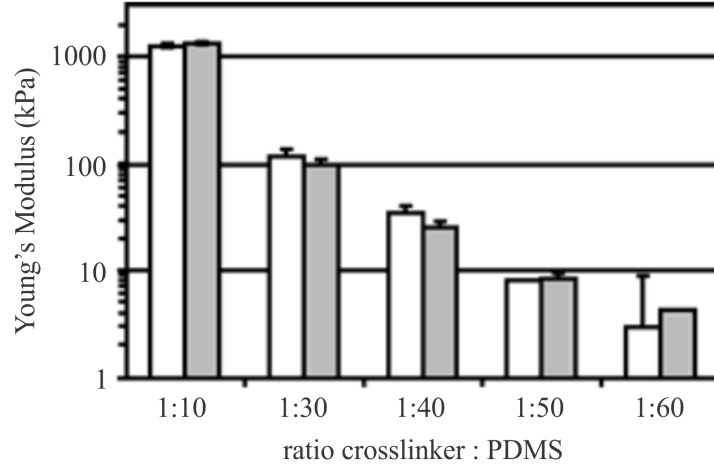


Figure 3.10: Young Modulus E depend on the ratio Crosslinker:PDMS. [131]

Nickel wire (AWG30, $d_{Ni} = 120 \mu\text{m}$) was cut into small pillars with the length of 1 mm. To ensure each pillar has the same length, they were put in one line and being cut at the same time by a shape blade. A thin layer of PDMS ($50 \mu\text{m}$) was then spin-coated onto a glass slide. A magnet was kept under this glass slide and its magnetic field allowed the nickel pillar to stand on the liquid PDMS layer. The nickel pillar had its bottom end wetted with a thin layer of liquid PDMS and it was ready to be put on the substrate.

After preparing the Nickel pillars, we prepared a platform to locate the pillars into the pre-defined array as shown in Figure 3.11. A pattern of holes was drilled on an acrylic mould. These holes were filled with magnetic micro particles (MQFP-15-7, $5 \mu\text{m}$ average size), forming an array of magnetic material column. A strong magnet (0.6 T) was then put under the acrylic mould and the silicon substrate was also placed on top of the mould at the same time. The magnetic material

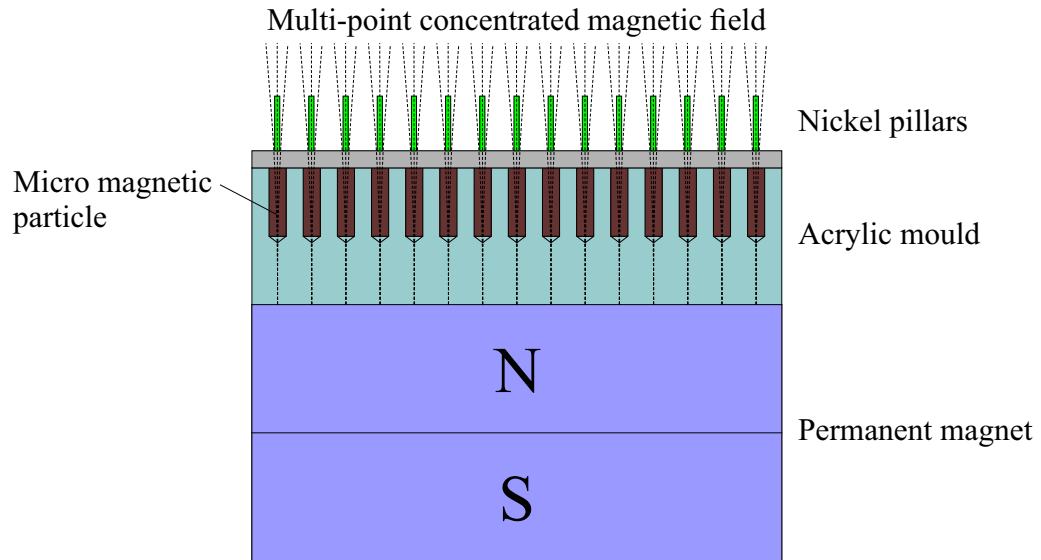


Figure 3.11: Setup to locate the array of nickel pillars on silicon substrate.

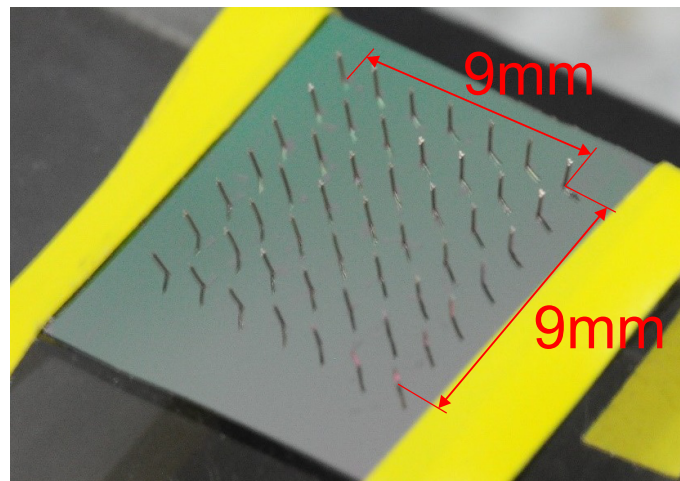


Figure 3.12: A sample of nickel arrays on silicon substrate.

column on the mould focused the magnetic line from the magnet into a point-array of concentrated field, right on the surface of the substrate. This allows the nickel wire to stand on the substrate with its bottom end attracted to these adjacent field-concentrated points. Finally, each nickel pillar was dropped through a capillary tube ($d_{cap} = 500 \mu\text{m}$) onto the substrate by mini CNC machine. Although the diameter of the capillary tube is larger than that of the pillars, they can be located well on the substrate due to the local concentrated field. The whole setup including the magnet was kept inside the oven for 2 hours at $80 \text{ }^\circ\text{C}$ for curing of PDMS. After PDMS on the bottom of nickel pillars was cured, the magnet can be removed. A sample of nickel arrays on silicon substrate is shown in Figure 3.12.

3.3.2 Array of Nickel strips

The array of Nickel pillar had been tested and it was working properly with good response to the external magnetic field. However, the demands of increasing flow rate inside the liquid body might also need the effect of actuation to be even stronger. To achieve this requirement, we have come up with another structure which has not only a better flexible joint of the actuator but also a wider affected area to the inner liquid flow: an array of nickel strip.

First, the fabrication for this kind of Ni strip cannot use the previous idea used on single pillar arrays. The reason is that the strip cannot be align very well with magnetic field line as a single pillar. Even if one strip can be place that the right position, the other strip will affect the position of the previous strip inside that magnetic field. Therefore, the only approach that we found it useful is to put the strip onto the substrate surface using a mini CNC machine, which help to grab and position the strip to the right position.

Each Ni strip actuator is cut out for a larger sheet of Nickel, which have the thickness of $200 \mu\text{m}$. This piece of Ni strip will then be attached with a nickel wire using wet PDMS mixture, which is chosen due to its elastic durability, cleanliness and low thermal conductivity. This PDMS mixture should need to be rigid, so the mixing ratio of PDMS and curing agent will be 5:1. The parts will be put into the oven at $80 \text{ }^\circ\text{C}$ for 1 hour for drying out. Next, a pair of $150 \mu\text{m}$ flat needle tip will be cut out to a length of 1 mm and put on the two ends of the Ni wired. This whole part will be put on the grabbing mechanism (on the CNC machine) to place it to

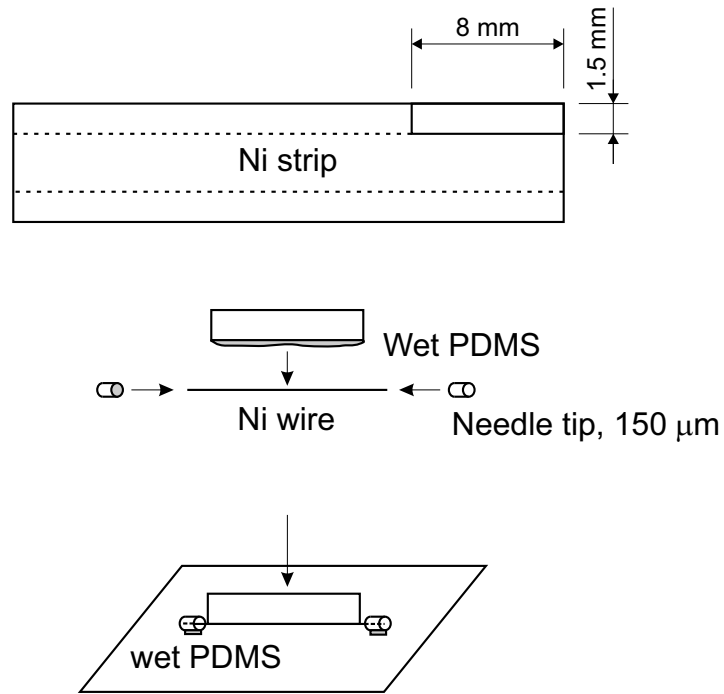


Figure 3.13: The fabrication of an array of Nickel strips.

the right position on the substrate.

After that, a thin layer of wet PDMS will be applied on the interface between the needle and substrate. The whole parts will be kept steady for 1 hour under 80 °C for fast solidified of the PDMS (the substrate is put on the CNC table, which is also assembled with a heater). After the process for one strip finished, the other strips were continued to be placed on the substrate.

Chapter 4

Heat transfer enhancement on passive nano-structured surfaces

In this chapter, we would like to focus on the experiment of pool boiling on passive micro-structured surface and its mechanism. There will be three main contents: data validation for the pool boiling setup, properties of the experiment substrate and the results and discussion section. The last section will include a predictive model for critical heat flux and critical surface temperature.

4.1 Experiment procedure and data validation for pool boiling

In this section, the first design of the boiling rig for pool boiling as well as the measurement procedure for pool boiling on passive structured surface will be tested and validated. Before getting to the validation results, all the necessary contents related to the experiment procedure will be discussed in detail.

4.1.1 Experimental scheme

The experimental setup consists of three sections: heating, testing and condensation (see Figure 4.1). In the heating section, a cartridge heater embedded in a cylindrical of copper rod is used to generate heat. The copper rod is insulated from the surrounding environment by a Teflon holder. In the testing section, a boiling substrate, which is either smooth silicon wafer or a nanopillar substrate, is placed between the

copper rod and a glass cuvette of lateral size 10 mm×10 mm. The test substrate is cleaned by ethanol and acetone in an ultrasonic bath and rinsed with distilled water before each experiment. The cuvette is filled with degassed FC-72 as a working liquid. The cuvette is enclosed by a stainless-steel container; the gap between the cuvette and the container is circulated with hot water of temperature $55.5\pm 0.5^\circ\text{C}$ to keep the temperature of the working liquid close to boiling point. The container has two glass windows on two opposite sides allowing optical recording of the boiling phenomena. A condenser is placed on top of the container to collect vapour generated from the working liquid. The cooling power of the condenser is adjusted to keep the vapour pressure inside the cuvette at atmospheric pressure. The vapour pressure is measured by pressure transducer (Gefran, working range 0 - 6 bar, accuracy $\pm 0.5\%$ full scale, analog output 10VDC) and maintained at atmospheric pressure by adjusting the cooling power of a Peltier unit.

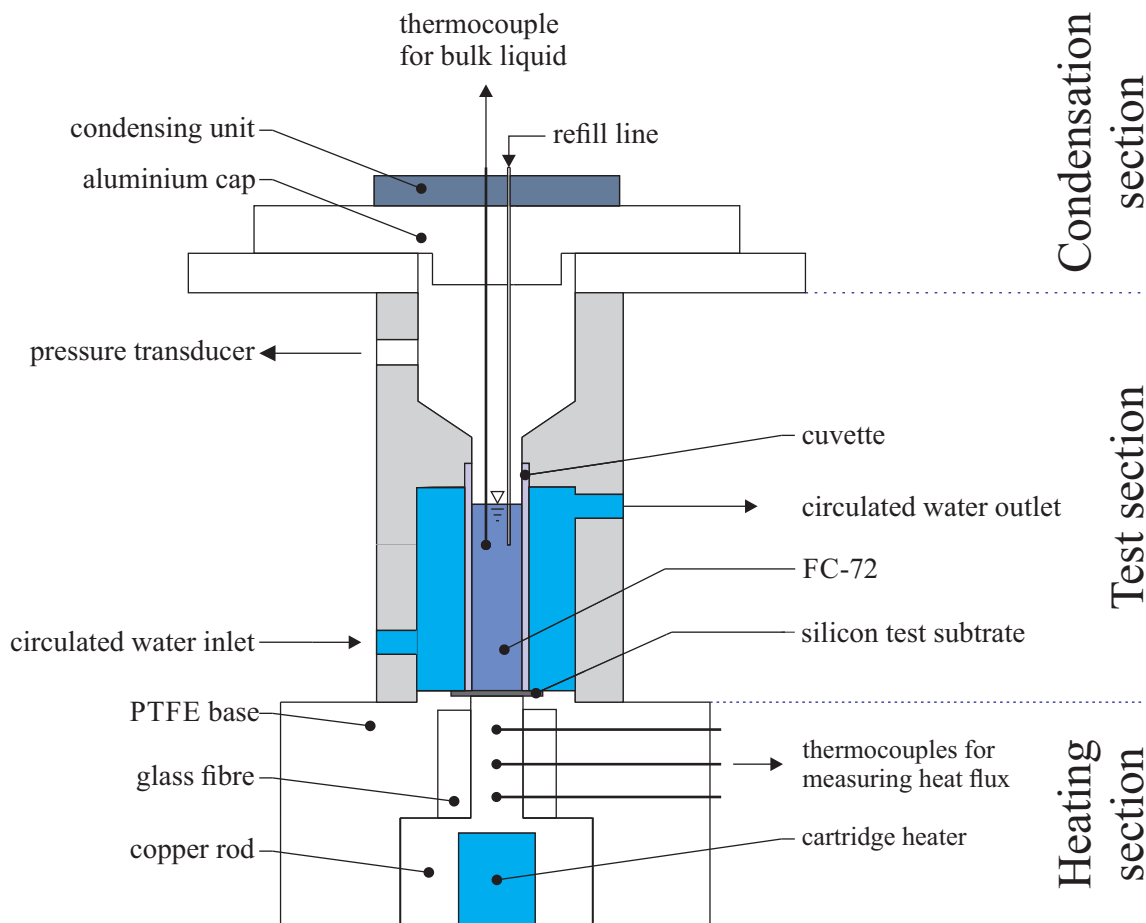


Figure 4.1: The schematic of boiling set up experiment.

Three thermocouples were inserted vertically at three points along the heating direction. The heat flux through the substrate was interpolated by three-points forward and backward differences interpolation. Signals from the thermocouple and the pressure transducer are read by a Keithley DMM device before being ready for calculation of heat flux and wall superheat. The boiling process is recorded by a high-speed camera (SA-5, Photron) at 5000 frames per second. The scheme of parameter controlling, and measurement is described in Figure 4.2.

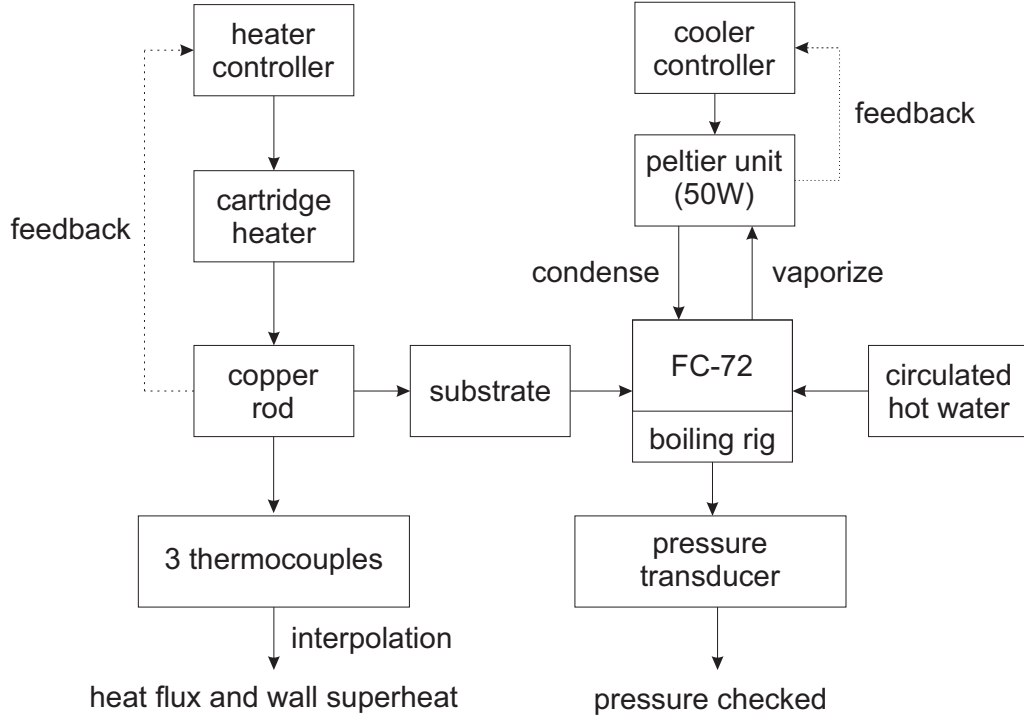


Figure 4.2: The schematic of parameter controlling and measurement.

4.1.2 Heat flux and wall superheat interpolation

The eat flux q through the substrate and surface temperature T were interpolated by three-points forward and backward differences interpolation methods:

$$q = -k_c \frac{3T_3 - 4T_2 + T_1}{2\Delta x_c}. \quad (4.1)$$

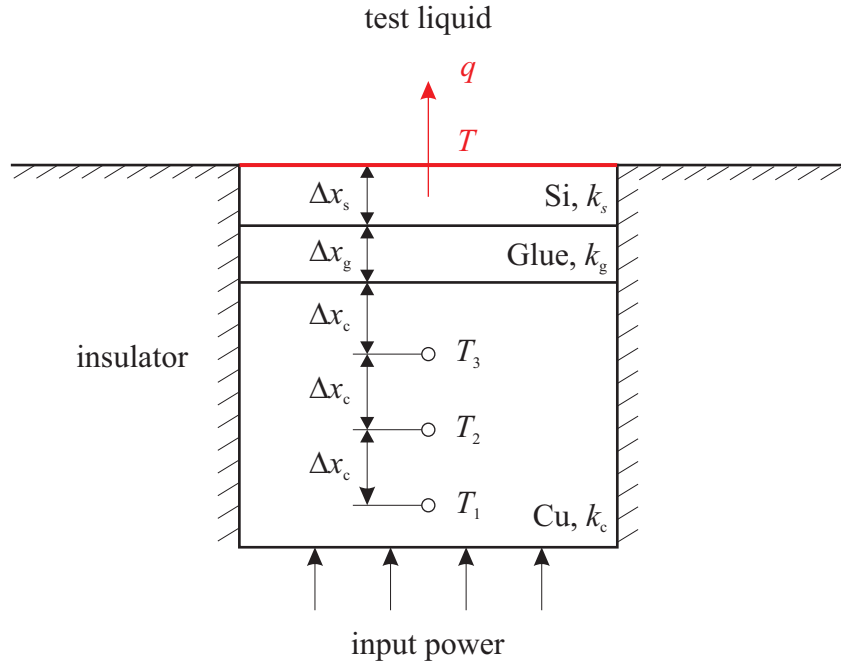


Figure 4.3: Heat flux measurement.

$$T = T_3 - qR. \quad (4.2)$$

$$\Delta T = T - T_{sat}. \quad (4.3)$$

Here q is the heat flux through the substrate surface; T is the surface temperature; k_c , k_s and k_g are the respective thermal conductivities of copper, silicon wafer and glue. Also, Δx_c is distance from thermocouple T_3 to bottom of glue layer and Δx_g and Δx_s are thicknesses of thermal glue layer and silicon substrates respectively. The heat resistance, R , from the third thermocouple (T_3) to substrate surface is calculated as follows. The physical properties of components in the boiling rig are tabulated in Table 4.1.

$$R = \frac{\Delta x_c}{k_c} + \frac{\Delta x_g}{k_g} + \frac{\Delta x_s}{k_s}. \quad (4.4)$$

Table 4.1: The physical properties of components in the boiling rig.

Physical properties	Notation	Value
Thermal conductivity of copper ($\text{W}\cdot\text{m}^{-1}\cdot\text{K}^{-1}$)	k_c	400
Thermal conductivity of thermal glue ($\text{W}\cdot\text{m}^{-1}\cdot\text{K}^{-1}$)	k_g	1.8
Thermal conductivity of silicon substrate ($\text{W}\cdot\text{m}^{-1}\cdot\text{K}^{-1}$)	k_s	131
Distance between thermocouples (mm)	Δx	7
Gap between T_3 and the bottom of glue layer (mm)	Δx_c	7
Thickness of thermal glue layer (mm)	Δx_g	0.01
Thickness of silicon substrate (mm)	Δx_s	0.5

4.1.3 Results on pool boiling validation

The boiling point of FC-72 is 56°C at atmospheric pressure, which was considered as the initial temperature to begin the experiment. For each tested substrate, the heat flux q and the corresponding superheat $\Delta T = T - T_{sat}$ were measured when the system is in the steady state and with temperature steps of 5 K. The experimental uncertainty is obtained by repeating the experiment three times.

The measurement procedure and analysis are validated by comparing the heat transfer data obtained on the smooth Silicon substrate to the well-known dataset obtained by Ujereh *et al* [132], as well as to classical model, including the one for nucleate boiling heat transfer by Rohsenow [133] and the one for critical heat flux by Zuber [134] (see Figure 4.4). In particular, the critical heat flux on a smooth substrate is:

$$q_c^s = K \rho_v^{1/2} h_{fg} [g\sigma(\rho_l - \rho_v)]^{1/4}, \quad (4.5)$$

where $K \approx 0.131$ is an empirical parameter. The other details on Rohsenow and Zuber model are described in Appendix B

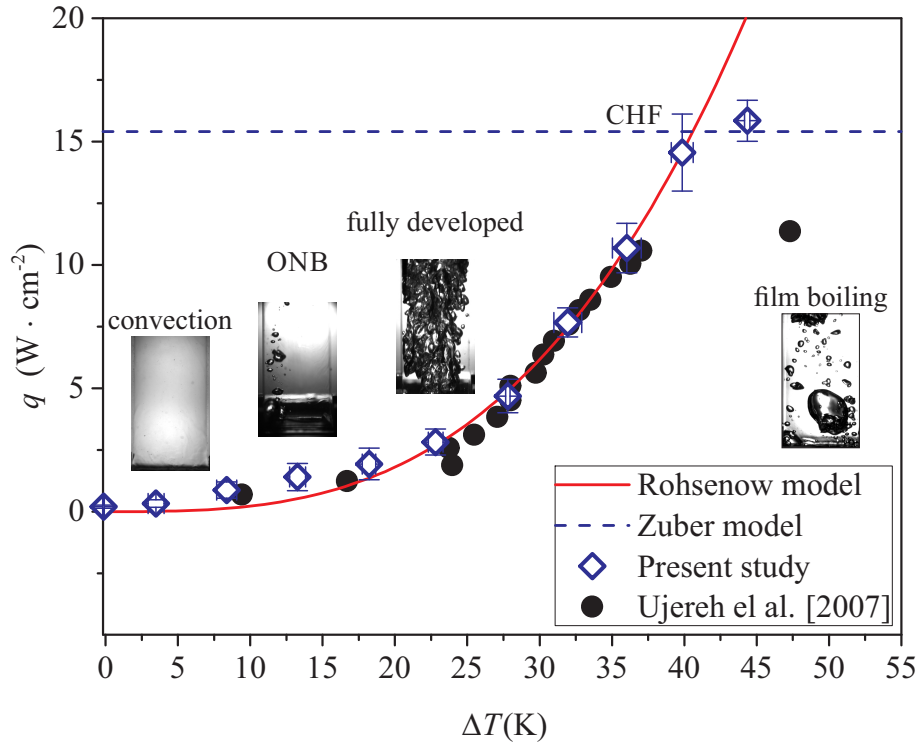


Figure 4.4: Boiling curve of bare silicon with Zuber and Rohsenow models.

4.2 Properties of experimental substrates

The test substrates were made by a collaborate group at the University of Pittsburgh, USA. We would like to present about their fabrication step and its advantage in Appendix A. Here we will describe the nanopillar array on the substrate surface in terms of geometric structure and other important parameters such as surface area enhancement ratio, dimension of pillars and array pitch.

Geometric structure of experimental substrate.

The substrate surface used in this experiment was modified by an array of silicon nanowire/pillar (SiNW) which is uniformly distributed on the surface as shown in Figure 4.5. The height l of nanopillars will be varied over four substrates. The surface area enhancement ratio r of each substrate will be calculated as their characteristic parameters.

Surface area enhancement ratio of nanopillar substrate.

The surface area enhancement ratio r of the substrate was calculated using the geometry profile of each substrate, including the pillar height l . The ratio $r = A_1/A_0$ was used to evaluate how much the surface has been modified, in term of

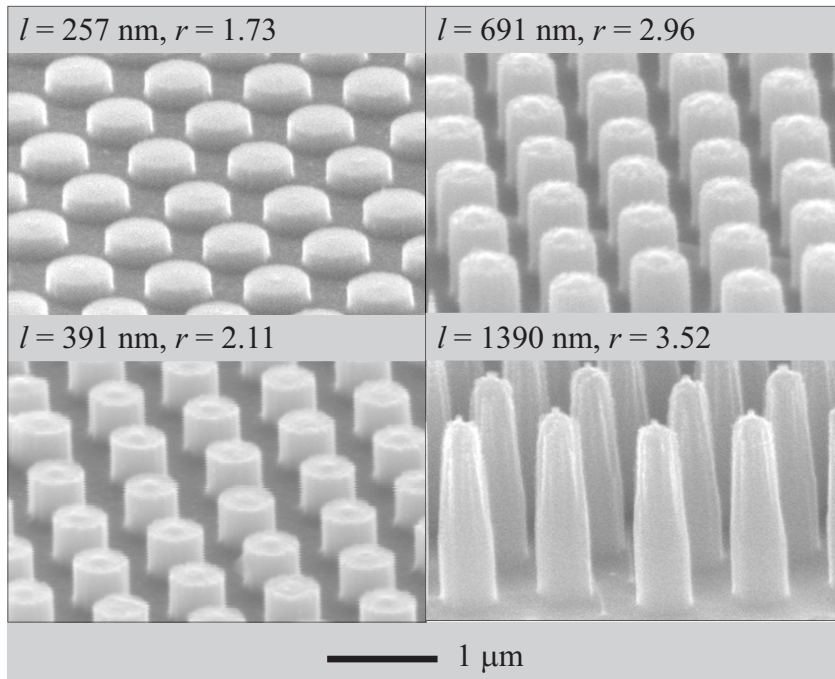


Figure 4.5: SEM images showing nanopillar substrates of different pillar heights l and corresponding surface area enhancement ratio r .

effective area over total area. The definition of total effective enhancement area A_1 is described in Figure 4.6.

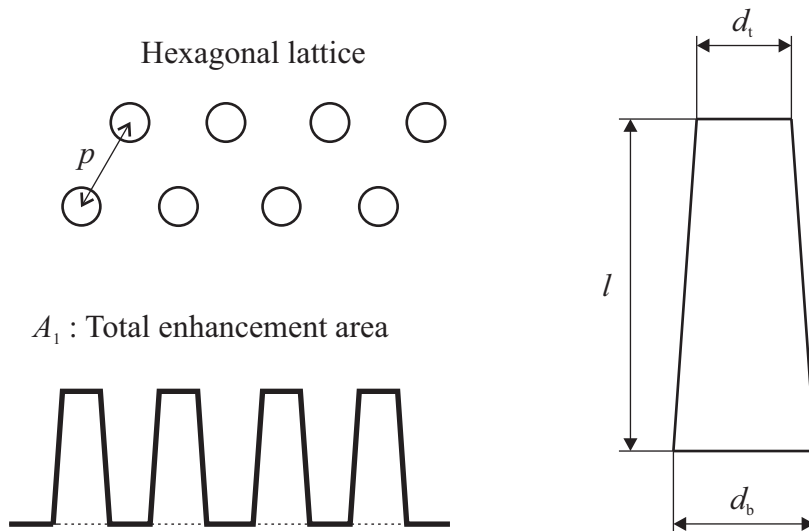


Figure 4.6: Total effective enhancement area A_1 (bold line)

The surface area of a single tapered nanowire:

$$A_{bottom} = \frac{\pi d_b^2}{4} \quad (4.6)$$

$$A_{top} = \frac{\pi d_t^2}{4} \quad (4.7)$$

$$A_{side} = \frac{\pi(d_t + d_b)}{2} \sqrt{l^2 + \frac{(d_t - d_b)^2}{4}} \quad (4.8)$$

Number of nanowires on an area of $A_o = 15 \times 8 \text{mm}^2$:

$$n_{NW} = \frac{2A_o}{p^2 \sqrt{3}} \quad (4.9)$$

The total effective enhancement area, A_1 of the nanowire surface is calculated as follows.

$$A_1 = A_o + n_{NW} \times (A_{side} + A_{top} - A_{bottom}) \quad (4.10)$$

where A_o is the area of plain Si substrate $15 \times 18 \text{ (mm}^2\text{)}$.

The calculation results for the surface area enhancement ratio $r = A_1/A_o$ is shown in Table 4.2.

Table 4.2: Surface area enhancement ratio r calculated for each substrate.

Substrate	Height l (nm)	Total surface area A_1 (nm²)	Surface area enhancement ratio r (A_1/A_o)
1	257	4.669e+14	1.73
2	391	5.696e+14	2.11
3	691	7.994e+14	2.96
4	1390	9.501e+14	3.52

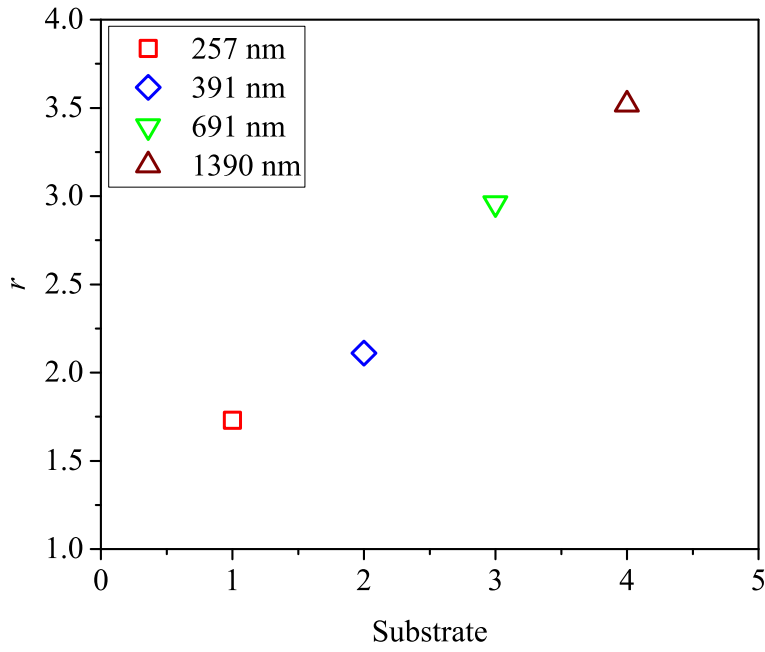


Figure 4.7: Properties and surface area enhancement ratio r of four substrates.

4.3 Results and discussion.

4.3.1 Experimental result and observations

To qualitatively evaluate the effect of the nanopillars on boiling, we first compare the boiling behaviours between the smooth substrate and the nanopillar substrate with $l = 1390$ nm at several surface temperatures T (Figure 4.8).

Although the onset of boiling occurs at $T \approx 69^\circ\text{C}$ for both substrates, the size of bubbles generated on the smooth substrate varies much more broadly than that on the nanopillar substrate. At higher temperature, the bubble dynamics on the two substrates become even more contrasting: while the bubbles on the smooth substrate tend to merge and create either large bubbles or vapour columns starting from the substrate, those generated on the nanopillar substrate have much lesser tendency to merge and appear more uniform in size. We note that it is not likely for bubbles to coalesce after their detachment from the substrate due to liquid inertia and surface tension, thus the coalescence process mainly occurs between consecutive bubbles generated from the same nucleation site before detachment.

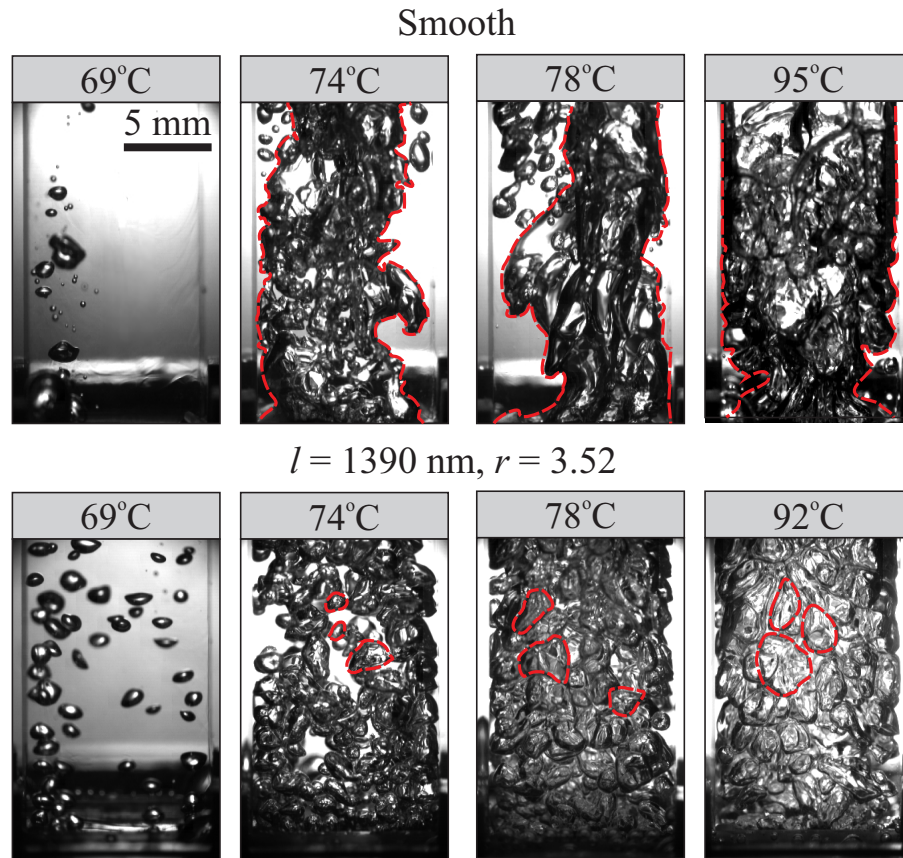


Figure 4.8: Representative snapshots showing boiling phenomenon on the smooth substrate (top panel) and the nanopillar substrate with $l = 1390 \text{ nm}$ (bottom panel) at several surface temperatures T . While the smooth surface produces vapour bubbles which have tendency to coalesce (e.g., at $T = 74^\circ\text{C}$) and form vapour columns (e.g., at $T = 78^\circ\text{C}$), the nanopillar substrate produce bubbles which have a narrow size distribution and tend to evolve separately without merging. The vapour column and bubbles are highlighted by red dashed lines.

This strongly suggests that resistance to coalescence, as well as the uniform size of bubbles generated from the nanopillar substrate result from an effective rewetting process, which facilitates bubble detachment from the surface. We hypothesise that deviation in boiling behaviours of nanopillar substrates from the smooth one, therefore, originates from the nanopillar-induced enhancement in the rewetting process.

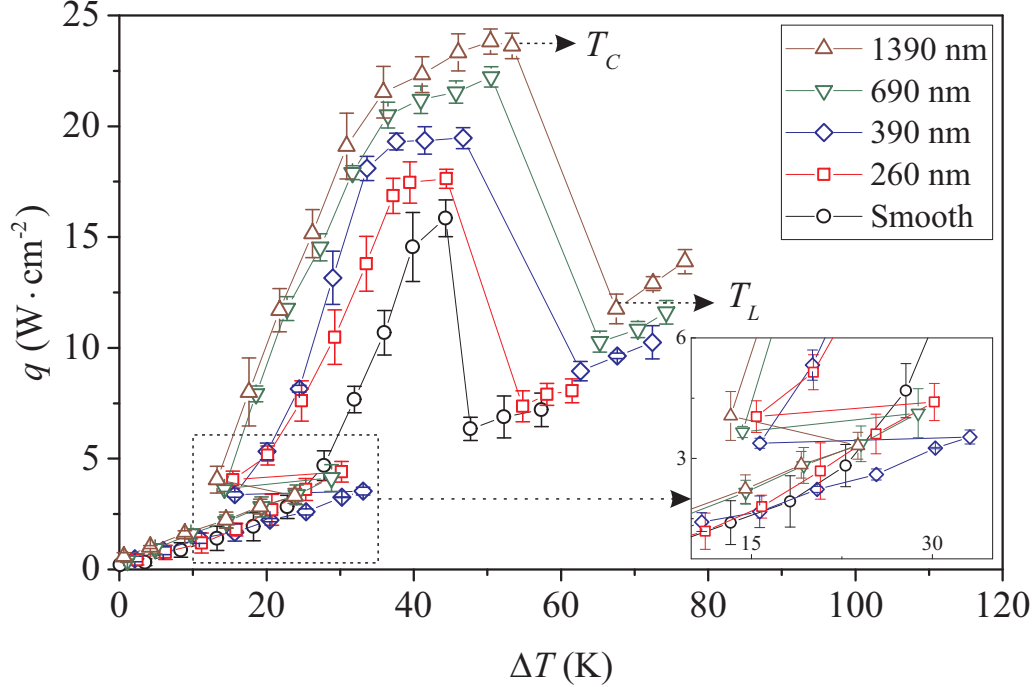


Figure 4.9: Heat flux q versus wall superheat ΔT for smooth and nanopillar substrates. Error bars represent the standard deviation from multiple experiments.

We now quantify the effect of nanopillars on the boiling performance by measuring the heat flux q for each substrate as a function of the superheat $\Delta T = T - T_{sat}$, where $T_{sat} = 56^\circ\text{C}$ is the saturation temperature of FC-72 at atmospheric pressure. In Figure 4.9, we show the dependence of q on ΔT for the smooth and all the nanopillar substrates (See Appendix C for the uncertainty analysis of the heat flux and surface temperature measurements). Starting from $\Delta T = 0$, q first gradually increases due to natural convection until it reaches the onset of nucleate boiling ($\Delta T \approx 30$ K for all tested substrates). In this so-called natural convection regime, since the nanopillars are much smaller than the thermal boundary layer thickness, their presence causes negligible effect to the heat flux, which is dictated by the con-

vective liquid flow outside of the thermal boundary layer. Here, the boundary layer thickness is roughly $57 \mu\text{m}$, estimated using the ratio between the natural convection heat transfer coefficient and the thermal conductivity of FC-72 [135].

As ΔT increases past the onset of nucleate boiling, the heat flux on nanopillar substrates, denoted as q^n , deviates substantially from that on the smooth substrate. In particular, q^n after the system transitions into the nucleate boiling regime is achieved at much lower superheat compared to that when system is still in the natural convection regime (inset of Figure 4.9). For instance, for the substrate with $l = 390 \text{ nm}$, $q = 3.3 \text{ W} \cdot \text{cm}^{-2}$ is achieved at $\Delta T \approx 16 \text{ K}$ when the system is in the nucleate boiling regime, whereas a slight increase in heat flux, $q \approx 3.5 \text{ W} \cdot \text{cm}^{-2}$, is achieved at much higher superheat $\Delta T \approx 33 \text{ K}$ in the natural convection regime. On the smooth substrate, however, the heat flux increases *smoothly* as the system transitions into the nucleate boiling regime. The presence of nanopillars causes a substantial jump in heat flux as soon as the system transitions to the nucleate boiling regime because the heat transfer mechanism is more efficient for the nanopillar substrates. The homogeneous spread of nucleation sites, high generation frequency and narrow size distribution of bubbles on nanopillar substrates (see Appendix D, Figure D.1) results in the sudden discontinuity in the boiling curve.

With the superheat increasing beyond the onset of nucleate boiling, bubbles are generated with higher frequency and larger size, intensifying forced convection in the bulk liquid and subsequently enhancing the heat flux q . For each substrate, q increases to the CHF q_c at the critical temperature T_c , beyond which it drops sharply due to excessive vapour generation and lack of replenishing liquid to the substrate. The heat flux reaches its minimum value at the so-called Leidenfrost temperature T_L , or the upper limit of nucleate boiling. The sudden drop in heat flux at T_L often triggers drastic spike in surface temperature causing the notorious “burn-out” in boiling applications. Thus, designing heat-dissipating substrates with high T_L is as practically important as enhancing the critical heat flux.

We observe considerable enhancement in both q_c and T_L on nanopillar substrates. In Figure 4.10, the dependences of q_c and T_L on the surface area enhancement ratio r are shown. Both q_c and T_L increase monotonically with increasing r (or equivalently with pillar height l). Compared to the smooth substrate ($r = 1$), q_c and T_L on the nanopillar substrate with $r = 3.5$ increase $\approx 50\%$ and $\approx 25^\circ\text{C}$, respectively.

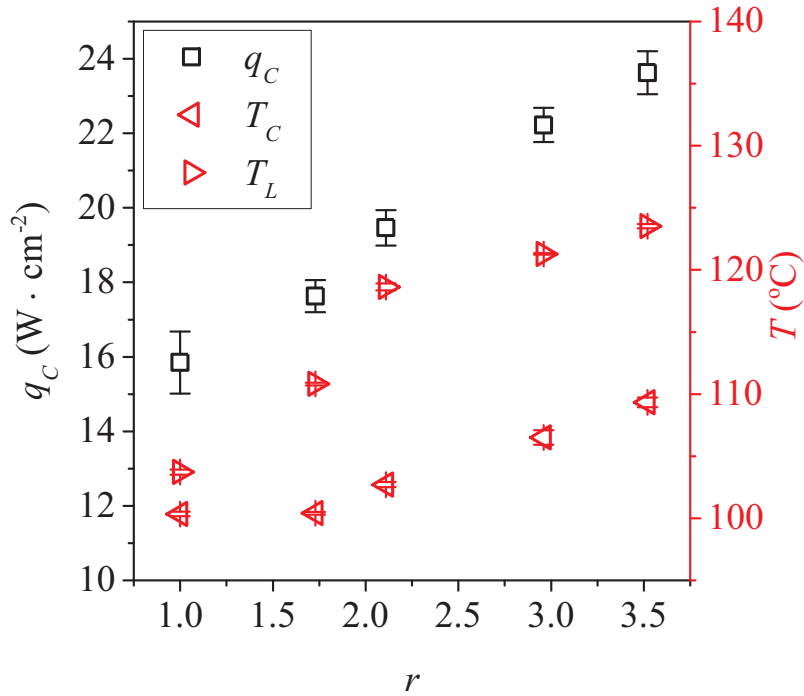


Figure 4.10: Dependence of critical heat flux q_c (open squares), CHF temperature T_c (left-pointing triangles), and Leidenfrost temperature T_L (right-pointing triangles) on surface area enhancement ratio r .

The enhancement in both q_c and T_L is a remarkable feature of the nanopillar substrates as opposed to those fabricated with larger scale structures. It was observed that micro-structures only enhance the heat flux without increasing the Leidenfrost temperature; typically, T_L decreases with increasing height of microstructures [136]. Separate investigations on hierarchical substrates, i.e., microstructured surfaces covered with nanograss, reported enhancement in *either* the Leidenfrost temperature [137–139], or the heat flux [121, 140, 141, 99, 142, 138, 143, 144].

4.3.2 Mechanism of heat transfer enhancement on nanopillar substrates.

To control the effects of nanopillars on enhancing q_c and T_L , we now investigate the heat transfer mechanism on nanopillar substrates. From qualitative observations of the differences in bubble generation between the nanopillar substrates and the smooth one, we postulate that the major contributing factor leading to the observed change in q_c and T_L is the nanopillar-induced rewetting process. We note that in

the case of hierarchical structured surfaces, i.e., micro-structures covered by nanograss, enhancement in q_c was observed, but due to a very different mechanism: the enhancement in volume of liquid wicking through the microstructures brings more liquid to the surface and subsequently leads to an increase in heat flux by latent heat of evaporation. The wicking process, however, is not possible for nanopillars due to the tremendous viscous stress induced in flows confined in such small length scales between pillars [121]. Thus, wicking is excluded as the cause of heat flux enhancement for our nanopillar substrates, which have inter-spacing between pillar ≈ 360 nm.

We focus on the advancing contact line of liquid to explore how the nanopillar-induced rewetting process leads to heat transfer enhancement. Taking advantage of the similarity between the rewetting process of vapour bubbles and the spreading process of liquid (illustrated in Figure 4.11a), the dynamics of the advancing contact line can be studied separately in the case of spreading liquid on nanopillar substrates [120, 145]. We note that the rewetting process has been the focus of numerous detailed studies [121], which revealed contributing factors such as surface-induced capillary force [121], hydrostatic and hydrodynamic forces [145], reshaping effects [146] and vaporisation [147]. For the nanopillar substrates, we determine the dominant effects and their contribution to the heat transfer by investigating the spreading of liquid from a capillary tip onto heated substrates (see Figure 4.11a). The details setup of this extra experiment are described in the appendix, section A.7. By varying the surface temperature and tracking the three-phase contact-line (TCL) as the liquid spreads, we determine the temperature dependence of the apparent spreading velocity v_s on each nanopillar substrate.

The surface temperature can be varied from room temperature $T_r = 20^\circ\text{C}$ up to 46°C without causing the liquid to boil. Although the displacement of the TCL results from various coupled effects, we simplify the analysis by decomposing v_s into several independent components (Figure 4.11b):

$$v_s = v_{ca} - v_n - v_h, \quad (4.11)$$

where the component v_{ca} is caused by capillary force on the substrate and therefore is a function of the surface area enhancement ratio r only. The component

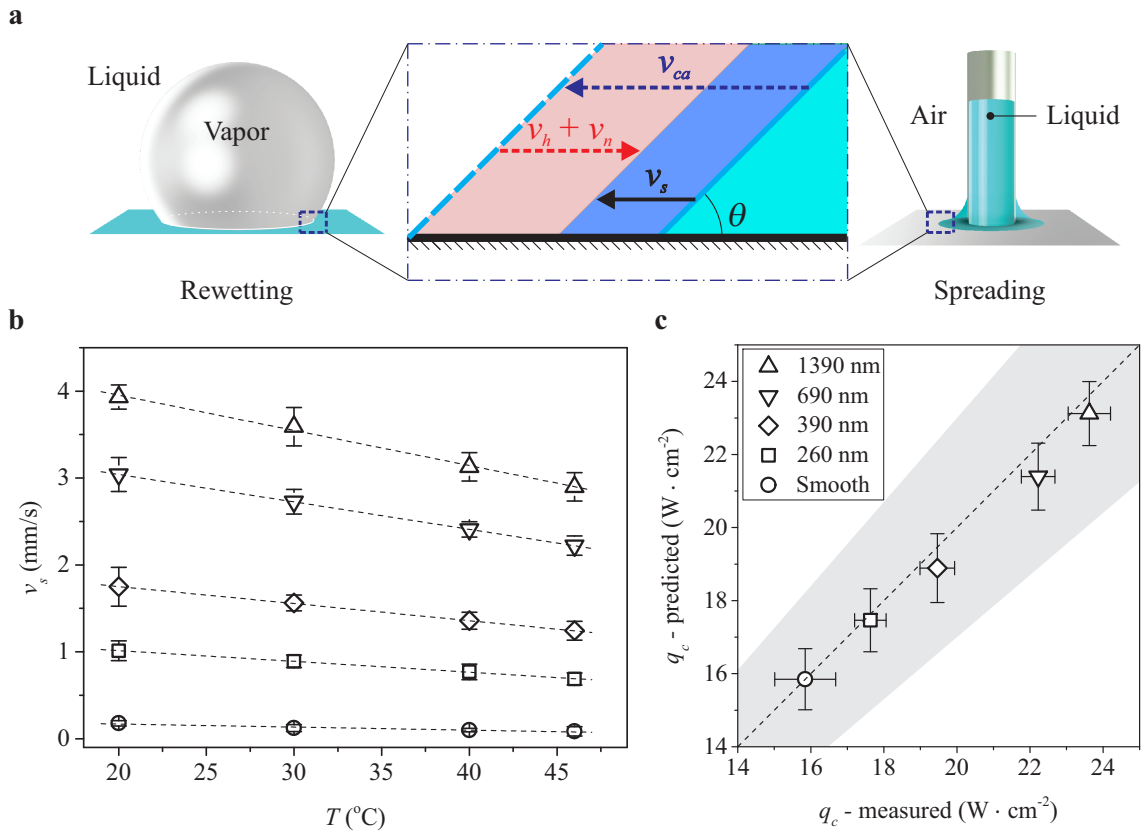


Figure 4.11: (a) Schematics showing similarities between the rewetting process in pool boiling (left panel) and the spreading process (right panel) from a capillary, in particular at the three-phase contact line (highlighted in the middle panel). (b) Apparent spreading velocity v_s of FC-72 on different substrates over a range of temperature from 20 °C to 46 °C. (c) Critical heat flux q_c predicted using Eq. (4.12) versus the measured values for smooth and nanopillar substrates. The uncertainty for the predicted heat flux comes from that of the spreading velocity measurements. The shaded area indicates a 15% deviation from the measured data.

v_h represents the reduction in spreading velocity as liquid absorbs heat from the surface and evaporates. Thus, if the substrate is not heated, i.e., $T = T_r$, it follows that $v_h = 0$ because there is no heat transferred from the surface to the liquid. The velocity component v_n represents the reduction in spreading velocity due to natural evaporation of liquid. In the case of liquid spreading in air, this component is nonzero and depends on the partial pressure of vapour, whereas in the case of boiling, it vanishes as bubbles generated during boiling of liquid are filled only with saturated vapour. Here, we have neglected contributions to TCL displacement from hydrostatic pressure of the liquid column, and from capillary pressure at the upper liquid surface in the tube due to the small gap between the capillary tube and the substrate.

We postulate that the increase in heat flux on nanopillar substrates results from nanopillar-induced enhancement in wetting. This is suggested from the linear correlation between the critical heat flux of different substrates and the spreading velocity v_s measured on respective substrates at surface temperature $T = 20^\circ\text{C}$ (see Appendix, Figure F.1). In other words, the presence of nanopillars intensifies the rewetting process, leading to an added amount of liquid brought to and subsequently evaporated from the surface. Among the contributing components to the apparent spreading velocity, v_{ca} inherits the effect of r on capillary wetting, thus has a direct relation to the enhanced rewetting process. In addition, as the surface temperature for spreading liquid was set lower than the liquid's saturation temperature, we assume that with constant surface temperature, v_n remains fixed for all the substrates, i.e., $v_n^n = v_n^s$, where the superscripts n and s respectively indicate quantities of the nanopillar substrates and the smooth one. We recall that v_{ca} is independent of T and $v_h(T_r) = 0$. As a result, at room temperature T_r , the spreading velocity difference $\delta v_s(T_r) = v_s^n(T_r) - v_s^s(T_r)$ between a nanopillar substrate and the smooth one *only* depends on the change in capillary velocity between the two substrates $\delta v_{ca} = v_{ca}^n - v_{ca}^s$. Thus, δv_{ca} can be estimated as $\delta v_{ca} \approx \delta v_s(T_r)$.

We measure the spreading velocity v_s for all nanopillar substrates and the smooth substrate (see Figure 4.11b). The spreading velocity increase $\delta v_s(T_r)$ is calculated for each nanopillar substrate to obtain δv_{ca} . The spreading velocity increases with increasing nanopillar height due to the increasing energetic favourability of wetted nanopillar surfaces of increasing height. The energy of the different dry nanopil-

lar substrates is approximately the same. However, the energy of different wetted nanopillar substrates decreases with increasing height due to the larger interface between the liquid and solid nanopillar array. This energy difference drives the spreading of the FC-72, and thus, the spreading velocity increases with increasing nanopillar height. We note that for a nanopillar substrate with projected boiling area A_p , the increase in capillary velocity δv_{ca} leads to a mass increase of evaporated liquid $\rho_l A_d \delta v_{ca}$, where A_d is the time-averaged dry area during boiling on A_p . At CHF, A_d can be estimated using the classic boiling model by Zuber [134]: $A_d = K A_p$, with $K \approx 0.131$ [134, 2, 148]. The enhancement in heat transfer at CHF, i.e., of a nanopillar substrate compared to the smooth substrate, can be calculated as $\delta Q_c = h_{fg} \rho_l A_d \delta v_{ca}$. As a result, we can estimate the heat flux at CHF, denoted as q_c^n , through each nanopillar substrate using that through the smooth one q_c^s and the heat flux enhancement $\delta Q_c / A_p = K \rho_l h_{fg} \delta v_{ca}$ as follows:

$$q_c^n = q_c^s + K \rho_l h_{fg} \delta v_{ca}. \quad (4.12)$$

We note that the heat flux at CHF on smooth substrates depends on the surface temperature and can be predicted using the classical model for nucleate boiling by Zuber [134]. A comparative study between the model and our boiling data on the smooth substrate shows a good agreement (see Appendix A for details). Thus, Eq. (4.12) provides a direct prediction of the heat flux through nanopillar substrates based on the enhancement in spreading velocity. In Figure 4.11c, we show a comparison between the heat flux predicted using Eq. (4.12) and one measured experimentally for all the substrates. The agreement between the predicted CHF and the measured values for all nanopillar substrates strengthen the hypothesis that the enhanced heat flux is caused by nanopillar-induced enhancement in rewetting. The results also suggest that the boiling crisis is mainly dictated by the intensity of the rewetting process, and the increase in critical heat flux is a direct consequence of the faster rewetting velocity using higher nanopillars.

4.3.3 Prediction of critical heat flux temperature on nanopillar substrates

We now explore how nanopillars-induced enhancement in rewetting affects the surface temperature T_c at CHF. Recall that the critical heat flux for nanopillar substrates can be predicted using that on the smooth substrate and the enhancement in rewetting velocity. We extend this argument to estimate T_c of nanopillar substrates. First, we determine the heat transfer coefficient h_{TCL} associated with liquid vaporisation at the three-phase contact line (TCL) by considering the volume Ω of liquid evaporated at TCL per unit time due to heat absorption from the nanopillar substrates. If we denote θ the contact angle of FC-72, Ω can be calculated as $\Omega = v_h A_d \tan \theta$ (see Figure 4.11a for illustration). On one hand, the rate of latent heat required to evaporate Ω is $\rho_l \Omega h_{fg}$. On the other hand, the heat rate supplied from the substrate is $h_{TCL}(T - T_l)A_d$, where T_l is the liquid temperature. Balancing the rate of latent heat of evaporation and the heat rate supplied from the substrate gives the energy balance $\rho_l \Omega h_{fg} = h_{TCL}(T - T_l)A_d$. Thus, the heat transfer coefficient h_{TCL} can be obtained by taking derivative with respect to T of the energy balance, assuming that h_{TCL} is independent of T : $h_{TCL} = \rho_l h_{fg} \tan \theta dv_h/dT$. Taking into account the relation between the spreading velocity v_s and v_h (Eq. (4.11)) and recalling that v_{ca} is independent of T , we have $dv_h/dT = dv_s/dT$, thus arrive at the equation to determine h_{TCL} for each substrate:

$$h_{TCL} = \rho_l h_{fg} \tan \theta \frac{dv_s}{dT}. \quad (4.13)$$

The central argument of the analysis for nanopillar-induced enhancement in heat flux is that the heat transfer increase takes place at TCL where capillary wetting and evaporation are significantly altered by the presence of nanopillars. As shown in Fig. 4.12a, h_{TCL} calculated using Eq. (4.13) increases linearly with the surface area enhancement ratio, or equivalently, the height of nanopillars. This implies that the enhancement due to both conduction at the solid-liquid interface and convection on nanopillar substrates are secondary effects. The total heat transfer coefficient h^n on nanopillar substrates can then be estimated using the total heat transfer coefficient h^s on the smooth substrate and the enhancement in heat transfer coefficient at TCL:

$$h^n \approx h^s + K(h_{TCL}^n - h_{TCL}^s) + C = h^s + K\rho_l h_{fg} \tan\theta \frac{d(v_s^n - v_s^s)}{dT} + C, \quad (4.14)$$

where the prefactor K is needed for the enhancement at TCL and the constant $C = 425 \text{ W} \cdot \text{m}^{-2} \cdot \text{K}^{-1}$ accounts for the additional heat transfer caused by the flow induced by displacement of bubbles from nanopillar substrates. Since there is no obvious difference in bubble dynamics between nanopillar substrates, we use a fixed constant C for all nanopillar substrates to represent the heat transfer increase due to displacement of bubbles. In deriving Eq. (4.14), we also assume insignificant variation in h between the spreading and boiling processes for a fixed substrate. We note that Eq. (4.14) can be applied at CHF due to the linear dependence of v_s on T (see Figure 4.11b). The heat transfer coefficient at CHF on the smooth substrate can be determined using the heat transfer balance $q_c^s = h^s(T_c^s - T_{sat})$, which gives $h^s = q_c^s/(T_c^s - T_{sat})$. Here T_c^s is the wall temperature at CHF on the smooth substrate and T_{sat} is the saturation temperature of the liquid. Similarly, we have $q_c^n = h^n(T_c^n - T_{sat})$, where T_c^n is the wall temperature at CHF on nanopillar substrates. Taking the predicted heat flux q_c^n and the heat transfer coefficient h^n on nanopillar substrates respectively from Eq. (4.12) and Eq. (4.14), T_c^n can be predicted as:

$$T_c^n - T_{sat} = \frac{q_c^n}{h^n}. \quad (4.15)$$

In Fig. 4.12b, we compare the predicted superheat temperatures $\Delta T_c = T_c - T_{sat}$ and the experimental ones at CHF for all substrates. Although the predicted values of ΔT_c carries the uncertainty of the spreading velocity measurement on nanopillar substrates, they fall within 15% deviation from the experimentally measured ones, highlighting a remarkable agreement between the predicted and experimental data.

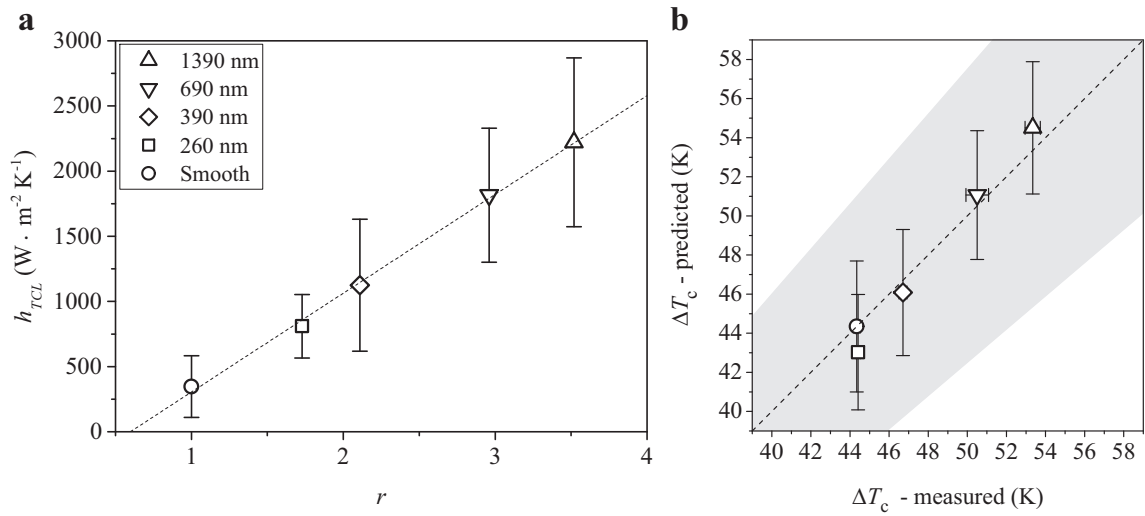


Figure 4.12: (a) Heat transfer coefficient at the three-phase contact line h_{TCL} versus surface area enhancement ratio r . (b) Critical heat flux temperature T_c predicted using Eq. (4.15) versus the measured values for different substrates. The shaded area indicates a 15% deviation from the measured data.

Chapter 5

Study of heat transfer enhancement on actuated strip arrays

In the nucleate boiling regime, vapour bubbles act like a huge number of micro-pumps, which efficiently take heat away from the hot surface to the bulk liquid above. There are several mechanisms for these “micro-pump” to work such as evaporation of microlayer liquid, micro-convection, transition conductive heat transfer. In a certain boiling process, the most dominant mechanism depends on the properties of its heating surface such as surface topology, heating scheme and liquid modification. Regardless of which mechanism is dominated in a boiling process, its effects can be visually observed by the change in bubble departure diameter and releasing frequency.

The natural convective regime in a boiling process, however, has only two main heat transfer mechanisms, including conductive heat transfer through the liquid body and convective inside the liquid bulk. These phenomena are more difficult to observe than the vapour bubble in nucleate regime.

In this section, we focus on convective heat transfer on an actuated strip-array. The convective heat transfer is expected to be driven by the actuated frequency of the strip-array. This assumption of heat transfer mechanism is discussed by high speed image recording before a model can be derived from the experimental results.

5.1 Experimental setup and procedures

In this experiment, the strip-array was actuated by a magnetic field from a couple of electro-magnet (24VDC, 25-50 mT, $f_{max}=200\text{Hz}$) attached on the boiling rig. Therefore, the second design of boiling rig was used to meet this requirement (details of the design are discussed in section 3.1.4). Once the substrate was installed, the working liquid (FC-72) was then filled into the cuvette to a constant level (25 mm). The condensing and heating module were activated at the same time to maintain a constant liquid level and atmospheric vapour pressure, which was followed by a pressure transducer attached on the condensing module. The average liquid temperature was also measured during the experiment by three thermocouples placed at different position inside the bulk liquid. (see Figure 5.1).

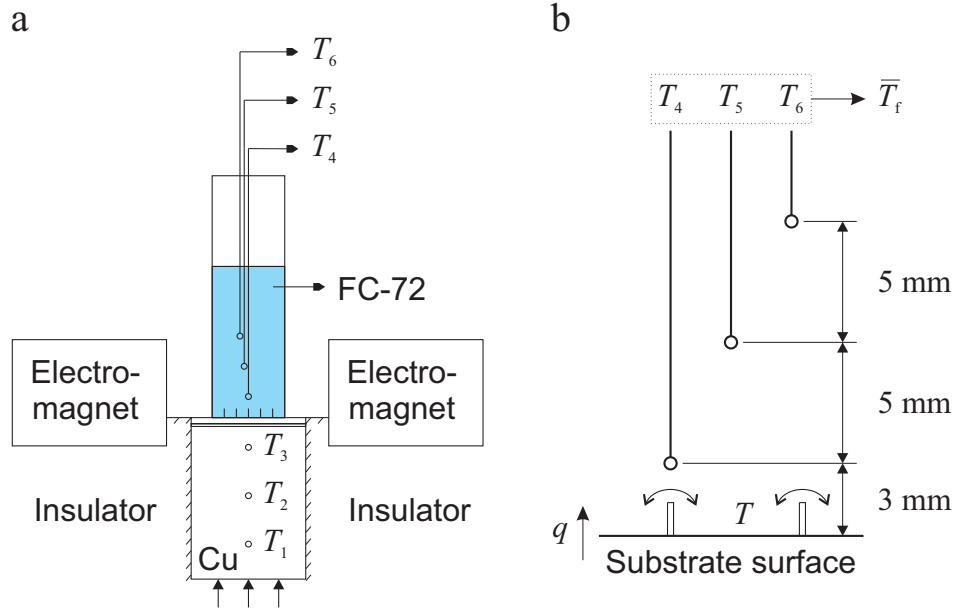


Figure 5.1: A simplified schematic drawing of the setup. (a) Positions of temperature measured and arrangement of experimental setup and (b) Position of three thermocouples put inside the liquid bulk.

First, the substrate was heated by gradually increasing the setting temperature, so that temperature on substrate surface T was stable at the target temperature. The temperature at different positions from T_1 to T_6 (Figure 5.1) was measured and recorded by a Keithley data multimeter and switching system. Heat flux q and wall

temperature T were calculated from T_1 , T_2 and T_3 using Eq. (4.1) and Eq. (4.2) with a similar method that has been discussed in section 4.1.2. The average liquid temperature \bar{T}_l was obtained by taking the mean value of T_4 , T_5 and T_6 . This data set was counted as data for passive case with wall temperature T .

Once the data for passive case was recorded and the system was thermally stable at target wall temperature T , the electro-magnet was then powered by a periodic power signal (see Figure 5.2). The signal supplied to the electromagnet was a sinusoidal wave and the signal strength was varied from 4V to 24V peak-to-peak by the power amplifier. This varied magnetic field as well as the static field from the permanent magnet created a proper driving force across the strip-array, that allowed it to actuate smoothly (see details in chapter 3).

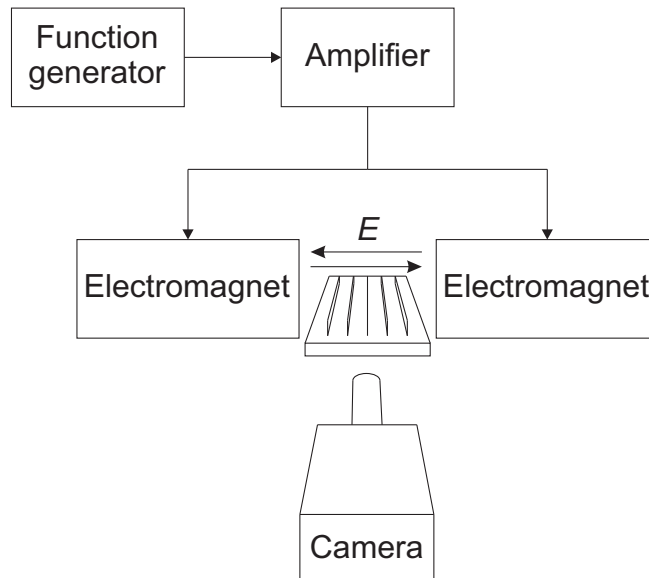


Figure 5.2: Scheme of periodic signal supplied from the electromagnet and arrangement of high speed camera.

After the strip-array was actuated at frequency f , the wall temperature temporarily reduced due to the cooler liquid being push against the surface. The heater controller started its process to supply more power to the system, so that it would be stable at the target wall temperature T again. As a result, the average liquid temperature rised up to the new stable state. The system was now stable at the same wall temperature, but at different level of power input, or in this case, a new heat flux value through the surface. This set of q and \bar{T}_l was recorded as a new data

set for active case with corresponding actuated frequency f and wall temperature T .

The other experiment data was collected with the same procedure for different value of actuated frequency f and wall temperature T . As a side note, the amplitude of the actuation was kept constant by controlling the signal strength applied to the electro-magnet from the amplifier. The uncertainty of the experiment was obtained by replicating the experiment five times for each data point. The phenomenon was visually recorded by a high-speed camera (Photron SA5) during the experiment.

5.2 Experimental substrate and actuation scheme

The test substrate used in this experiment is a silicon substrate fabricated with an array of five Nickel strips, which is able to rotate back and forth around their joints placed on substrate surface (see detail in section 3.4.2). The strip thickness is $200\ \mu\text{m}$ and its planar dimension is $1.5 \times 7\ \text{mm}$. Five parallel strips are distributed evenly throughout the heating area ($10 \times 10\ \text{mm}$), so the spacing between them is $1.6\ \text{mm}$ (Figure 5.3). The silicon substrate has a thickness of $500\ \mu\text{m}$.

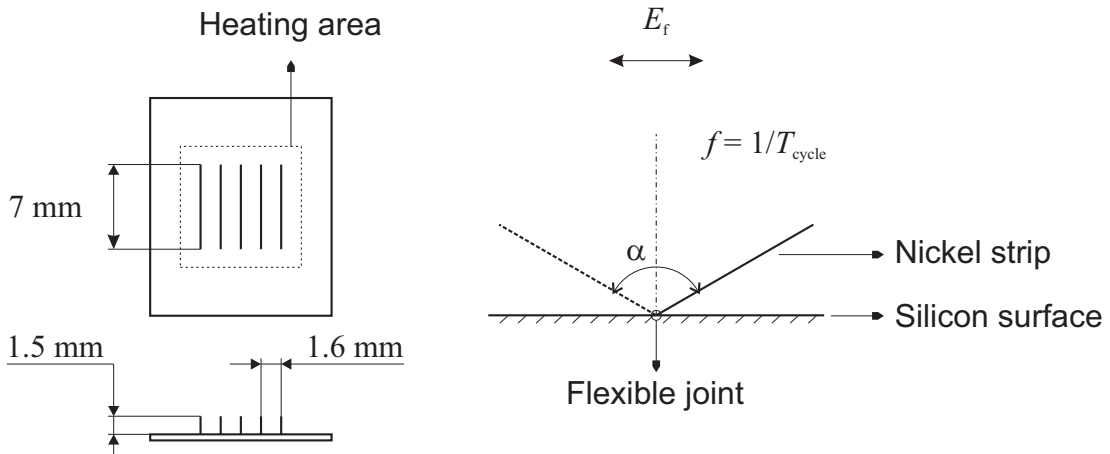


Figure 5.3: Substrate with array of Nickel strips and characteristic parameters.

When the strip-array was put under a magnetic field, it would align itself to the field direction, note that each strip has only one degree of freedom to rotate around its joint. Therefore, the periodic magnetic field E_f make it possible for each strip to rotate back and forth. The angular amplitude α and the responding

frequency f is used to characterize the movement of this strip-array (Figure 5.3). Angular amplitude is defined as the maximum opening angle that the strip can move from left to right and responding frequency is the actuated frequency that the strip responds to the external periodic magnetic field.

The actuated frequency f could be adjusted by setting the frequency of the output signal from the function generator, whereas the angular amplitude α was directly related to the signal strength, which could be regulated by the amplifier. It is worth mentioning that the actuation faces an increasing resistant force inside the liquid body along with increasing f or α . Therefore, both frequency and amplitude have their upper limit, beyond that, their value would reduce very fast to almost zero. The substrate in this experiment has been tested with various value of signal frequency and strength to get the optimize actuated mode as in table 5.1. In this mode, we regulated both signal frequency and strength to have an increasing value of actuated frequency while keeping the amplitude as a constant.

Table 5.1: Actuated mode used in the experiment, the angular amplitude is kept almost constant with varied frequency.

Actuated frequency f (Hz)	Angular amplitude α (radian)	Angular amplitude α (degree)
Passive	0	0
5	1.23	70.7
10	1.22	70.3
15	1.23	70.5
20	1.23	70.5
25	1.24	70.9
30	1.24	70.8
35	1.23	70.3

5.3 Results and discussion

5.3.1 Experimental result

The experiment has been conducted following the procedure described in the previous section. The visual results are shown in Figure 5.4 for $T = 30\text{ }^{\circ}\text{C}$ and $55\text{ }^{\circ}\text{C}$ at two different actuated frequencies ($f=5\text{ Hz}$ and 35 Hz). The visual “heat wave” pattern caused by the difference in refractive index between parts of liquid body due to temperature gradient can be observed in both case of wall temperature.

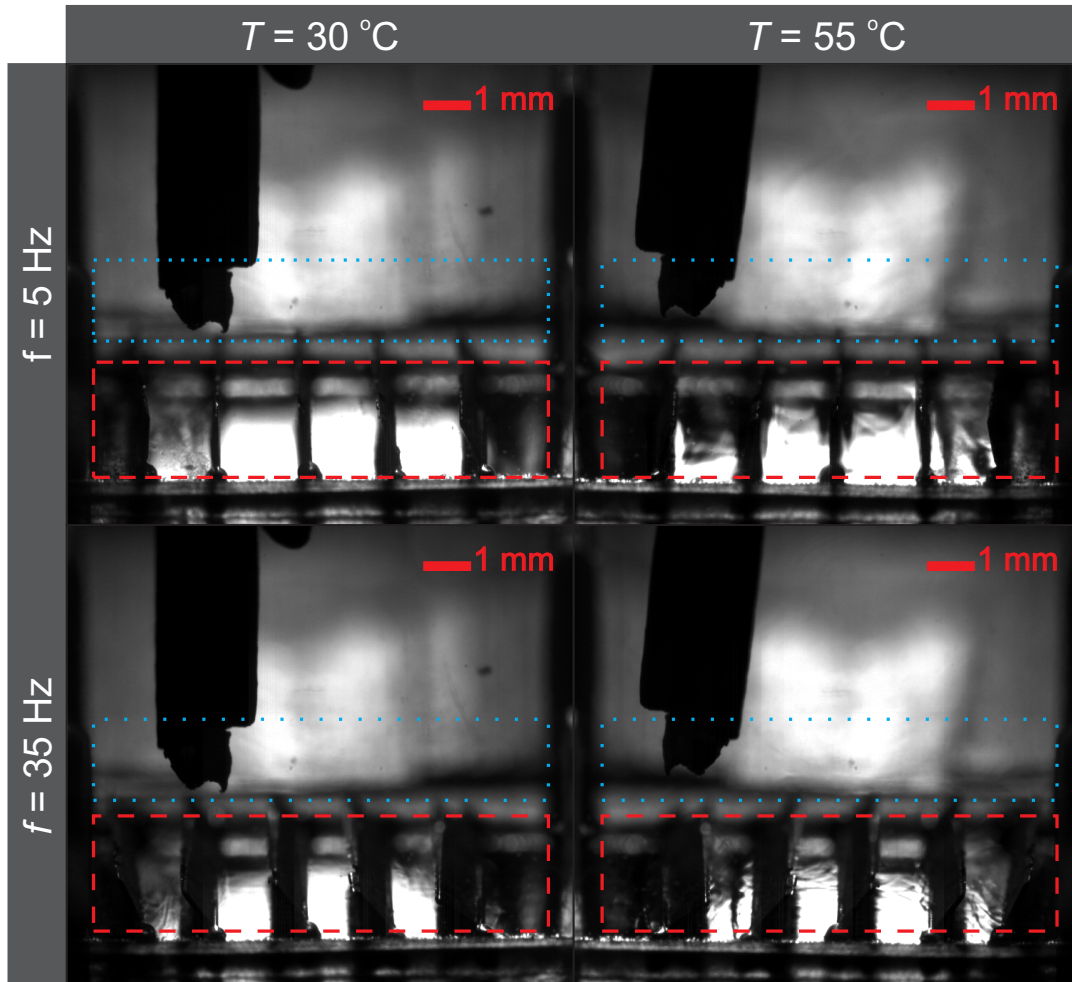


Figure 5.4: Experimental observation of different cases of wall temperature and actuated frequency. The red dash line represents the area in which internal flow created by the actuation and the blue dot line is the area on top of the array, where the net liquid volume transfers in/out the hot surface area.

There is no doubt to observe that the pattern in the images for $T = 55\text{ }^{\circ}\text{C}$ is obviously more visible than that of $T = 30\text{ }^{\circ}\text{C}$ due to higher temperature gradient between the heated surface and bulk liquid. Now if we take a closer look into the case which has the same wall temperature but different actuated frequency f : there is also a difference in the density of these patterns. In other words, the actuated strip-array did contribute to the distribution of temperature inside the liquid body.

Moreover, the pattern in the image for $f = 35\text{ Hz}$ shows that there are two main effected areas, one is the area between the strips, which stands for the “internal flow” close to the heat surface and the other area is the space upon the tip of the strips, which is represented for the “external flow” going out for the heated surface. Based on these observations, we propose that the actuation has some effects on the natural convection flow inside the liquid body by induce the net mass flow in/out from the space confined below the strip height.

Following that hypothesis, we investigate the heat flux for each experiment case. Heat flux q is calculated for each actuated frequency f and wall temperature T as shown in Figure 5.5.

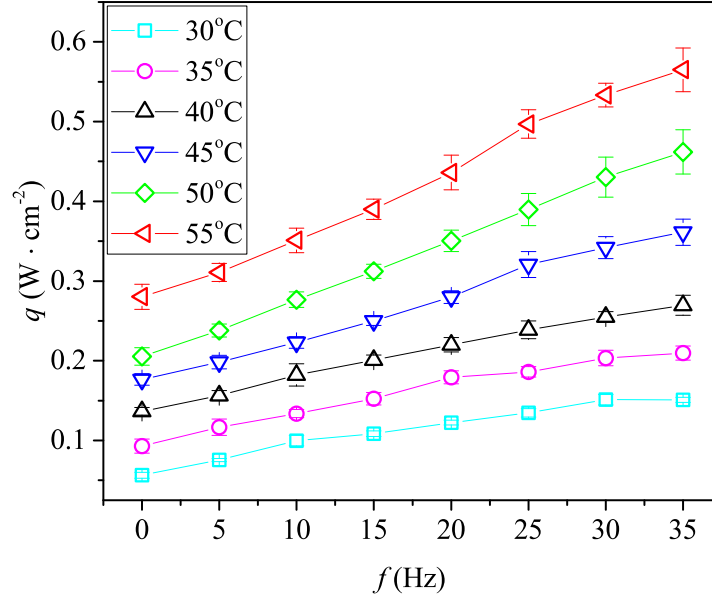


Figure 5.5: Heat flux q in relation with actuated frequency f and wall temperature T .

The horizontal axis represents the actuated frequency f and the vertical axis is the heat flux q through the substrate surface. The data is plotted for various values of wall temperature from near room temperature (30 °C) to near boiling point of FC-72 (55 °C). The actuated frequency is increasing from 0 Hz (passive) to 35 Hz with the increment step of 5 Hz. At the same value of actuated frequency, heat flux has the trend to increase along with increasing wall temperature. That can be expected since hotter surface creates larger temperature gradient and promotes more convection inside the liquid body. Interestingly, the actuation seems to amplify this effect over the hotter surface. For instance, when f varies from 0 Hz to 35 Hz, heat flux increases $\Delta q \simeq 0.1 \text{ W/cm}^2$ at $T = 30 \text{ °C}$ whereas it increases a notable larger amount $\Delta q \simeq 0.3 \text{ W/cm}^2$ at $T = 55 \text{ °C}$, which is three times larger. Moreover, this heat flux enhancement also shows a monotonical relation with increasing f , which motivates an assumption that there is a cumulative effect of natural convection and additional convection due to mass transfer caused by the actuation.

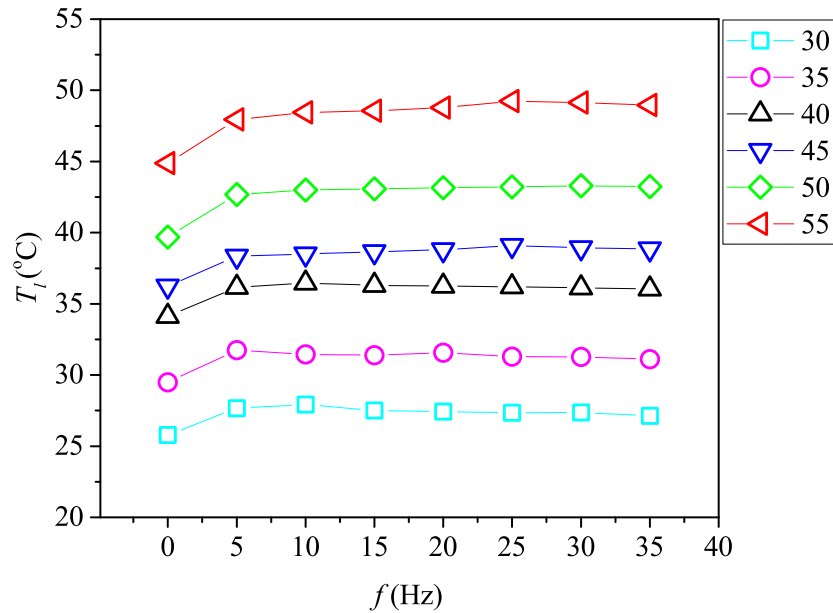


Figure 5.6: Relation between liquid temperature T_l and actuated frequency f .

Now, that assumption motivates us to consider the bulk liquid temperature in relation with actuated frequency f . We recall the hypothesis that the overall

convective heat transfer is improved due to enhanced mass transfer, and therefore, the temperature gradient inside the bulk liquid has to be reduced. In the other words, the average temperature of liquid body T_l is increased to keep up with the temperature of the hot surface. In fact, that trend is shown in the experiment as in Figure 5.6.

The results exhibit an obvious jump of \bar{T}_l between the passive and active case. However, for same value of wall temperature T , the liquid temperature \bar{T}_l is not much different with increasing f . This may be explained by the asymmetric movement of the strip-array, which also creates an “internal flow” as described in the previous observation. This flow may limit the mass transfer process to an upper bound, which related to the properties of the actuators in term of “effective mass” transferred per cycle. This term will be discussed in the next section.

5.3.2 Proposed model for convective heat transfer on actuated structure

Base on the observation and experiment results, we propose a model for the convective heat transfer on this actuated structure. We assume that the increasing amount of heat flux $\Delta q = q_f - q_o$ under frequency f is a result of enhanced mass transfer across the liquid medium. An extra mass rate \dot{m} is being pushed though the heat transfer area and takes away an amount of energy from the surface to the liquid body, causing average temperature of the bulk liquid \bar{T}_l to increase.

By that assumption, we consider a control volume as in Figure 5.7. This control volume is defined using experimental method, as a volume from the heat surface to a liquid level that has significantly higher temperature gradient than the upper rest of bulk liquid. In this case, the control volume is defined as a volume of $10 \times 10 \times 13$ mm³ bulk liquid above the heat surface. Base on the experimental observation, once the strip array is actuated with frequency f , the system becomes steady state after a short time (around 2-5 minutes). This actuation also creates a steady state flow inside the bulk liquid, where a mass flow rate \dot{m} is carried in and out from the control volume equally. Once we increase the actuated frequency f , the exchanged mass flow rate \dot{m} should also be increased across the control volume. Now if the substrate is not heated, this \dot{m} carried no heat energy with it and the heat transfer

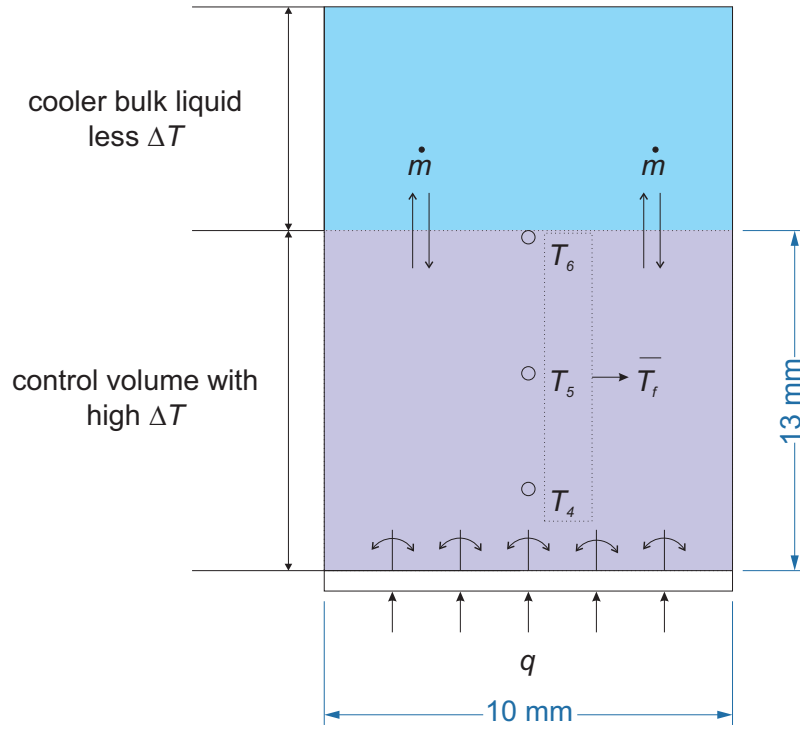


Figure 5.7: Control volume for heat transfer across the bulk liquid.

process will not happen. However, once the substrate is heated, \dot{m} starts its role as a heat energy exchanger: transferring the heat energy it received from the control volume to the upper cooler bulk liquid, then going back to the control volume again. Since \dot{m} can be enhanced by increasing f , the heat transferring process can also be improved as a result. We now consider the improvement of exchanged heat energy caused by the strips actuation in compare with passive case. In other words, this can be described as the different in the heat energy, or different in enthalpy of the system, which is written in form of specific heat C_p , \dot{m} and bulk liquid temperature different as in the right term of Eq. (5.1). On the other hand, this enhancement can also be described as the difference between heat flux supplied to the system in passive and active case.

Therefore, it follows the equation:

$$A(q_f - q_o) = \dot{m}C_p(\bar{T}_{l,f} - \bar{T}_{l,o}). \quad (5.1)$$

where q_f and q_o are the heat fluxes through substrate surface while the strip-array actuate with frequency f and at passive state, respectively; A is the projected heat

transfer area ($10 \times 10 \text{ mm}^2$); C_p is the specific heat of FC-72; $\bar{T}_{l,f}$ and $\bar{T}_{l,o}$ are the average liquid temperatures across described control volume with and without actuation respectively.

The extra mass transfer \dot{m} can be evaluated by relating the properties of the actuator in terms of geometry and movement mode:

$$\dot{m} = n\xi\rho V_c f. \quad (5.2)$$

where $n = 5$ is the number of strips in the array; ρ is the density of working liquid FC-72; f is the actuated frequency of the actuator; V_c is the total space (volume) that one strip sweeps through in one cycle and ξ is a coefficient that accounts for the effective (real) mass transfer in/out of the heat transfers zone.

The total space that one strip sweeps through in one cycle, V_c , can be calculated from the strip topology (strip height R , strip length L) and its movement mode (angular amplitude α):

$$V_c = \frac{1}{2}R^2\alpha L \times 2. \quad (5.3)$$

The coefficient ξ is defined as the ratio between V_c and the net liquid volume, V_e , that has been pushed against the hot surface in one cycle, $\xi = V_e/V_c$. Since V_e is represented for the ability of the strip to create whether a strong or weak net flow inside the liquid, the coefficient ξ is directly related to the properties of the actuator such as shape, stiffness, surface roughness and even surface wettability.

Finally, the extra mass transfer rate \dot{m} can be rewritten as:

$$\dot{m} = kf. \quad (5.4)$$

where $k = n\xi\rho R^2\alpha L$.

Substituting \dot{m} into Eq. (5.1), we have:

$$A(q_f - q_o) = kC_p f (\bar{T}_{l,f} - \bar{T}_{l,o}). \quad (5.5)$$

or

$$\frac{A(q_f - q_o)}{\bar{T}_{l,f} - \bar{T}_{l,o}} = kC_p f. \quad (5.6)$$

From Eq. (5.6), the term on the left-hand side represents the heat transfer enhancement obtained from measured heat flux and liquid temperature whereas the term on the right is that improvement calculated from extra mass transfer caused by the actuators, which is characterised by the coefficient ξ . It is shown in Figure 5.8 that the experiment data collapse into a linear line, which strengthens our hypothesis. Moreover, the slope of this collapsed data line can be used to calculate k , which is then used to estimate the value of coefficient ξ for our actuated substrate. Besides the traditional method to estimate the flow field inside the liquid such as PIV measurement, this can be used as a simple method to evaluate the ability of an actuator in terms of both heat and mass transfer.

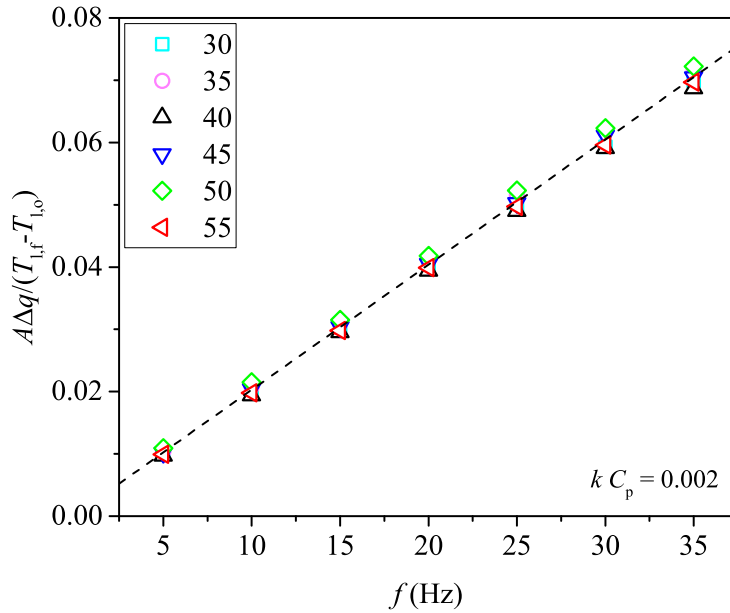


Figure 5.8: Data collapses and shows the relation between the enhanced thermal properties of the system and the improved mass transfer rate.

5.3.3 Non-dimensional relationship of heat transfer process and actuation of strips array.

To further understand the dependence of the heat flux q on the actuation frequency f and the wall temperature T , or equivalently the temperature difference $\Delta T = T - T_l$, we examine the non-dimensional relationship $\text{Nu} = \mathcal{F}(\text{Re}, \text{Gr}, \text{Pr})$, where $\text{Nu} = qL/(\Delta T k)$ is the Nusselt number (non-dimensional heat flux), $\text{Gr} = g\beta\Delta TL^3/\nu^2$ the Grashoff number (non-dimensional buoyancy), $\text{Pr} = \nu\rho C_p/k$ the Prandtl number, and $\text{Re} = fL^2/\nu$ the Reynolds number (non-dimensional inertia). Here $L = 1.5\text{mm}$ denotes the height of the fin, g is the gravitational acceleration, k is the thermal conductivity of the liquid, ν the kinematic viscosity, β the coefficient of expansion, C_p the specific heat, and ρ the density. Since Pr is constant in our experiments, we focus on the effect of Gr and Re on Nu .

In the absence of any actuation, i.e. $f = \text{Re} = 0$, the Nusselt number scales as $\text{Nu} \sim \text{Gr}^{0.63}$ (Figure 5.9). This scaling is consistent with past measurements [149], where a correlation of the form $\text{Nu} \sim \text{Ra}^{0.57}$ was observed for natural convection over fins. Here, similar to the Grashoff number Gr , the Rayleigh number Ra is also proportional to ΔT .

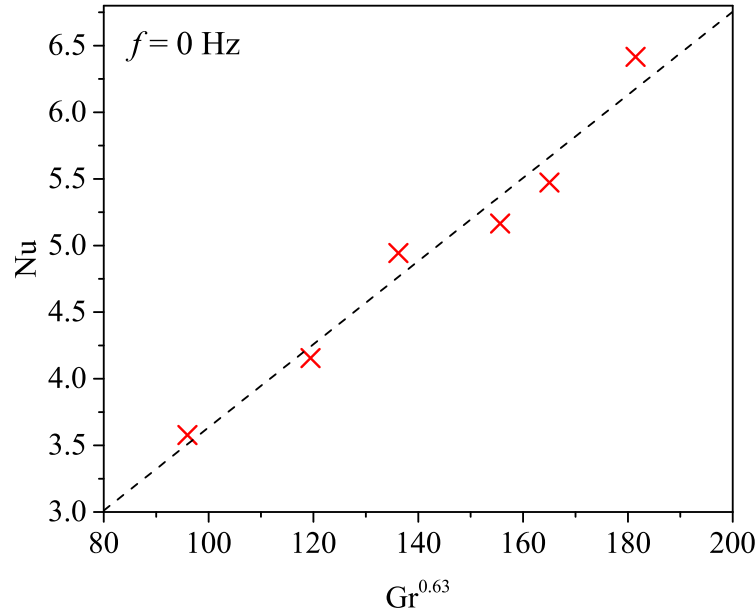


Figure 5.9: Relation between Nu and Gr in the passive case.

At very high values of f , we expect Nu to be determined mostly by Re . In such a situation, the convective velocity of the fluid scales like $U \sim fL$. For FC-72, $Pr \gg 1$, indicating that in the presence of forced convection, the thickness δ_T of the thermal boundary layer is less than the thickness δ of the velocity boundary layer at the wall. In such cases, it can be readily shown [150] that $\delta_T/L \propto Re^{-1/2}Pr^{-1/3}$. The net heat flux is then given as $q \sim k(T - T_l)/\delta_T = k((T - T_l)/L)Re^{1/2}Pr^{1/3}$, indicating that Nu scales as $Nu = qL/(k\Delta T) \sim Re^{1/2}Pr^{1/3}$. In Figure 5.10, we note that Nu indeed appears to vary approximately linearly with $Re^{1/2}$, although there is also significant scatter in the data at higher values of f .

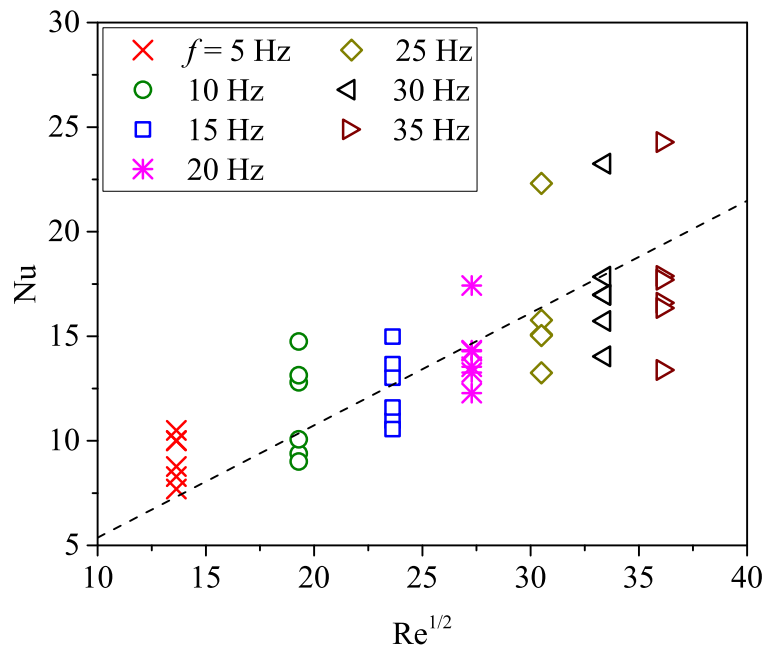


Figure 5.10: Relation between Nu and $Re^{1/2}$ for different non-zero actuation frequencies f . The dashed line indicates the scaling $Nu \sim Re^{1/2}$.

It was shown [151] using dimensional analysis and conservation laws, i.e. mass, momentum and energy conservations, that the Nusselt number should follow the scaling $Nu \sim Re^{1/2}\mathcal{G}(Gr^{1/4}/Re^{1/2})$ for combined forced and natural convection, with \mathcal{G} asymptotically tending to a constant for $Gr^{1/4}/Re^{1/2} \rightarrow 0$. Our data show that the value of $Nu/Re^{1/2}$ approaches a constant for small values of $Gr^{1/4}/Re^{1/2}$, while it has a tendency to increase at higher $Gr^{1/4}/Re^{1/2}$ (Figure 5.11a).

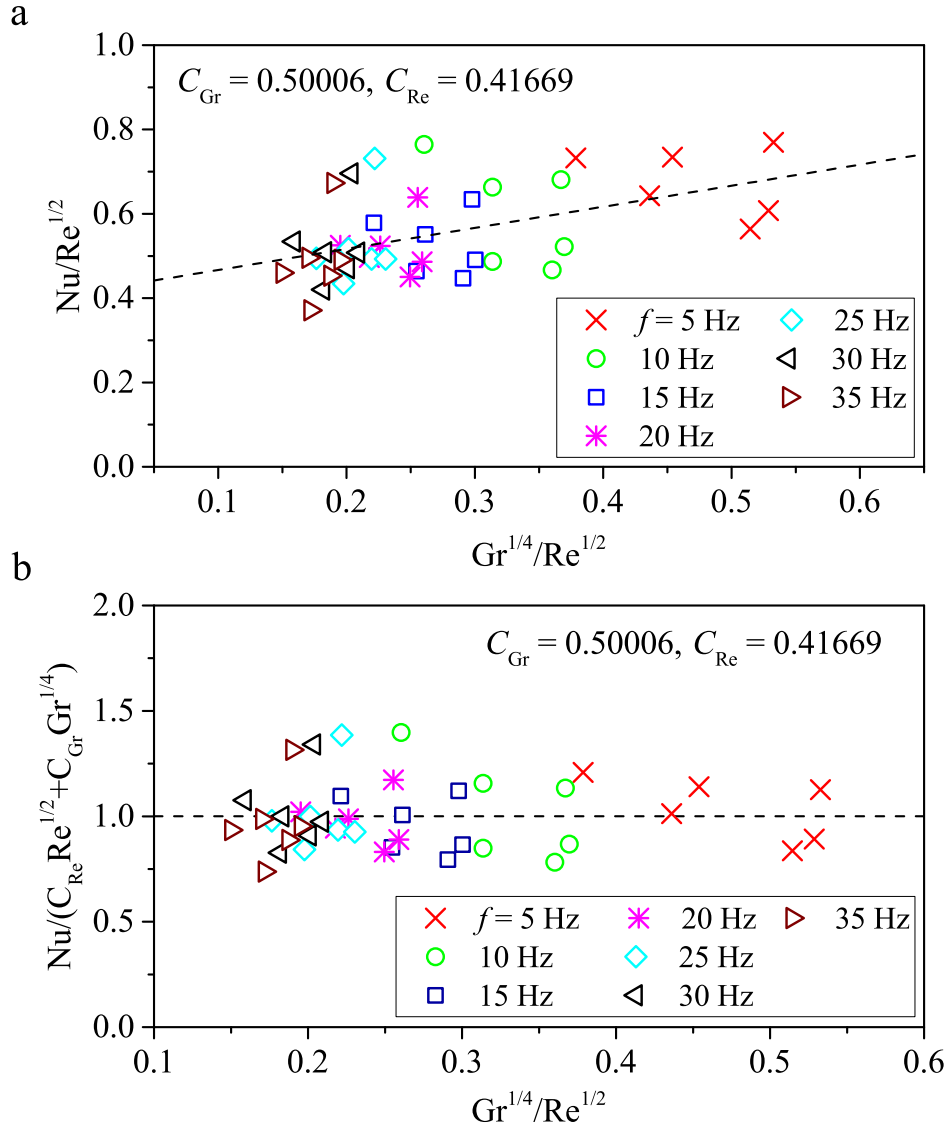


Figure 5.11: (a) Relation between $Nu/Re^{1/2}$ and $Gr^{1/4}/Re^{1/2}$. The dashed line indicates $C_{Re} + C_{Gr}Gr^{1/4}/Re^{1/2}$, where C_{Re} and C_{Gr} are obtained via a least squares fit of the data; (b) $Nu/(C_{Re}Re^{1/2} + C_{Gr}Gr^{1/4})$ vs $Gr^{1/4}/Re^{1/2}$.

Interestingly, such a trend in $\mathcal{G}(\text{Gr}^{1/4}/\text{Re}^{1/2})$ was also observed for forced convection on a heated vertically oriented plate undergoing periodic longitudinal oscillations [152], whereby Re was determined based on the frequency of the plate oscillation. A linear least squares fit of the data from our experiments yields the relationship $\text{Nu} = C_{\text{Re}}\text{Re}^{1/2} + C_{\text{Gr}}\text{Gr}^{1/4}$, in which $C_{\text{Re}} = 0.42$ and $C_{\text{Gr}} = 0.50$ (Figure 5.11b) with the coefficient of determination $R^2 = 0.2$. We refrain from speculating on the dependence of \mathcal{G} on Pr since the experiment was performed using only one liquid.

5.4 Summary

In summary, we have experimentally demonstrated a novel and robust method for enhancing heat transfer on a substrate using electromagnetic-induced actuation of nickel strips attached to the boiling substrate. We achieved localised heat transfer enhancement up to 100% using single-phase liquid cooling. For any given wall temperature T , the bulk temperature does not change significantly with actuation frequency, indicating that any enhancement in heat flux results from a systematic reduction of the thermal boundary layer thickness in the presence of actuation. In general, it appears that for active fins, the thermal boundary layer thickness is governed by the convective fluid velocity induced by the oscillating fins. The results from this work show that increasing the characteristic velocity scale of the fluid flow using electromagnetically actuated structures can be used to significantly enhance the rate of heat transfer from heated substrates. Our analysis also provides a guideline on how the heat transfer enhancement relates to the physical and geometric parameters of the system.

Chapter 6

Experimental study of bubble nucleation on a microheater

In the previous chapters, we have discussed about experimental results on passive nanopillar structure, which exhibited a remarkable role of rewetting at the three-phase contact line (TCL). The proposed model used the rewetting scheme of a vapour bubble on substrate surface, which showed a good prediction for critical heat flux and wall superheat. In this chapter, we would like to focus on the nucleation of one individual bubble and the interaction between an actuated strip and bubble nucleation.

In detail, this experiment focuses on the relation between the dynamic behaviour of bubbles, bubble departure frequency, the temperature at the nucleation site of a heated substrate during a nucleate boiling process with or without the present of an actuated strip. The bubble behaviours during the growth process from a controlled cavity were observed using a high-speed camera system. Together with these observations, synchronous measurements of the temperature underneath the bubble were measured by a microsensor.

6.1 Hydrodynamic behaviour of a single bubble nucleated on a microheater

6.1.1 Experimental setup and procedures

The first design of boiling rig for passive pool boiling was used in this experiment (see Figure 6.1a). The working liquid (degassed ethanol) was contained in a test section, which was a quartz cuvette of dimensions $10\text{ mm} \times 10\text{ mm} \times 30\text{ mm}$. The cuvette was placed inside a chamber to prevent any temperature fluctuation caused by the surrounding air. The chamber was made of stainless steel and had two glass windows to facilitate optical visualisation of vapour bubbles inside the test section. The volume of the chamber was $25 \times 25 \times 25\text{ mm}^3$. The base of the chamber can be heated by a copper block embedded with a cartridge heater. The top of the cuvette was connected to a cooling chamber used to condense vapour and circulate the liquid back to the cuvette. The pressure of the cooling chamber was monitored by a pressure transducer and was kept at atmospheric pressure by adjusting the power of a Peltier unit attached to the cooling chamber.

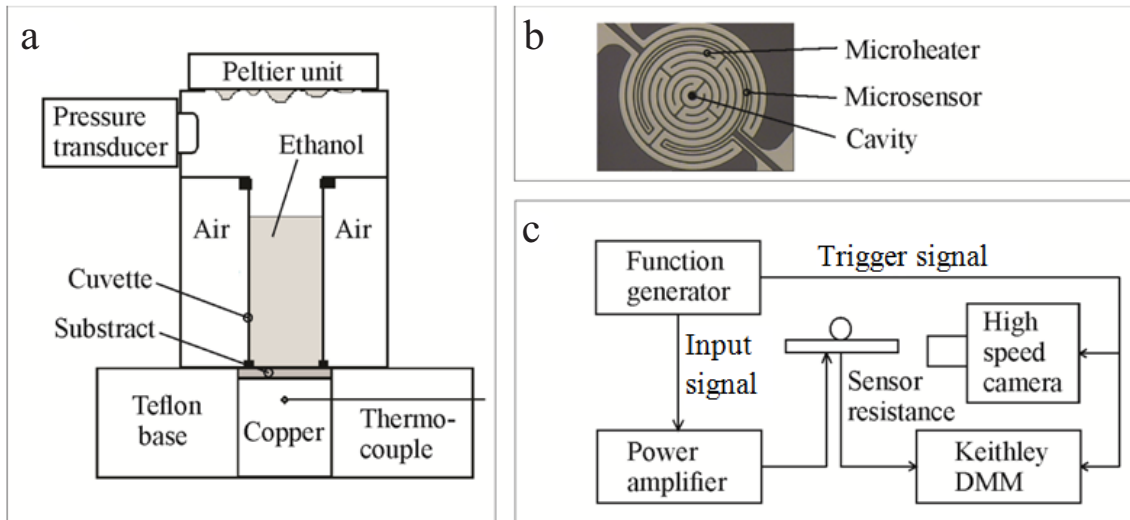


Figure 6.1: (a) The schematic drawing of boiling rig used in the experiment (b) SEM image of the microheater/sensor fabricated on top of the substrate. There is a cavity ($40\text{ }\mu\text{m}$ in diameter and $150\text{ }\mu\text{m}$ in depth) at the centre of the microheater/sensor and (c) Synchronisation of the heating signal applied to the microheater, acquisition of temperature from the microsensor, and optical recording system.

The microsensor and microheater were fabricated on a silicon substrate of dimension $0.5 \text{ mm} \times 15 \text{ mm} \times 18 \text{ mm}$. Both the microheater and the microsensor had serpentine layouts (see Figure 6.1b) and they covered a circular area of 1 mm in diameter. The nominal resistances of the microheater and microsensor are 400Ω and 370Ω , respectively. For each sensor, we measured the temperature dependence of its resistance and used the calibrated relation to deduce the temperature of the sensor from its measured resistance. At the centre of the microheater/sensor, an artificial cavity of $40 \mu\text{m}$ in diameter and $150 \mu\text{m}$ in depth was etched to serve as a nucleation site for vapour bubbles.

The temperature of the copper block underneath the substrate was maintained at $60 \text{ }^\circ\text{C}$ by a cartridge heater, which was controlled by a PID temperature controller (E5CSV, Omron). Before activating the microheater, temperature of the working liquid at steady state was $50 \text{ }^\circ\text{C}$, which corresponds to 18 K subcooling for ethanol. This working liquid temperature was measured by an immersed thermocouple inside the bulk liquid. Subsequently, the microheater was supplied with a 1MHz AC current provided by a power amplifier. The supplied power per unit area was varied from 0.35 MW/m^2 to 2.32 MW/m^2 . For each value of applied power P , the corresponding sensor temperature was acquired by a digital multimeter (3706A, Keithley). The bubble dynamics were also synchronously recorded by a high-speed camera (APX-RS, Photron).

6.1.2 Results and discussion on nucleation of individual vapour bubble

To study the relation between the bubble dynamics and the wall temperature, different values of electrical power were applied to the microheater, which was varied from 0.35 MW/m^2 to 2.32 MW/m^2 . Subsequently, the evolution of vapour bubbles, as well as the corresponding temperature of the microsensor was recorded. A representative series of snapshots of a vapour bubble is described in Figure 6.2a, when the power per unit area P supplied to the microheater was set at 0.35 MW/m^2 . For each snapshot of a vapour bubble, the equivalent diameter D_b was calculated. In this work, D_b was defined as the diameter of the circle having the same area as the bubble.

A plot of D_b versus time t is described in Figure 6.2b for a vapour bubble starting from the time of detachment of the preceding bubble. The plot consists of a pre-nucleation stage in which no bubble was observed at the cavity and the following stage in which a bubble appeared and started growing until it detached from the substrate due to buoyancy force. In the first stage, the delay time t_d , defined as the time duration from detachment of the preceding bubble to nucleation of the current one, is 1.57 s. In the second stage, D_b , increases monotonically until it reaches its departure diameter $D_b = 0.87$ mm. This two-stage process is repeated with relatively high reproducibility.

Figure 6.2b together with Figure 6.2c shows the relation between the bubble dynamics and the temperature change. It is observed that T_w starts increasing from $T_w \simeq 67.9$ °C with a relatively high rate during the pre-nucleation stage. Note that after the detachment of the preceding bubble, it takes a certain waiting period for the building up of a thermal boundary layer, which is a necessary to activate the nucleation. Subsequently, as the bubble starts growing, T_w increases with a lower rate until it reaches the maximum value $T_w \simeq 68.2$ °C before it starts decreasing and finally stabilizes at an approximated value $T_w \simeq 68.1$ °C. The energy necessary for the bubble growth comes mostly from the heated liquid layer close to the wall [16].

The effect of the supplied power P on the bubble dynamics is discussed below. In figure 6.3, we show the relation of bubble diameter D_b and heating time t_h , which is the time elapsed from the activation of the microheater, for different values of power per unit area P . It is observed that within the same heating period ($t_h < 40$ s), the number of bubbles released from the cavity and the delay time t_d changes considerably with the power per unit area: for P increases from 0.35 MW/m² to 2.32 MW/m², the number of bubbles released increases from approximately 2 to 12.

The results in Figure 6.4 described the dependences of the bubble departure frequency f_d , departure diameter D_b and delay time t_d on the averaged substrate temperature, which is obtained by time-averaging T_w for each of the applied power. It can be seen from Figure 6.4a and Figure 6.4b that f_d increases while the t_d reduces with increasing T_w . The bubble departure frequency f_d exhibits a linear increase from 0.068 Hz to 0.32 Hz as increases from 68 °C to 81 °C. On the other hand, the delay time t_d drastically reduces from 1.57 s to 0.01 s within the same temperature

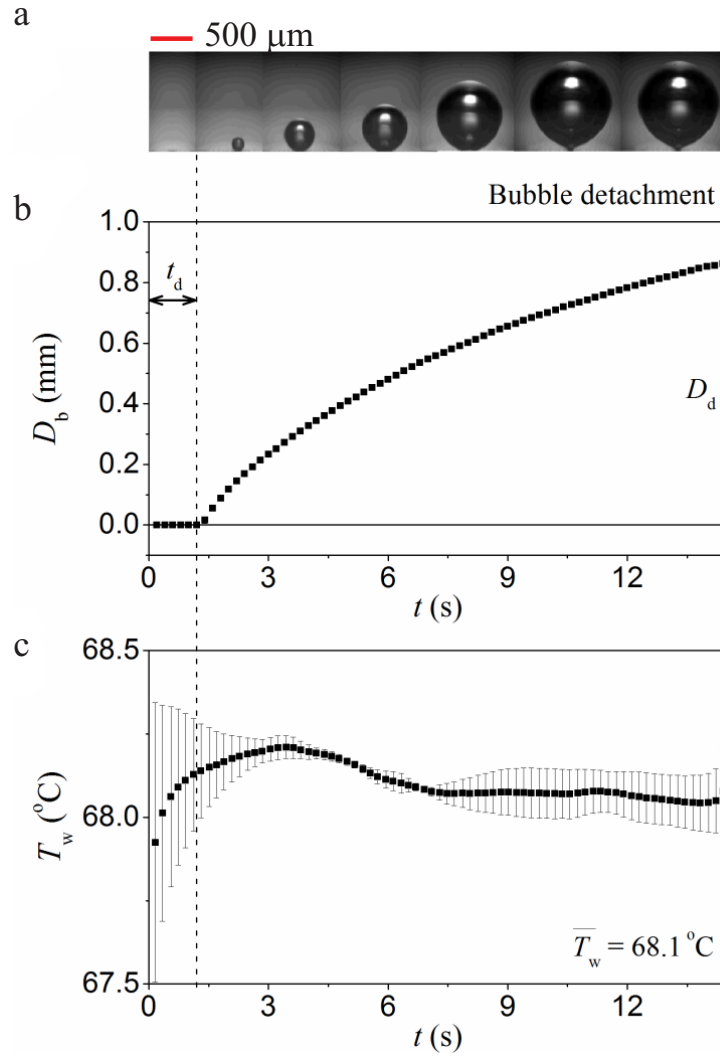


Figure 6.2: (a) Representative snapshots of a bubble nucleated when the supplied power to the heater was set at 0.35 MW/m^2 . Dependence of (b) equivalent diameter D_b of a growing bubble and (c) corresponding wall temperature T_w on time when the power supplied was set at 0.35 MW/m^2 . The average temperature of the substrate in this case is 68.1°C .

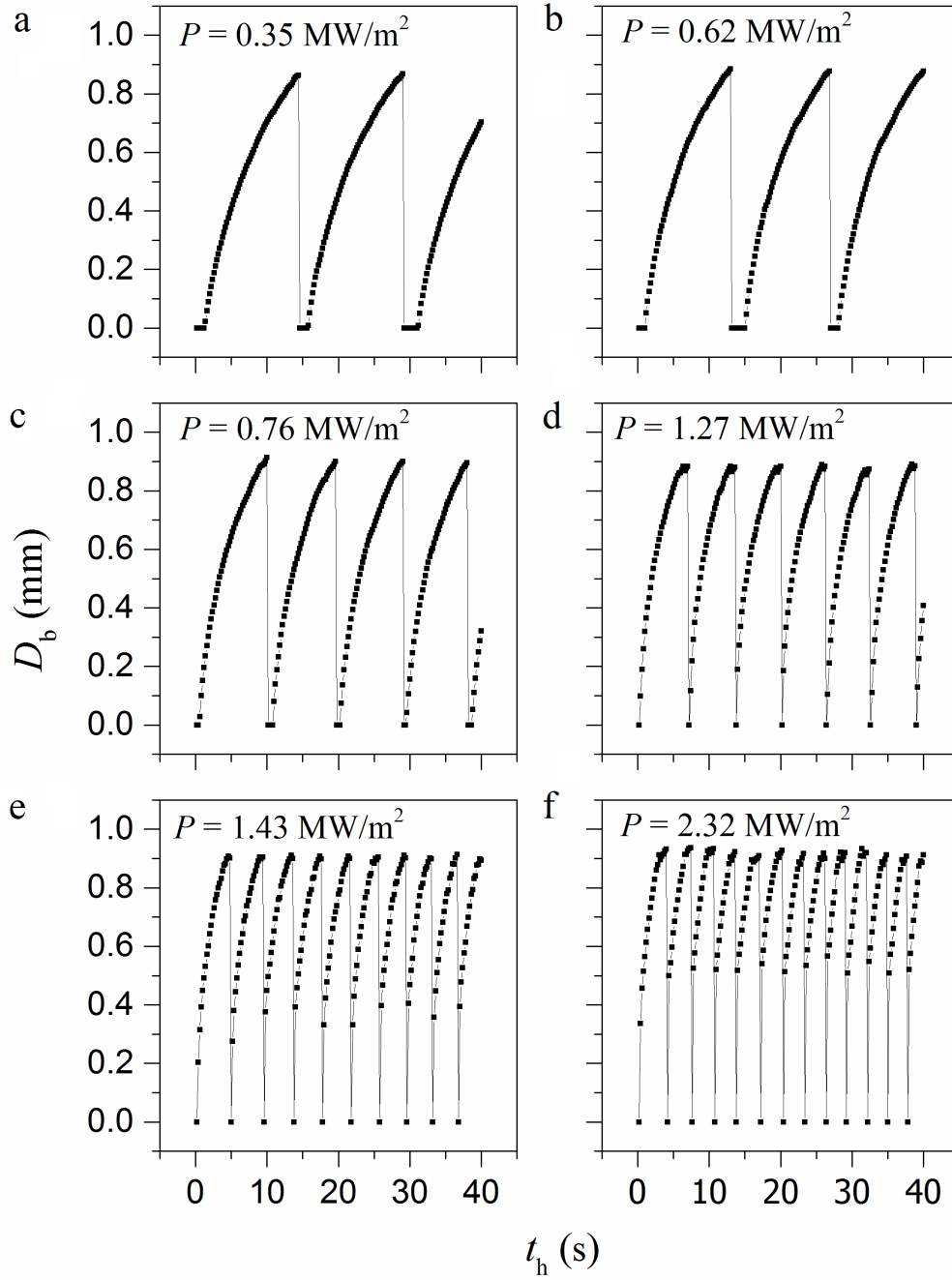


Figure 6.3: Bubble diameter D_b as a function of the heating time t_h , which is the time elapsed from the activation of the microheater, for different values of power per unit area P

range. However, it is only observed that an insignificant variation in the departure diameter: $D_d = 0.89 \pm 0.02$ mm.

It is worth mentioning that in Figure 6.4 shows that bubble nucleation takes place even at negative wall superheats ($\bar{T}_w < 78$ °C). Here the wall superheat is defined as $\Delta T = \bar{T}_w - T_s$ where $\bar{T}_w = 78$ °C is the saturation temperature of ethanol. This nontrivial phenomenon was also observed experimentally in studies of nucleate boiling of water on substrates with various wettability [1, 124] Although its physical mechanism is still unclear, attributing effects may include the substrate's wettability: the bubbles could be nucleated and grow at nominally negative wall superheats if the liquid has low wettability on the boiling substrate.

Summary

In summary, we have presented an experimental study of the dynamical behaviours of individual vapour bubbles along with measurements of the wall temperature at the nucleation site during the process of nucleate boiling. The temperature of working liquid was kept at 18 K subcooling and the boiling surface was heated by a microheater and an auxiliary cartridge heater. The experiment was conducted with the supplied power to the microheater in the range 0.35 - 2.32 MW/m². The temperature at the nucleation site was measured using an integrated microsensor. The corresponding bubble dynamics were synchronously measured using high-speed imaging.

When the applied power is 0.35 MW/m², t_d and D_b is found to be 1.57 s and 0.87 mm respectively. As P increases from 0.35 MW/m² to 2.32 MW/m², the number of bubbles released increases approximately from 2 to 12. It is found that f_d increases 0.068 Hz to 0.32 Hz and t_d reduces from 1.57 s to 0.01 s as increases from 68 °C to 81 °C. However, D_b showed an insignificant variation within the range of applied power P . It was also observed that the bubbles could be nucleated, grow, and detach even at nominally negative wall superheats.

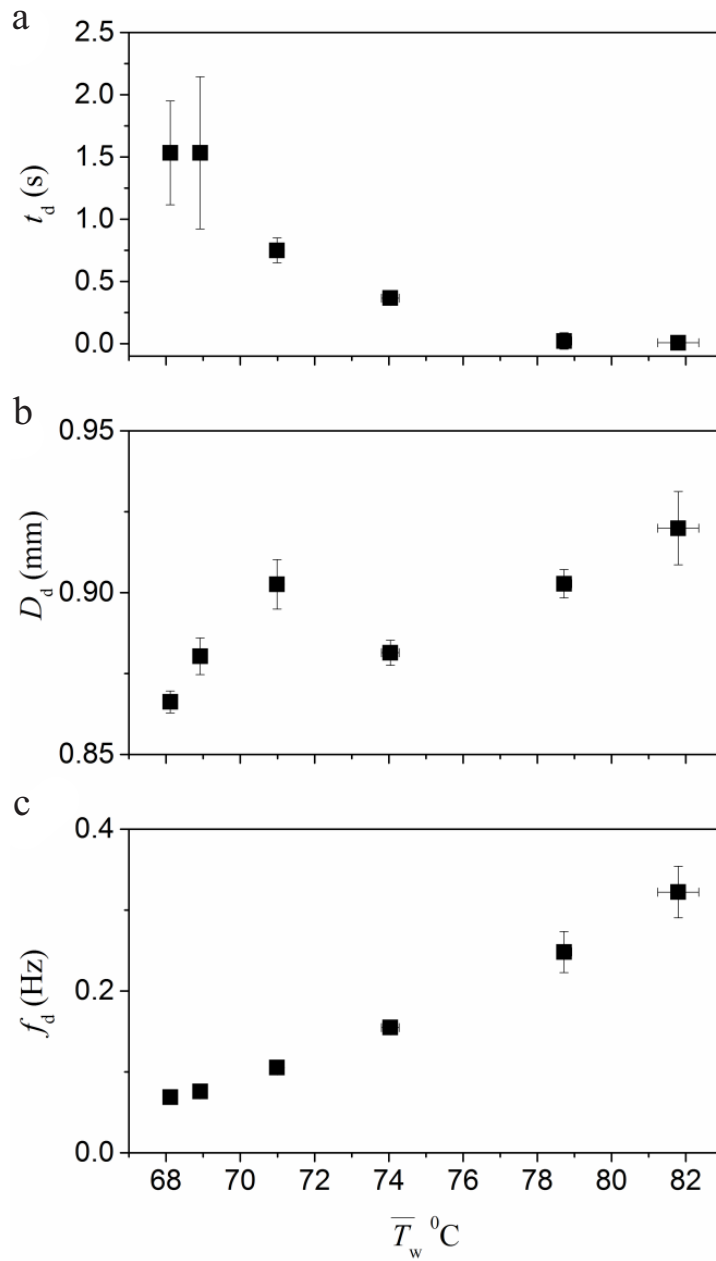


Figure 6.4: Dependence of (a) delay time t_d , (b) departure diameter D_b , and (c) departure frequency f_d , on the average temperature of the substrate.

6.2 Dynamic heat flux and wall temperature beneath a nucleate bubble

6.2.1 Experimental setup and procedures

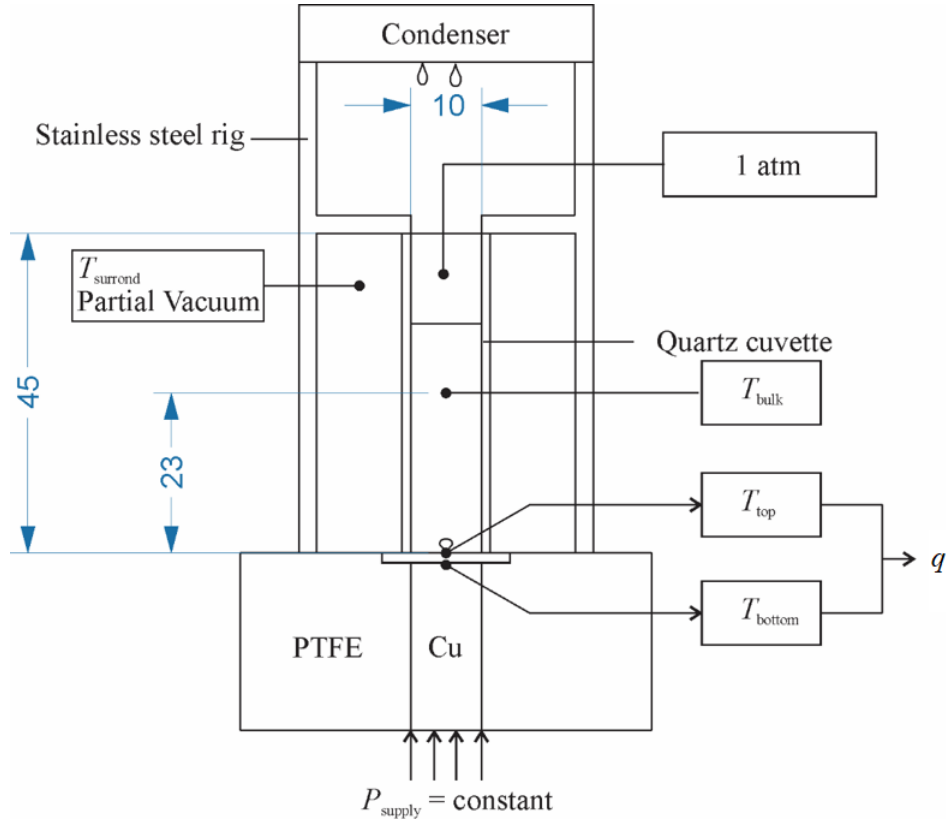


Figure 6.5: Experimental setup with two microsensors embedded on top and bottom side of the substrate, the space surrounding the cuvette is partial vacuum to ensure thermal insulation.

The experimental rig used in this experiment is similar to the previous experiment, except the substrate and heating method. Two microsensors were attached to top and bottom sides of the silicon substrate, to determine local temperature gradient across the substrate thickness. Also, a micro-cavity was fabricated at the centre of top microsensor. The substrate was heated by a copper rod, which itself received a constant power input from the cartridge heater below (Figure 6.5). The testing liquid was ethanol and subcooling was used as boiling condition. Partial vacuum

condition was maintained at the space surrounding the cuvette to limit heat loss to the cuvette side. The condenser on top of the rig help maintaining the liquid level and also the atmospheric pressure inside the chamber.

When the surface temperature reached a high enough value, the bubble nucleation was triggered at the cavity and a vapour bubble formed. The top and bottom microsensors were able to dynamically measure the local temperature change beneath the vapour bubble (Figure 6.6). The local heat flux q was calculated from temperature gradient collected from two microheaters (Eq. (6.1)). The results were described in Figure 6.7.

$$q = k_s \frac{T_{bottom} - T_{top}}{\Delta x_s}. \quad (6.1)$$

where k_s is the thermal conductivity of silicon; T_{bottom} and T_{top} are the temperature on top and bottom of the silicon substrate and Δx_s is the thickness of silicon substrate.

6.2.2 Results and discussion

i) Discussion on the thermodynamic of vapour bubble.

A snapshot of vapour bubble nucleation, growth and detachment was presented in Figure 6.6. This snapshot was taken at average surface temperature of 68.1°C. Although it was a 10 K subcooling condition for ethanol, the vapour bubble can still grow and detach from the surface due to the gas trap inside the micro-cavity. The timestamp was 1.2 s between the frame which is reasonably slow due to subcooling condition.

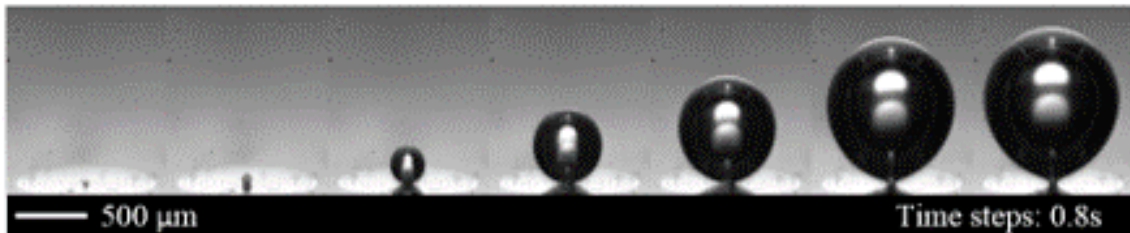


Figure 6.6: Representative snapshots of a bubble nucleated on top of the microsensor at average surface temperature of 68.1 °C.

The bubble size seems to increase rapidly at an early state from the second frame. At the ending state, this increasing trend starts to slow down and almost stop growing at the last two frames, just before the bubble detached from the surface. This observation can be verified by the measurement results of heat flux and wall temperature as in Figure 6.7.

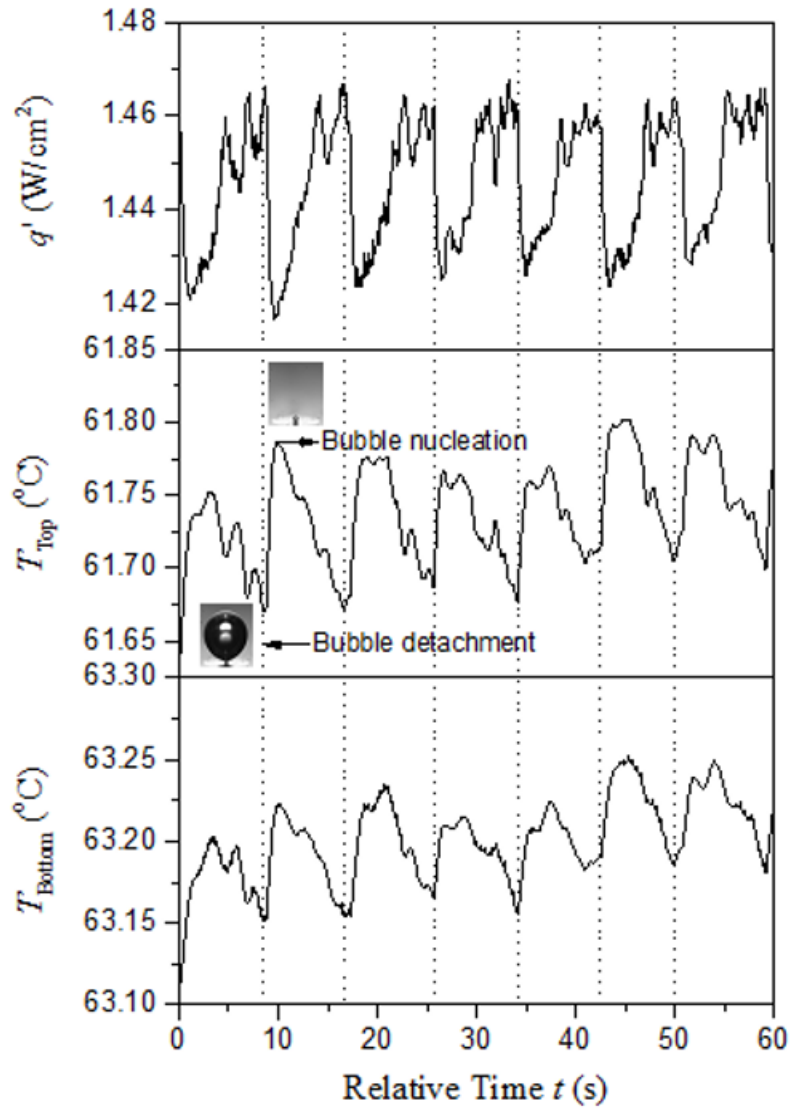


Figure 6.7: Dynamic local heat flux and wall temperature beneath a nucleate bubble at average surface temperature of 68.1°C .

The thermodynamic of a vapour bubble can be described by the local heat flux through an area of 1 mm^2 beneath the bubble. The temperatures on both side of the

substrate responded very well with the bubble growing process as they showed a synchronisation trend for every bubble cycle. A cycle of bubble growth and detachment can be classified into three states: thermal layer built-up, rapid bubble expanding due to evaporation and bubble oscillation due to balancing between evaporation and condensation.

As the previous bubble detached from the surface, the thermal layer starts to build up and the heat transfer mechanism in this period is mainly conduction through the liquid layer near the surface. That explains the reducing of heat flux q and increasing of surface temperature T_{top} .

In the next state, a new bubble will be nucleated at the cavity when the thermal boundary layer meets the critical condition. This vapour bubble rapidly increases its size due to inertia force and high rate of evaporation. The fast growing of the vapour bubble and large evaporation rate quickly dissipate heat from the surface as latent heat, causing the heat flux to increase and surface temperature to reduce.

When the bubble emerges from the thermal boundary layer, it contacts with the cooler liquid upper and the condensing process starts to speed up. The larger the bubble grows, the faster the condensing process speeds up. This process will continue until a point that they are balancing each other. The bubble will keep oscillating until the buoyancy force is large enough to make bubble detach from the surface. Therefore, the surface temperature and heat flux will also oscillate in this period, as in Figure 6.7.

ii) Discussion on dynamic bubble growth and heat flux oscillation.

We consider the growth rate of a vapour bubble nucleated from the hot surface as in Figure 6.8. In this sketch, R is the radius of curvature of the bubble surface at time t and r, θ are spherical polar co-ordinates, with origin at the centre of curvature O . The vapour pressure inside the bubble and the static pressure at a distance from the bubble is denoted as p_v and p_∞ respectively. Also, any point in the liquid with distance r from the centre of curvature O has a static pressure denoted as $p(r)$. As the bubble rises, its boundary interacts with the surrounding liquid and creates a flow field, which has the velocity potential denoted as ϕ .

As is well known [153], the motion of the liquid through a spherical shape has the velocity potential as:

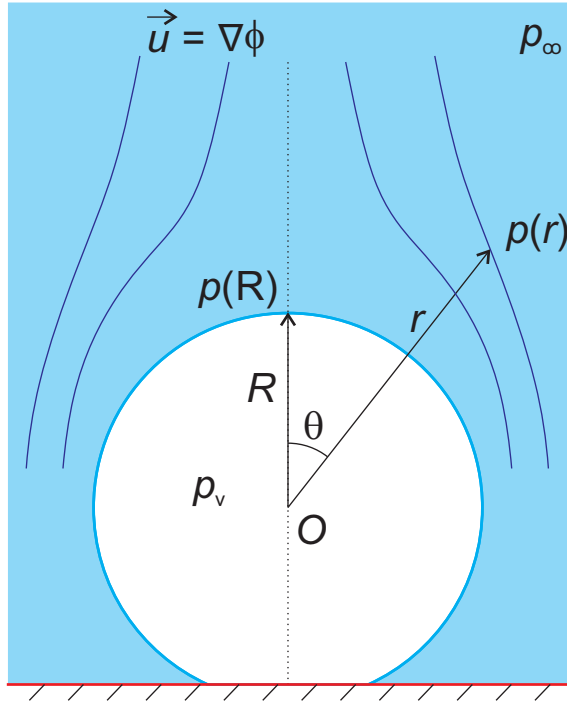


Figure 6.8: Definition sketch for a bubble rising in saturated bulk liquid, ϕ is the velocity potential of the flow surrounding the vapour bubble.

$$\phi = \frac{R^2 \dot{R}}{r}. \quad (6.2)$$

the Bernoulli integral of the above motion is:

$$-\frac{\partial \phi}{\partial t} + \frac{1}{2}(\nabla \phi)^2 + \frac{p(r)}{\rho} = \frac{p_\infty}{\rho}. \quad (6.3)$$

From Eq. (6.2), we have:

$$(\nabla \phi)^2 = \frac{R^4 \dot{R}^2}{r^4}. \quad (6.4)$$

$$\frac{\partial \phi}{\partial t} = \frac{1}{r}(2R\dot{R}^2 + R^2\ddot{R}). \quad (6.5)$$

Now if we consider Eq. (6.4) and Eq. (6.5) at position on the bubble boundary ($r=R$), we have:

$$(\nabla\phi)_{r=R}^2 = \dot{R}^2. \quad (6.6)$$

$$\frac{\partial\phi}{\partial t}_{r=R} = 2\dot{R}^2 + R\ddot{R}. \quad (6.7)$$

Substitute Eq. (6.6) and Eq. (6.7) into Eq. (6.3), we get:

$$\frac{p(R) - p_\infty}{\rho} = \frac{3}{2}\dot{R}^2 + R\ddot{R}. \quad (6.8)$$

Taking into account the relation between pressure different at the bubble boundary, surface tension and the curvature radius of the bubble, we have:

$$p(R) = p_v - 2\frac{\sigma}{R} \quad (6.9)$$

Finally, we have the relation between bubble growth rate \dot{R} and pressure different of vapour and liquid as:

$$\frac{p_v - p_\infty}{\rho} - 2\frac{\sigma}{R\rho} = \frac{3}{2}\dot{R}^2 + R\ddot{R}. \quad (6.10)$$

When the bubble has grown away from its initial radius, the surface tension and acceleration term can be neglected, Eq. (6.10) becomes:

$$\left(\frac{dR}{dt}\right)^2 = \frac{2}{3}\frac{p_v - p_\infty}{\rho}. \quad (6.11)$$

From Eq. (6.11), we found that the growth rate of bubble radius is proportional to the pressure difference $\Delta P = p_v - p_\infty$. At the beginning of the bubble growing cycle, the vapour pressure is much larger than the pressure inside the liquid (due to high evaporation rate into a small bubble size at the cavity). This causes the bubble grows rapidly until it emerged far from the thermal boundary layer. The bubble boundary contacts with the cooler bulk liquid, which promote the condensation

process. Since more and more vapour is condensed to the liquid, p_v is reduced. As a result, ΔP also reduces, causing the bubble growth rate \dot{R} to decrease. When the bubble grows bigger, the balance between p_v and p_∞ become unsteady and therefore, it causes the fluctuation in bubble radius.

Now we consider the rate of heat dQ/dt transferred through heated surface beneath the vapour bubble. By using the assumption that the rate of change in the heat content of vapour bubble is equated to heat flow in the liquid at bubble wall, Board *et. al* [154] established the relation of heat flux and bubble growth rate as in Eq. (6.12),

$$\frac{1}{4\pi R^2} \frac{dQ}{dt} = \rho_v h_{fg} \frac{dR}{dt}. \quad (6.12)$$

From Eq. (6.12), we found that the changing of heat flux over the bubble cycle is also correlated with the bubble growth rate \dot{R} . As our previous discussion, \dot{R} have the trend to increase rapidly at the early state of the bubble and then it is slow down to an unsteady state due to the pressure different between p_v and p_∞ . This explains the similar trend of heat flux found in the experiment as in Figure 6.7.

6.3 Hydrodynamic behaviour of a nucleate bubble interacted with actuated strip

In this experiment, we would like to explore the effect of an actuated strips to the bubble nucleation process. We expect the changing in bubble hydrodynamic behaviours such as bubble departure diameter or releasing frequency by regulating the actuated amplitude or frequency of the actuator.

6.3.1 Experimental setup and procedures

In this experiment, we used the boiling rig designed for active substrate as described in Chapter 3. The schematic drawing of the setup is shown in Figure 6.9a. The working liquid was FC-72 and saturated boiling was applied as the boiling condition. A pair of electromagnet was installed inside the rig, to create a periodic magnetic field across the working area. The substrate was fabricated with an actuated Nickel

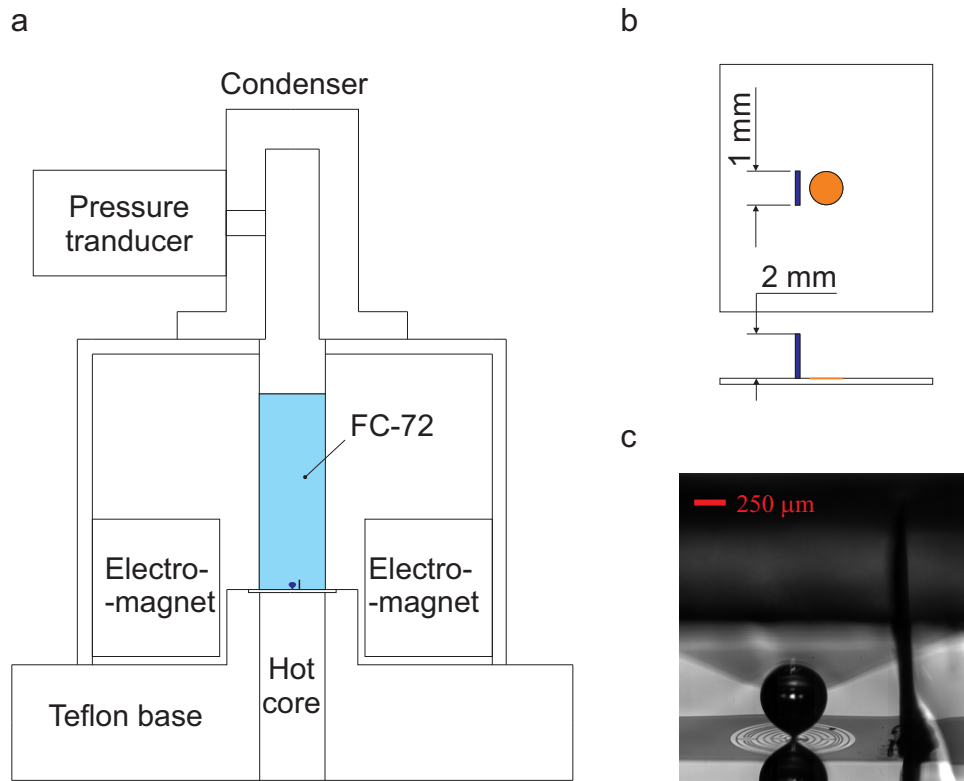


Figure 6.9: (a) Schematic drawing of the boiling rig and (b) dimension of substrate and actuators. (c) A snapshot of bubble nucleated from the cavity with the presence of the strip in passive case.

strip and was placed into the heating area above the copper rod. The fabricating method of this actuated substrate has been described in detail in chapter 3. The dimension of the actuators and substrate properties are shown in Figure 6.9b.

The substrate was fabricated with a microcavity at the centre and also integrated with a microsensor surrounding the cavity. The substrate was heated by a copper rod underneath and the surface temperature at nucleating point was measured by the integrated microsensor. A Nickel strips was placed next to the boundary of the microsensor, which is about 0.85 mm from the cavity. This strip has 2D dimensions of 1×2 mm and a thickness of $200 \mu\text{m}$. Once the electromagnet was activated, the magnetic field can drive the strip to rotate back and forth with frequency f and angular amplitude α . In this experiment, we varied the actuated frequency from 0 Hz to 60 Hz with a step of 10 Hz. Also, the angular amplitude α was set to three different values of 10, 30 and 60 degree. The interaction between vapour bubble and the actuated strip will be recorded using a high speed camera (Photron SA5) at 5000 fps.

6.3.2 Results and discussion

Discussion on experimental observations.

The interaction between a nucleated bubble at surface temperature of 56.3°C and an actuated strip ($f = 30$ Hz and $\alpha = 30$ degree) is shown in Figure 6.10.

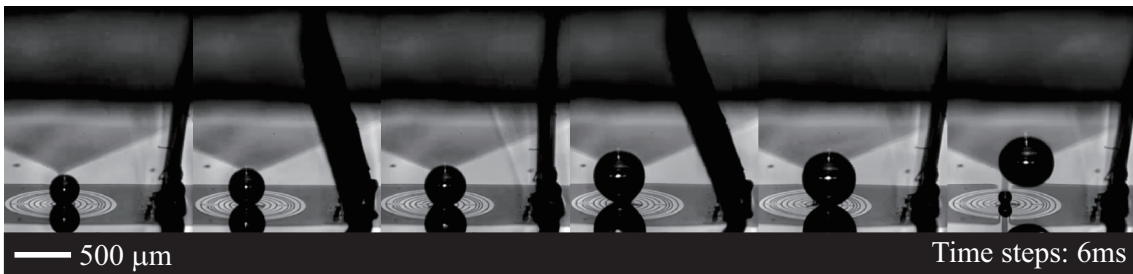


Figure 6.10: Representative snapshots of a bubble nucleated with the present of an actuated strip ($f = 30$ Hz and $\alpha = 30$ degree). The average surface temperature is close to boiling point of FC72 (56.3°C)

From the snapshot, the actuation seems to cause a strong flow rate across the bubble, causing it to oscillate around the cavity. When the bubble departed from the

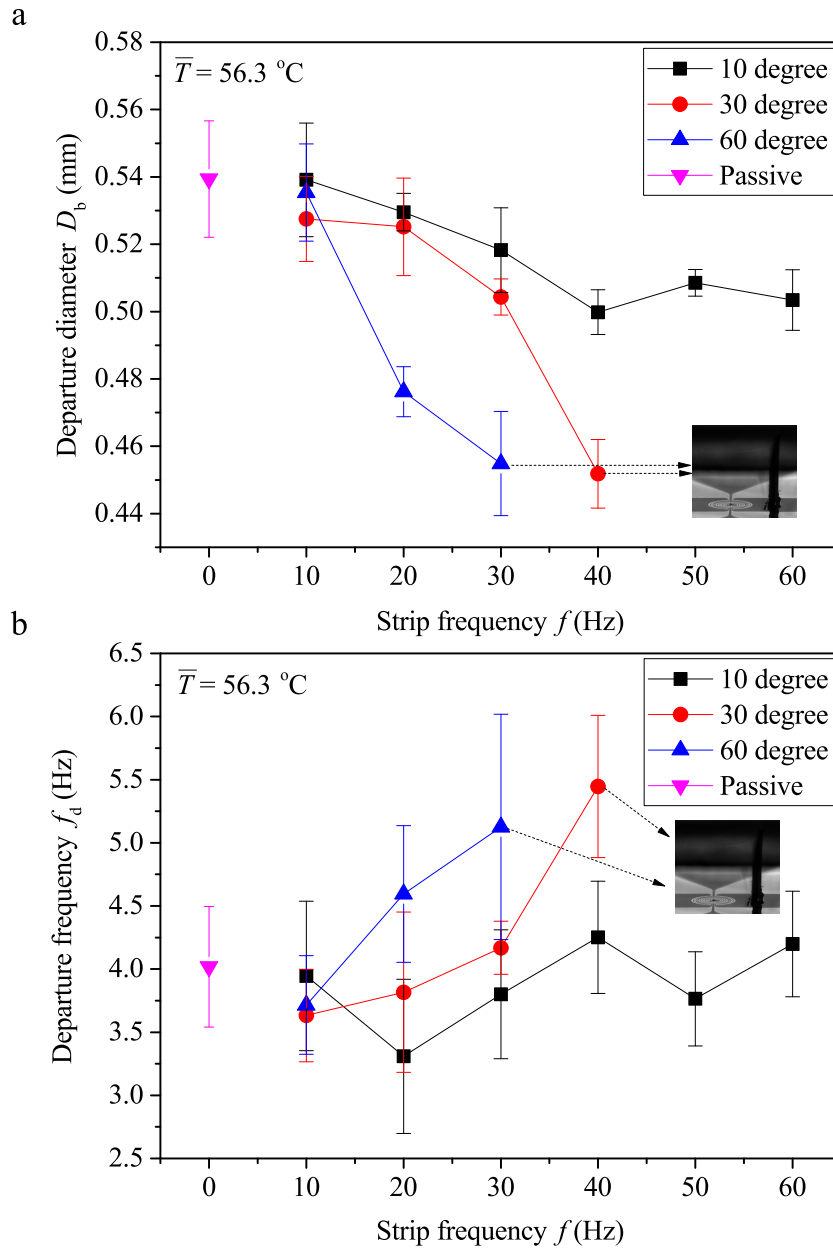


Figure 6.11: (a) Dependence of departure diameter D_b and strip frequency f for different angular amplitude. (b) Dependence of departure frequency f_d and strip frequency f for different angular amplitude.

surface, its movement path was also affected by the actuation even when the bubble did not directly contact the strip. This observation allows us to expect the changes in bubble hydrodynamic such as departure diameter or bubble releasing frequency. In fact, that assumption was shown in the measurement results in Figure 6.11.

From the results in Figure 6.11, the bubble departure diameter D_b and releasing frequency f_d have a direct relation with strip frequency f and actuated amplitude α . Along with increasing f or α , D_b decreased monotonically while the departure frequency f_d has a trend to increase. It can be explained that the extra flow rate caused by the actuation, has created an extra drag force to push the bubble away from the cavity. This force together with buoyancy force stimulated the bubble to leave the surface sooner. As a result, the bubble departure diameter D_b also reduced.

Force analysis on the vapour bubble.

To have a better understanding on the effect of actuated strips to the vapour bubble, we now consider a simple force model as in Figure 6.12. A growing bubble with radius of curvature R , is put next to an actuated strip with frequency f . In this case, we assume that the bubble has a nearly spherical shape and the distance from the spherical centre to the base is denoted as s . The strip is close to the bubble enough (~ 0.85 mm) to assume that the fluid velocity caused by the actuation is close to the fluid velocity nearby the bubble.

In such case, the forces that act on the bubble can be classified into two groups of upward and downward forces. The upward forces include buoyancy force F_b , contact pressure force F_p and drag force caused by the actuation D_{ay} . In the opposite direction, the forces that keep the bubble on the base surface are capillary force F_c and drag force caused by the relative movement between the rising bubble and upper bulk liquid F_d . The buoyancy force can be calculated as

$$F_b = (\rho_l - \rho_v)gV_b. \quad (6.13)$$

where V_b is the volume of a spherical segment, which involves only the volume of the region in contact with liquid above and below the bubble cap.

Contact pressure force caused by the pressure difference at the bubble cap interface, this force can be calculated as:

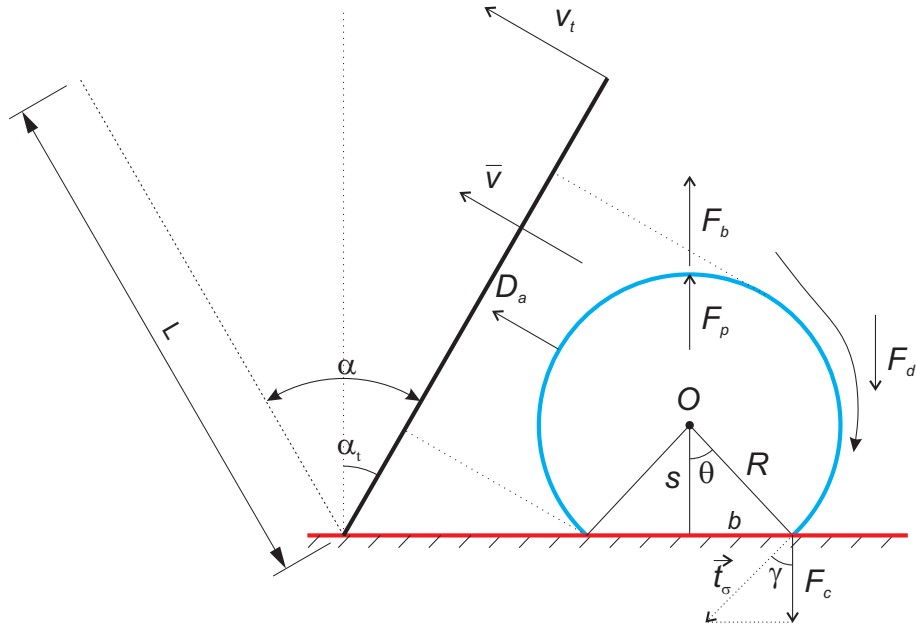


Figure 6.12: A schematic drawing of forces act on the vapour bubble with the presence of an actuated strip during its growing cycle.

$$F_p = \pi b^2(p_v - p_l). \quad (6.14)$$

where b is the bubble base radius. Applying the Young-Laplace equation at bubble interface $p_v - p_l = 2\sigma/R$, we have:

$$F_p = \frac{2\pi\sigma b^2}{R}. \quad (6.15)$$

As for the capillary force F_c caused by surface tension σ acts along the three phases contact line at the bubble base (t_o is the unit vector of F_c), we have:

$$F_c = 2\pi b\sigma \sin(\gamma) = \frac{2\pi\sigma b^2}{R}. \quad (6.16)$$

The drag force F_d is caused by the relative movement between the rising bubble and the upper liquid. It can be approximated as

$$F_d = \frac{1}{2}\rho_l C_D \pi s^2 \dot{s}^2. \quad (6.17)$$

where C_D is the drag coefficient for a spherical bubble moves in bulk liquid [155]:

$$C_D = \frac{24}{Re} \left(1 + \frac{3}{8} Re \right), Re = \frac{2R\rho_l \dot{s}}{\mu} \quad (6.18)$$

Drag force caused by the actuation.

Drag force D_a on the bubble is caused by the interaction between the bubble and the surrounding flow rate. This flow rate is a result of the strip actuation, which is assumed to have the same velocity as the actuator. In such case, the average fluid velocity at the middle of the strip that creates the drag force is as

$$\bar{v} \sim \frac{1}{2} v_t = \frac{1}{2} \omega L. \quad (6.19)$$

where ω is the angular velocity of the actuated strip and L is the strip height. The angle α_t of actuated strip at time t can be calculated as (α and α_t are in radian)

$$\alpha_t = \frac{\alpha}{2} \sin(2\pi ft). \quad (6.20)$$

where f is the actuated frequency and α is the maximum actuated angle of the strip. Therefore, ω can be defined as,

$$\omega = \frac{d\alpha_t}{dt} = \alpha f \pi \cos(2\pi ft). \quad (6.21)$$

Substitute Eq. (6.21) into Eq. (6.19), we get the average fluid velocity that caused the drag force:

$$\bar{v} = \frac{1}{2} \alpha L f \pi \cos(2\pi ft). \quad (6.22)$$

The drag force D_a can be calculated using the average fluid velocity \bar{v} as:

$$D_a = \frac{1}{2} \rho_l C_D A \bar{v}^2. \quad (6.23)$$

where A is the cross section area of the bubble segment that is effected by the drag force (area between the dot line in Figure 6.12. This area can be calculated as:

$$A = \frac{R^2}{2} (2\pi - \beta - \sin(\beta)) \quad (6.24)$$

where $\beta = \max(2(\theta - \alpha_t), 0)$. When the bubble has a full sphere shape, $\beta = 0$ and $A = \pi R^2$

In order to compare the effect of this drag force D_a with that of the buoyancy force, we consider the ratio $r_c = D_a \sin(\alpha_t) / F_b$. To simplify the comparison, we approximate the shape of the bubble as a sphere. In such case, the ratio r_c becomes:

$$r_c = \frac{9\bar{v}(3\rho_l R\bar{v} + 4\mu)}{8\rho_l R^2} \sin(\alpha_t) \quad (6.25)$$

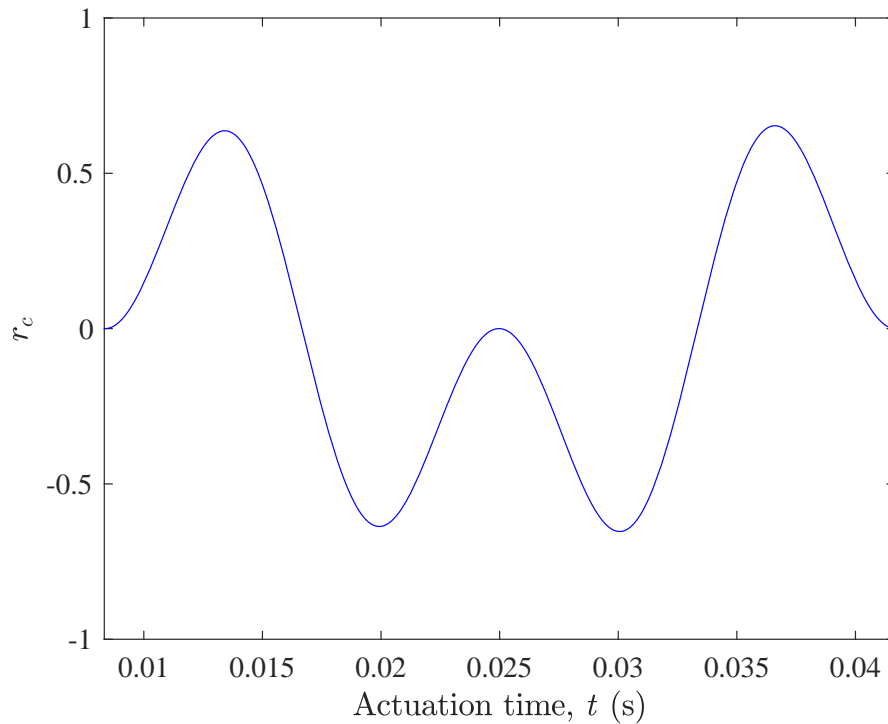


Figure 6.13: A plot of ratio $r_c = D_a \sin(\alpha_t) / F_b$ shows the contribution of drag force to the upward force over one cycle of actuation. The negative value means the opposite direction of D_a

We substitute the liquid properties of FC-72 and the value of largest bubble radius ($R=0.5$ mm) into Eq. (6.25). The applied frequency is $f=30$ Hz and the angular amplitude is 30 degree. The results are plotted in one cycle time of the actuation ($T_c = 1/30$ s). The result in Figure 6.13 shows that the maximum value of r_c is 0.6 obtained at 4 time points of $T_c/8$, $3T_c/8$, $5T_c/8$ and $7T_c/8$. This means that the vertical value of the drag force D_a exceed 60% value of the buoyancy force, which can be consider as a significant value to have an effect on the bubble departure.

Chapter 7

Conclusions and future work

7.1 Conclusions

In summary, three studies on boiling heat transfer on passive and active structured surfaces are presented. While they are separate experiments, their results can support each other and give us a better understanding of the mechanism of boiling process. Each of the approach has its pros and cons and it depends on the application. The passive nanopillars structure offers a consistent enhancement on both CHF and Leidenfrost temperature, which can be used in the cooling system of electrical device with known heat source capacity. On the other hand, the active structure has its flexibility to control the actual heat flux transferred through the surface without replacing the substrate. By this feature, it is more suitable for the applications, in which heat flux needed to be continuously and precisely controlled, such as biomedical and microfluids applications.

7.1.1 Nucleate boiling on passive nanopillar structured substrate.

In this study, we show that nanopillars fabricated on boiling substrates induce a substantial effect on the boiling behaviours in the nucleate boiling regime. In particular, increasing the height of nanopillars effectively leads to considerable enhancement in both heat flux and surface temperature at CHF. We attribute such enhancement to the nanopillar-induced increase in rewetting velocity, which can be measured in a separate wetting experiment. Based on the observations that the rewetting velocity

increases for substrates with higher nanopillars, as well as the assumption that the enhancement in heat flux dominantly takes place at the three-phases contact line, we develop a mechanistic model to predict both the heat flux and the temperature at CHF of nanopillar substrates. The model takes into account the nanoscales of the pillars, and thus, excludes the wicking motion, or imbibition of liquid, as plausible mechanisms for heat transfer enhancement. As a result, the enhanced capillary force due to the presence of nanopillars is the major cause of the intensified rewetting process and subsequent increases in heat flux and temperature at CHF. In particular, the maximum heat transfer rate ($q = 23.6 \text{ W/cm}^2$) and maximum Leidenfrost temperature were obtained on the substrate with the longest nanopillars length ($l = 1390 \text{ nm}$). This result agrees with the conclusion on the influence of rewetting process to heat transfer rate.

The enhancement in both of these critical quantities in pool boiling is a remarkable feature of nanopillar substrates in comparison with nano/micro-engineered substrates in which only either one can be increased. By using only nanopillars with a systematic variation in height and well-defined geometrical dimensions, we have established a direct link between the enhancement in capillary force and the boiling performance of a substrate.

This provides new insights about design of surface textures not only to amplify the heat flux, but also to achieve an enhancement in the temperature at CHF, which is an equally important quantity in preventing boiling crisis.

7.1.2 Convective heat transfer on actuated Nickel strips-array.

In this study, we have shown the effect of actuated strip-array on convective heat transfer and its mechanism. We have successfully designed a boiling rig that met multiple requirements for the experiment, including efficient thermal insulator, heating and condensing modules, optical elements to work with PIV and a system of electro-magnets to generate a proper magnetic field. The actuators have also been optimised in term of flexibility and response to the external magnetic force.

We have found in the experiment results that the convective heat transfer increases with wall temperature. Moreover, this effect is monotonically amplified by

increasing actuated frequency. In the experiment, we obtained the maximum convective heat transfer rate at 0.56 W/cm^2 with the highest actuated frequency $f = 35 \text{ Hz}$. Although this frequency is the maximum limit of our experimental setup, this result shows that the higher frequency can potentially enhance the heat transfer rate even further.

From the observation on high-speed image recording, we have assumed a hypothesis that convective heat transfer is enhanced due to the extra mass transfer caused by the actuation. Based on that assumption, a model has been derived and it showed a good agreement of the experimental data.

This result allowed us to introduce a new coefficient ξ , which represents the extra mass transfer caused by an actuator. In the other words, it provides a new approach to evaluate the enhancement of heat and mass transfer in convective regime. It is worth mentioning that the recent study on convective heat transfer focus on either a forced convection process or a modified liquid such as magnetic nanofluids. These methods, however, require an excessive supplied power or release unwanted residual on the surfaces.

7.1.3 Nucleation of individual vapour bubbles on microheater and microsensor.

In this study, we have presented an exploratory study of the dynamical behaviours of individual vapour bubbles along with measurements of the wall temperature at the nucleation site during the process of nucleate boiling. The temperature of working liquid was kept at 18 K subcooling and the boiling surface was heated by a microheater and an auxiliary cartridge heater. The experiment was conducted with the supplied power P to the microheater in the range $0.35 - 2.32 \text{ MW/m}^2$. The temperature at the nucleation site was measured using an integrated microsensor. The corresponding bubble dynamics were synchronously measured using high-speed imaging.

When the applied power is 0.35 MW/m^2 , bubble delay time t_d and departure diameter D_d are found to be 1.57 s and 0.87 mm, respectively. As P increases from 0.35 MW/m^2 to 2.32 MW/m^2 , the number of bubbles released increases approximately from 2 to 12. It is found that releasing frequency f_d increases 0.068 Hz

to 0.32 Hz and t_d reduces from 1.57 s to 0.01 s as increases from 68 °C to 81 °C. However, D_d showed an insignificant variation within the range of applied power P . It was also observed that the bubbles could nucleate, grow, and detach even at nominally negative wall superheats.

7.2 Future work

For future work, we plan to study further and in more detail on nucleate boiling on other nanopillars substrate and on the effect of the actuation on boiling heat transfer. In particular, we would like vary more surface parameters such as pillar length, spacing and wall slope to investigate its effect on boiling efficiency. For the active case, we would like to vary both the amplitude and the properties of actuators such as shape and size. The PIV measurement will also be considered to provide a confirmation to the flow field inside the bulk liquid. In addition to obtain these results, we intend to carry out the following tasks:

7.2.1 Further analysis on nucleate boiling on nanopillars array by varying more parameters of the structure.

In this thesis, we investigated the enhancement of CHF and Leidenfrost temperature of boiling process on nanopillars array. The structures were varied by the height of nanopillars from hundred of nanometer to above one micrometer. In our next plan, we would like to extend the range of length of the nanopillars and investigate more geometry parameters such as pillar diameter, array spacing and wall slope of the pillar. We hope that this further investigation will lead to more interesting finding on the relation of surface parameters and boiling heat transfer efficiency.

7.2.2 Design actuators with varied shape, size and surface roughness

For each cycle of actuation, the actuator would be able to create different flow intensity depended on its properties such as shape, size, stiffness and surface roughness. For instance, a difference in pillar stiffness can lead to other flow fields as in Figure 7.1. These various effects can be evaluated by the coefficient ξ introduced in

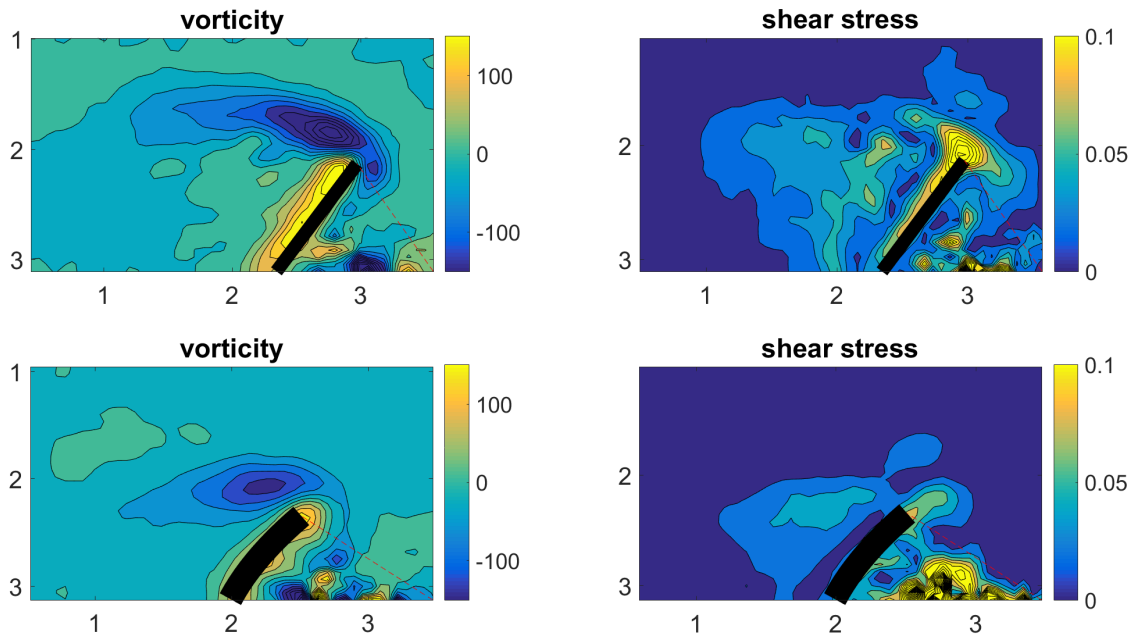


Figure 7.1: PIV image recorded for 10 Hz actuated pillar. The result is shown for rigid pillar (top) and soft pillar (bottom).

Chapter 4. In the future plan, we would like to conduct the boiling experiment on various actuators to have a better definition of ξ in related to these parameters.

On the other hand, the actuated frequency and amplitude are other parameters that evenly contribute to the enhancement of heat transfer. Currently, the actuators in the experiment can only actuated with maximum 35 Hz without reducing the amplitude. That can be improved by applied a stronger magnetic field or replace the material of the actuator. That would be possible since the current electromagnet is relative weak, it only creates a magnetic field of 20 mT.

7.2.3 Velocity field measurement using PIV

The velocity field surrounding an actuator is an important factor to evaluate the effect of this actuation to the bubble nucleation. We expect this velocity field which presented for the local flow of liquid, may affect the departure frequency and the departure diameter of surrounding nucleated bubble by generating some vortexes.

Some preliminary experiments were carried out to obtain this velocity field using PIV method and indeed some vortices were observed surrounding the actuated pillar as in Figure 7.2. Based on this result, we intent to conduct the PIV measurements

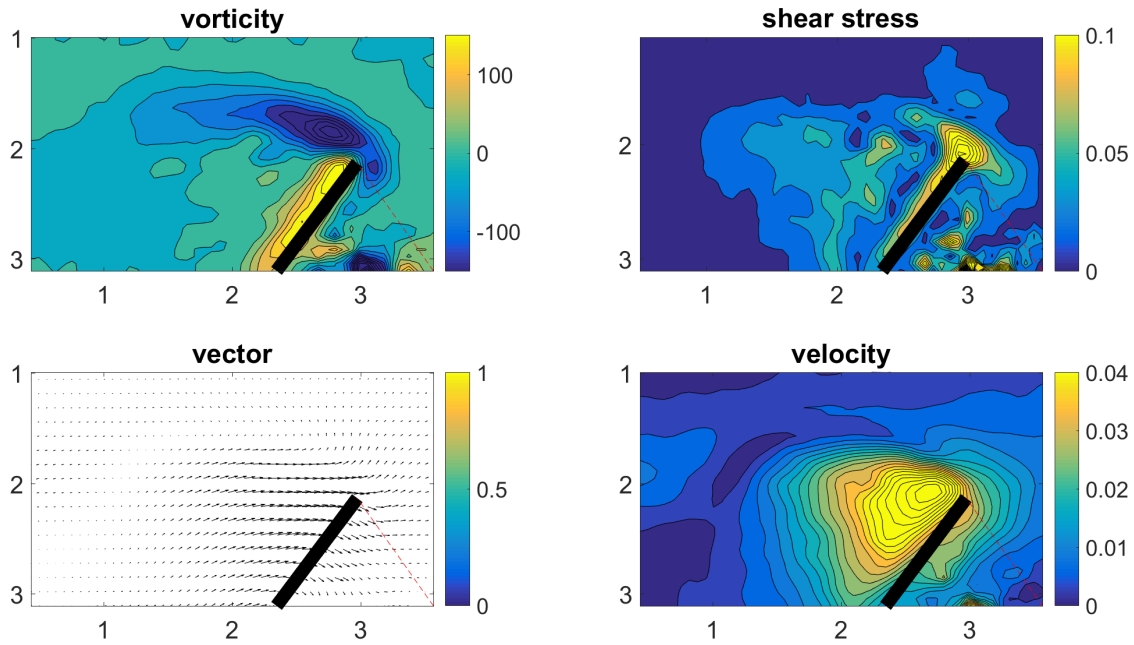


Figure 7.2: One frame of PIV recorded for 10 Hz actuated pillar. The result is in vorticity (1/s), shear stress and velocity.

with various frequencies and amplitudes of the actuated pillars and then compare the experimental results with simulation. The validated results will be used further to investigate the influence of the actuated pillar to a nearby nucleated bubble.

Beside measuring the velocity of an actuated pillar, we also plan to investigate the velocity field surrounding a growing nucleated bubble alone. This result can be used together with the velocity field nearby an actuated pillar to estimate the final velocity when all of them is put together. This will provide more evident to control the actuation in a way that bubble is nucleated and departed from the substrate surface. Therefore, the thermal property of the surface will be modified by changing the applied actuated frequency or amplitude.

References

- [1] A. R. Betz, J. Jenkins, C.J. Kim, and D. Attinger. Boiling heat transfer on superhydrophilic, superhydrophobic, and superbiphilic surfaces. *International Journal of Heat and Mass Transfer*, 57(2):733–741, 2013.
- [2] V. P. Carey. *Liquid-vapor Phase-Change Phenomena*. CRC Press, 2007.
- [3] H. Steiner, G. Brenn, F. Ramstorfer, and B. Breitschädel. *Increased Cooling Power with Nucleate Boiling Flow in Automotive Engine Applications*, book section 13. InTech, Rijeka, 2011.
- [4] C. Hutter, K. Sefiane, T. G. Karayiannis, A. J. Walton, R. A. Nelson, and D. B. R. Kenning. Nucleation site interaction between artificial cavities during nucleate pool boiling on silicon with integrated micro-heater and temperature micro-sensors. *International Journal of Heat and Mass Transfer*, 55(11):2769 – 2778, 2012.
- [5] S. Nukiyama. The maximum and minimum values of the heat q transmitted from metal to boiling water under atmospheric pressure. *International Journal of Heat and Mass Transfer*, 9(12):1419 – 1433, 1966.
- [6] M.-C. Lu, R. Chen, V. Srinivasan, V. P. Carey, and A. Majumdar. Critical heat flux of pool boiling on si nanowire array-coated surfaces. *International Journal of Heat and Mass Transfer*, 54(25):5359 – 5367, 2011.
- [7] D. B. R. Kenning. *Nucleate boiling*, February 2011. [Online; posted 4-February-2011].
- [8] W. Fritz. Maximum volume of vapor bubbles. *Physikalische Zeitschrift*, 36:379–384, 1935.

- [9] L.-H. Chien and R. L. Webb. A nucleate boiling model for structured enhanced surfaces. *International Journal of Heat and Mass Transfer*, 41(14):2183 – 2195, 1998.
- [10] S. I. Haider and R. L. Webb. A transient micro-convection model of nucleate pool boiling. *International Journal of Heat and Mass Transfer*, 40(15):3675 – 3688, 1997.
- [11] Y. Haramura and Y. Katto. A new hydrodynamic model of critical heat flux, applicable widely to both pool and forced convection boiling on submerged bodies in saturated liquids. *International Journal of Heat and Mass Transfer*, 26(3):389 – 399, 1983.
- [12] Y. Y. Jiang, H. Osada, M. Inagaki, and N. Horinouchi. Dynamic modeling on bubble growth, detachment and heat transfer for hybrid-scheme computations of nucleate boiling. *International Journal of Heat and Mass Transfer*, 56(1):640 – 652, 2013.
- [13] C. L. Tien. A hydrodynamic model for nucleate pool boiling. *International Journal of Heat and Mass Transfer*, 5(6):533 – 540, 1962.
- [14] S. R. Yang and R. H. Kim. A mathematical model of the pool boiling nucleation site density in terms of the surface characteristics. *International Journal of Heat and Mass Transfer*, 31(6):1127 – 1135, 1988.
- [15] L. Z. Zeng, J. F. Klausner, D. M. Bernhard, and R. Mei. A unified model for the prediction of bubble detachment diameters in boiling systems—ii. flow boiling. *International Journal of Heat and Mass Transfer*, 36(9):2271 – 2279, 1993.
- [16] J. Kim. Review of nucleate pool boiling bubble heat transfer mechanisms. *International Journal of Multiphase Flow*, 35(12):1067–1076, 2009.
- [17] B. B. Mikic and W. M. Rohsenow. A new correlation of pool-boiling data including the effect of heating surface characteristics. *Journal of Heat Transfer*, 91(2):245–250, 1969.

- [18] C.-Y. Han and P. Griffith. The mechanism of heat transfer in nucleate pool boiling—part ii: The heat flux-temperature difference relation. *International Journal of Heat and Mass Transfer*, 8(6):905 – 914, 1965.
- [19] P. Stephan and J. Hammer. A new model for nucleate boiling heat transfer. *Heat and Mass Transfer*, 30(2):119–125, 1994.
- [20] S. G. Bankoff, W. J. J. Colahan, and D. R. Bartz. *Summary of conference on bubble dynamics and boiling heat transfer held at the jet propulsion laboratory, June 14 and 15, 1956*. 1956.
- [21] F. D. Moore and R. B. Mesler. The measurement of rapid surface temperature fluctuations during nucleate boiling of water. *AIChE Journal*, 7(4):620–624, 1961.
- [22] R. C. Hendricks and R. R. Sharp. Initiation of cooling due to bubble growth on a heating surface. Report, NASA Lewis Research Center; Cleveland, OH, United States, 1964.
- [23] G. Son and V. K. Dhir. Numerical simulation of nucleate boiling on a horizontal surface at high heat fluxes. *International Journal of Heat and Mass Transfer*, 51(9):2566 – 2582, 2008.
- [24] A. Sanna, C. Hutter, D. B. R. Kenning, T. G. Karayiannis, K. Sefiane, and R. A. Nelson. Numerical investigation of nucleate boiling heat transfer on thin substrates. *International Journal of Heat and Mass Transfer*, 76(Supplement C):45 – 64, 2014.
- [25] P. Genske and K. Stephan. Numerical simulation of heat transfer during growth of single vapor bubbles in nucleate boiling. *International Journal of Thermal Sciences*, 45(3):299 – 309, 2006.
- [26] R. Zhuan and W. Wang. Simulation on nucleate boiling in micro-channel. *International Journal of Heat and Mass Transfer*, 53(1):502 – 512, 2010.
- [27] S. Narumanchi, A. Troshko, D. Bharathan, and V. Hassani. Numerical simulations of nucleate boiling in impinging jets: Applications in power electronics cooling. *International Journal of Heat and Mass Transfer*, 51(1):1 – 12, 2008.

- [28] S. Jung and H. Kim. An experimental method to simultaneously measure the dynamics and heat transfer associated with a single bubble during nucleate boiling on a horizontal surface. *International Journal of Heat and Mass Transfer*, 73(Supplement C):365 – 375, 2014.
- [29] G. Hong, X. Yan, Y.-H. Yang, S. Liu, and Y. p. Huang. Experimental study on onset of nucleate boiling in narrow rectangular channel under static and heaving conditions. *Annals of Nuclear Energy*, 39(1):26 – 34, 2012.
- [30] Y. Rousselet, G. R. Warrier, and V. K. Dhir. Experimental study of bubble dynamics during nucleate flow boiling on horizontal and vertical surfaces. *Journal of Enhanced Heat Transfer*, 21(4-5):259 – 282, 2014.
- [31] A. Najim and A. R. Aacharya. Experimental study of effect of nucleation site size on bubble dynamics during nucleate pool boiling heat transfer. In *Dynamics of Machines and Mechanisms, Industrial Research*, volume 592 of *Applied Mechanics and Materials*, pages 1596–1600. Trans Tech Publications.
- [32] T. Chen. An experimental investigation of nucleate boiling heat transfer from an enhanced cylindrical surface. *Applied Thermal Engineering*, 59(1):355 – 361, 2013.
- [33] S. Fischer, S. Herbert, A. Sielaff, E. M. Slomski, P. Stephan, and M. Oechsner. Experimental investigation of nucleate boiling on a thermal capacitive heater under variable gravity conditions. *Microgravity Science and Technology*, 24(3):139–146, 2012.
- [34] X. Ma, C. Yu, Z. Lan, D. Wang, and T. Bai. Experimental study of nucleate boiling heat transfer using enhanced space-confined structures. *Journal of Heat Transfer*, 134(6):061501 – 061501, 2012.
- [35] Y.-F. Xue, J.-F. Zhao, J.-J. Wei, J. Li, D. Guo, and S.-X. Wan. Experimental study of nucleate pool boiling of FC-72 on smooth surface under microgravity. *Microgravity Science and Technology*, 23(1):75, 2011.
- [36] A. Sathyabhama and T. P. A. Babu. Experimental study of nucleate pool boiling heat transfer to ammonia–water–lithium bromide solution. *Experimental Thermal and Fluid Science*, 35(6):1046 – 1054, 2011.

- [37] G. Sateesh, S. K. Das, and A. R. Balakrishnan. Experimental studies on the effect of tube inclination on nucleate pool boiling. *Heat and Mass Transfer*, 45(12):1493–1502, 2009.
- [38] S. Moghaddam and K. Kiger. Physical mechanisms of heat transfer during single bubble nucleate boiling of FC-72 under saturation conditions. ii: Theoretical analysis. *International Journal of Heat and Mass Transfer*, 52(5):1295 – 1303, 2009.
- [39] G. Ribatski, J. M. S. Jabardo, and E. F. da Silva. Modeling and experimental study of nucleate boiling on a vertical array of horizontal plain tubes. *Experimental Thermal and Fluid Science*, 32(8):1530 – 1537, 2008.
- [40] Y. H. Zhao, Y. H. Diao, and T. Takaharu. Experimental investigation in nucleate pool boiling of binary refrigerant mixtures. *Applied Thermal Engineering*, 28(2):110 – 115, 2008.
- [41] E. Wagner, C. Sodtke, N. Schweizer, and P. Stephan. Experimental study of nucleate boiling heat transfer under low gravity conditions using tics for high resolution temperature measurements. *Heat and Mass Transfer*, 42(10):875–883, 2006.
- [42] J. Kim, J. Lee, and M. H. Kim. Experimental study on single bubble growth under subcooled, saturated, and superheated nucleate pool boiling. *Journal of Mechanical Science and Technology*, 20(5):692–709, 2006.
- [43] J. Kim, B. D. Oh, and M. H. Kim. Experimental study of pool temperature effects on nucleate pool boiling. *International Journal of Multiphase Flow*, 32(2):208 – 231, 2006.
- [44] S. Chatpun, M. Watanabe, and M. Shoji. Experimental study on characteristics of nucleate pool boiling by the effects of cavity arrangement. *Experimental Thermal and Fluid Science*, 29(1):33 – 40, 2004.
- [45] G. Barthau and E. Hahne. Experimental study of nucleate pool boiling of r134a on a stainless steel tube. *International Journal of Heat and Fluid Flow*, 25(2):305 – 312, 2004.

- [46] Y. Zhao, T. Tsuruta, and C. Ji. Experimental study of nucleate boiling heat transfer enhancement in a confined space. *Experimental Thermal and Fluid Science*, 28(1):9 – 16, 2003.
- [47] G. Ribatski and J. M. S. Jabardo. Experimental study of nucleate boiling of halocarbon refrigerants on cylindrical surfaces. *International Journal of Heat and Mass Transfer*, 46(23):4439 – 4451, 2003.
- [48] P. M. C. V. P. Masson. An experimental study of the two-phase flow adjacent to a wire in nucleate boiling under an electric field. *Experimental Heat Transfer*, 13(2):107–123, 2000.
- [49] J. Bonjour, M. Clause, and M. Lallemand. Experimental study of the coalescence phenomenon during nucleate pool boiling. *Experimental Thermal and Fluid Science*, 20(3):180 – 187, 2000.
- [50] G. F. Naterer, W. Hendradjit, K. J. Ahn, and J. E. S. Venart. Near-wall microlayer evaporation analysis and experimental study of nucleate pool boiling on inclined surfaces. *Journal of Heat Transfer*, 120(3):641 – 653, 1998.
- [51] T. C. Wang, T. J. Snyder, and J. N. Chung. Experimental examination of forced-convection subcooled nucleate boiling and its application in microgravity. *Journal of Heat Transfer*, 118(1):237 – 241, 1996.
- [52] P. M. Carrica, S. A. Leonardi, and A. Clause. Experimental study of the two-phase flow dynamics in nucleate and film pool boiling. *International Journal of Multiphase Flow*, 21(3):405 – 418, 1995.
- [53] T. Usui, K. Aizawa, and Y. Sano. Experimental study of nucleate boiling on surface of cooling channel of silicon crystal. In *Proceedings of SPIE*, volume 1739, pages 1739 – 1739 – 8, 1993.
- [54] M. M. Shah. A survey of experimental heat transfer data for nucleate pool boiling of liquid metals and a new correlation. *International Journal of Heat and Fluid Flow*, 13(4):370 – 379, 1992.
- [55] D. Dix and J. Orozco. An experimental study in nucleate boiling heat transfer from a sphere. *Journal of Heat Transfer*, 112(1):258 – 263, 1990.

- [56] S. M. You, T. W. Simon, A. Bar-Cohen, and W. Tong. Experimental investigation of nucleate boiling incipience with a highly-wetting dielectric fluid (r-113). *International Journal of Heat and Mass Transfer*, 33(1):105 – 117, 1990.
- [57] S. U. D. O. Yukio, K. MIYATA, H. IKAWA, and M. KAMINAGA. Experimental study of incipient nucleate boiling in narrow vertical rectangular channel simulating subchannel of upgraded jrr-3. *Journal of Nuclear Science and Technology*, 23(1):73–82, 1986.
- [58] E. A. Ibrahim and R. L. Judd. An experimental investigation of the effect of subcooling on bubble growth and waiting time in nucleate boiling. *Journal of Heat Transfer*, 107(1):168 – 174, 1985.
- [59] R. Bartolini, G. Guglielmini, and E. Nannei. Experimental study on nucleate boiling of water in vertical upflow and downflow. *International Journal of Multiphase Flow*, 9(2):161 – 165, 1983.
- [60] A. Ali and R. L. Judd. An analytical and experimental investigation of bubble waiting time in nucleate boiling. *Journal of Heat Transfer*, 103(4):673 – 678, 1981.
- [61] V. A. Grigor'ev, A. V. Klimenko, Y. M. Pavlov, and E. V. Ametistov. Experimental investigation of the dependence of heat transfer during nucleate boiling on the thickness of the heating wall and metallic coatings. *High Temp. (USSR) (Engl. Transl.); (United States)*, 16:1, 1978.
- [62] F. W. Schmidt, D. F. Torok, and G. E. Robinson. Experimental study of the effects of an ultrasonic field in a nucleate boiling system. *Journal of Heat Transfer*, 89(4):289 – 294, 1967.
- [63] D. E. Drayer. Nucleate boiling of hydrogen. comparison between experimental and predicted data. *Industrial and Engineering Chemistry Fundamentals*, Vol: 4, 1965.
- [64] L. Xu, J. Xu, B. Wang, and W. Zhang. Pool boiling heat transfer on the micro-heater surface with and without nanoparticles by pulse heating. *International Journal of Heat and Mass Transfer*, 54(15):3309 – 3322, 2011.

- [65] G. Chen, X. Quan, and P. Cheng. Effects of surfactant additive on flow boiling over a microheater under pulse heating. *International Journal of Heat and Mass Transfer*, 53(7):1586 – 1590, 2010.
- [66] G. Chen and P. Cheng. Nucleate and film boiling on a microheater under pulse heating in a microchannel. *International Communications in Heat and Mass Transfer*, 36(5):391 – 396, 2009.
- [67] C. Herman, C. Herman, J. Kim, and J. Kim. Heat transfer and bubble detachment in subcooled pool boiling from a downward-facing microheater array in a nonuniform electric field. *Annals of the New York Academy of Sciences*, 1161:182–91, 2009.
- [68] J. Li, G. P. Peterson, and P. Cheng. Dynamic characteristics of transient boiling on a square platinum microheater under millisecond pulsed heating. *International Journal of Heat and Mass Transfer*, 51(1):273 – 282, 2008.
- [69] Y. D. Varlamov, Y. P. Meshcheryakov, S. I. Lezhnin, M. R. Predtechenskii, and S. N. Ul'yankin. Evolution of a vapor cavity during explosive boiling on a film microheater: Experiment and numerical simulation. *Journal of Applied Mechanics and Technical Physics*, 48(4):534–541, 2007.
- [70] Y. D. Varlamov, Y. P. Meshcheryakov, M. P. Predtechenskii, S. I. Lezhnin, and S. N. Ul'yankin. Specific features of explosive boiling of liquids on a film microheater. *Journal of Applied Mechanics and Technical Physics*, 48(2):213–220, 2007.
- [71] T. Chen, J. F. Klausner, S. V. Garimella, and J. N. Chung. Subcooled boiling incipience on a highly smooth microheater. *International Journal of Heat and Mass Transfer*, 49(23):4399 – 4406, 2006.
- [72] C. D. Henry and J. Kim. Thermocapillary effects on low-g pool boiling from microheater arrays of various aspect ratio. *Microgravity - Science and Technology*, 16(1):170, 2005.
- [73] T. Chen, J. F. Klausner, and J. N. Chung. Subcooled boiling heat transfer and dryout on a constant temperature microheater. *International Journal of Heat and Fluid Flow*, 25(2):274 – 287, 2004.

- [74] H. S. Ahn, N. Sinha, and D. Banerjee. Micro-machined temperature sensor arrays for studying micro-scale features in film boiling. In *ASME Proceedings, Heat Transfer, Part B*, pages 317 – 324, 2005.
- [75] H. Ammar, D. Hamadi, B. Garnier, A. Ould El Moctar, H. Peerhossaini, F. Monti, and H. Willaime. Thin-film heat-flux microsensor for heat-transfer measurement in micro-heat exchangers/microreactors. In *ASME 2012 10th International Conference on Nanochannels, Microchannels, and Minichannels*, pages 781 – 788, 2012.
- [76] C. Baojun, Z. Chongquan, Y. Suying, and Y. Ming. The application of soft-sensor technology in measuring water boiling point. In *2007 Chinese Control Conference*, volume 6, pages 372–376.
- [77] B. Garnier, H. Willaime, F. Monti, and H. Peerhossaini. A novel thin-film temperature and heat-flux microsensor for heat transfer measurements in microchannels. *Lab on a Chip*, 12(3):652 – 658, 2012.
- [78] J. P. McHale and S. V. Garimella. Nucleate boiling from smooth and rough surfaces – part 1: Fabrication and characterization of an optically transparent heater–sensor substrate with controlled surface roughness. *Experimental Thermal and Fluid Science*, 44(Supplement C):456 – 467, 2013.
- [79] Osamu T. a. Yabuki. Approach to heat transfer mechanism beneath boiling bubble with mems sensor, 2009.
- [80] T. Yabuki and O. Nakabeppu. Heat transfer mechanisms in isolated bubble boiling of water observed with mems sensor. *International Journal of Heat and Mass Transfer*, 76(Supplement C):286 – 297, 2014.
- [81] T. Yabuki, R. Samaroo, O. Nakabeppu, and M. Kawaji. Mems sensor measurement of surface temperature response during subcooled flow boiling in a rectangular flow channel. *Experimental Thermal and Fluid Science*, 67(Supplement C):24 – 29, 2015.
- [82] N. Yaddanapudi and J. Kim. Single bubble heat transfer in saturated pool boiling of FC-72. *Multiphase Science and Technology*, 12(3-4), 2000.

- [83] F. Demiray and J. Kim. Microscale heat transfer measurements during pool boiling of FC-72: effect of subcooling. *International Journal of Heat and Mass Transfer*, 47(14):3257 – 3268, 2004.
- [84] L. H. Chai, X. F. Peng, and B. X. Wang. Nucleation site interaction during boiling. *International Journal of Heat and Mass Transfer*, 43(23):4249 – 4258, 2000.
- [85] L. Zhang and M. Shoji. Nucleation site interaction in pool boiling on the artificial surface. *International Journal of Heat and Mass Transfer*, 46(3):513 – 522, 2003.
- [86] A. Coulibaly, X. Lin, J. Bi, and D. M. Christopher. Bubble coalescence at constant wall temperatures during subcooled nucleate pool boiling. *Experimental Thermal and Fluid Science*, 44(Supplement C):209 – 218, 2013.
- [87] Y. A. Buyevich and B. W. Webbon. The isolated bubble regime in pool nucleate boiling. *International Journal of Heat and Mass Transfer*, 40(2):365 – 377, 1997.
- [88] T. Chen and J. N. Chung. Coalescence of bubbles in nucleate boiling on microheaters. *International Journal of Heat and Mass Transfer*, 45(11):2329 – 2341, 2002.
- [89] J. Bi, D. M. Christopher, X. Lin, and X. Li. Effects of nucleation site arrangement and spacing on bubble coalescence characteristics. *Experimental Thermal and Fluid Science*, 52(Supplement C):116 – 127, 2014.
- [90] Y. Utaka, Y. Kashiwabara, and M. Ozaki. Microlayer structure in nucleate boiling of water and ethanol at atmospheric pressure. *International Journal of Heat and Mass Transfer*, 57(1):222 – 230, 2013.
- [91] R. R. Sharp. The nature of liquid film evaporation during nucleate boiling. Report, NASA Lewis Research Center; Cleveland, OH, United States, 1964.
- [92] H. H. Jawurek. Simultaneous determination of microlayer geometry and bubble growth in nucleate boiling. *International Journal of Heat and Mass Transfer*, 12(8):843 – 848, 1969.

- [93] E. Wagner and P. Stephan. High-resolution measurements at nucleate boiling of pure FC-84 and FC-3284 and its binary mixtures. *Journal of Heat Transfer*, 131(12):121008 – 121008–12, 2009.
- [94] Y. Utaka, Y. Kashiwabara, M. Ozaki, and Z. Chen. Heat transfer characteristics based on microlayer structure in nucleate pool boiling for water and ethanol. *International Journal of Heat and Mass Transfer*, 68(Supplement C):479 – 488, 2014.
- [95] C. M. Voutsinos and R. L. Judd. Laser interferometric investigation of the microlayer evaporation phenomenon. *Journal of Heat Transfer*, 97(1):88 – 92, 1975.
- [96] T. Yabuki and O. Nakabeppu. On heat transfer mechanism of nucleate boiling with mems sensors (3rd report, evaluation of the approach method and heat transfer characteristics of isolated boiling bubble). 76:1932–1941, 2010.
- [97] H. S. Ahn, H. J. Jo, S. H. Kang, and M. H. Kim. Effect of liquid spreading due to nano/microstructures on the critical heat flux during pool boiling. *Applied Physics Letters*, 98(7):071908, 2011.
- [98] R. J. Benjamin and A. R. Balakrishnan. Nucleation site density in pool boiling of saturated pure liquids: Effect of surface microroughness and surface and liquid physical properties. *Experimental Thermal and Fluid Science*, 15(1):32 – 42, 1997.
- [99] R. Chen, M.-C. Lu, V. Srinivasan, Z. Wang, H. H. Cho, and A. Majumdar. Nanowires for enhanced boiling heat transfer. *Nano letters*, 9(2):548–553, 2009.
- [100] K. Ferjančič and I. Golobič. Surface effects on pool boiling CHF. *Experimental Thermal and Fluid Science*, 25(7):565 – 571, 2002.
- [101] T. J. Hendricks, S. Krishnan, C. Choi, C.-H. Chang, and B. Paul. Enhancement of pool-boiling heat transfer using nanostructured surfaces on aluminum and copper. *International Journal of Heat and Mass Transfer*, 53(15):3357 – 3365, 2010.

- [102] S. G. Kandlikar. A theoretical model to predict pool boiling chf incorporating effects of contact angle and orientation. *Journal of Heat Transfer*, 123(6):1071 – 1079, 2001.
- [103] S. J. Kim, I. C. Bang, J. Buongiorno, and L. W. Hu. Effects of nanoparticle deposition on surface wettability influencing boiling heat transfer in nanofluids. *Applied Physics Letters*, 89(15):153107, 2006.
- [104] S. Kim, H. D. Kim, H. Kim, H. S. Ahn, H. Jo, J. Kim, and M. H. Kim. Effects of nano-fluid and surfaces with nano structure on the increase of chf. *Experimental Thermal and Fluid Science*, 34(4):487 – 495, 2010.
- [105] C. Li, Z. Wang, P.-I. Wang, Y. Peles, N. Koratkar, and G. P. Peterson. Nanostructured copper interfaces for enhanced boiling. *Small*, 4(8):1084–1088, 2008.
- [106] Y. Nam, J. Wu, G. Warrier, and Y. S. Ju. Experimental and numerical study of single bubble dynamics on a hydrophobic surface. *Journal of Heat Transfer*, 131(12):121004–121004–7, 2009.
- [107] M. Sesen, W. Khudhayer, T. Karabacak, and A. Kosar. Compact nanostructure integrated pool boiler for microscale cooling applications. *IET Micro Nano Letters*, 5(4):203–206, 2010.
- [108] Y. Takata, S. Hidaka, M. Masuda, and T. Ito. Pool boiling on a superhydrophilic surface. *International Journal of Energy Research*, 27(2):111–119, 2003.
- [109] K. C. Ng, A. Chakraborty, S. M. Aye, and X. Wang. New pool boiling data for water with copper-foam metal at sub-atmospheric pressures: Experiments and correlation. *Applied Thermal Engineering*, 26(11):1286 – 1290, 2006.
- [110] D. M. Vazquez and R. Kumar. Surface effects of ribbon heaters on critical heat flux in nanofluid pool boiling. *International Communications in Heat and Mass Transfer*, 41(Supplement C):1 – 9, 2013.
- [111] J. Y. Ho, K. K. Wong, and K. C. Leong. Saturated pool boiling of FC-72 from enhanced surfaces produced by selective laser melting. *International Journal of Heat and Mass Transfer*, 99:107 – 121, 2016.

- [112] J. Y. Ho, K. C. Leong, and C. Yang. Saturated pool boiling from carbon nanotube coated surfaces at different orientations. *International Journal of Heat and Mass Transfer*, 79:893 – 904, 2014.
- [113] I. Pranoto, K. C. Leong, and L. W. Jin. The role of graphite foam pore structure on saturated pool boiling enhancement. *Applied Thermal Engineering*, 42:163 – 172, 2012.
- [114] L. W. Jin, K. C. Leong, and I. Pranoto. Saturated pool boiling heat transfer from highly conductive graphite foams. *Applied Thermal Engineering*, 31(14):2685 – 2693, 2011.
- [115] M. Zupančič, M. Steinbücher, P. Gregorčič, and I. Golobič. Enhanced pool-boiling heat transfer on laser-made hydrophobic/superhydrophilic polydimethylsiloxane-silica patterned surfaces. *Applied Thermal Engineering*, 91:288–297, 2015.
- [116] S. Mori and K. Okuyama. Enhancement of the critical heat flux in saturated pool boiling using honeycomb porous media. *International Journal of Multiphase Flow*, 35(10):946 – 951, 2009.
- [117] K. K. Wong and K. C. Leong. Saturated pool boiling enhancement using porous lattice structures produced by selective laser melting. *International Journal of Heat and Mass Transfer*, 121:46 – 63, 2018.
- [118] D. Zhong, J. Meng, Z. Li, and Z. Guo. Experimental study of saturated pool boiling from downward facing surfaces with artificial cavities. *Experimental Thermal and Fluid Science*, 68:442–451, 2015.
- [119] C. H. Li and P. R. P. Russell. Independent and collective roles of surface structures at different length scales on pool boiling heat transfer. *Scientific Reports*, 6, 2016.
- [120] M. M. Rahman, J. Pollack, and M. McCarthy. Increasing boiling heat transfer using low conductivity materials. *Scientific Reports*, 5, 2015.
- [121] N. S. Dhillon, J. Buongiorno, and K. K. Varanasi. Critical heat flux maxima during boiling crisis on textured surfaces. *Nature Communications*, 6, 2015.

- [122] M. M. Rahman, E. Olceroglu, and M. McCarthy. Role of wickability on the critical heat flux of structured superhydrophilic surfaces. *Langmuir*, 30(37):11225–11234, 2014.
- [123] D. B. R. Kenning. *Pool boiling*, February 2011. [Online; posted 7- February-2011].
- [124] Y. Takata, S. Hidaka, and T. Uruguchi. Boiling feature on a super water-repellent surface. *Heat Transfer Engineering*, 27(8):25–30, 2006.
- [125] S. Abishek, R. Narayanaswamy, and V. Narayanan. Effect of heater size and reynolds number on the partitioning of surface heat flux in subcooled jet impingement boiling. *International Journal of Heat and Mass Transfer*, 59(Supplement C):247 – 261, 2013.
- [126] C. O. Gersey and I. Mudawar. Effects of heater length and orientation on the trigger mechanism for near-saturated flow boiling critical heat flux—i. photographic study and statistical characterization of the near-wall interfacial features. *International Journal of Heat and Mass Transfer*, 38(4):629 – 641, 1995.
- [127] P. J. Giarratano. Transient boiling heat transfer from two different heat sources: Small diameter wire and thin film flat surface on a quartz substrate. *International Journal of Heat and Mass Transfer*, 27(8):1311 – 1318, 1984.
- [128] T. J. Heindel, S. Ramadhyani, and F. P. Incropera. Liquid immersion cooling of a longitudinal array of discrete heat sources in protruding substrates: Ii—forced convection boiling. *Journal of Electronic Packaging*, 114(1):63 – 70, 1992.
- [129] I. A. Mudawwar, T. A. Incropera, and F. P. Incropera. Boiling heat transfer and critical heat flux in liquid films falling on vertically-mounted heat sources. *International Journal of Heat and Mass Transfer*, 30(10):2083 – 2095, 1987.
- [130] K. N. Rainey and S. M. You. Effects of heater size and orientation on pool boiling heat transfer from microporous coated surfaces. *International Journal of Heat and Mass Transfer*, 44(14):2589 – 2599, 2001.

- [131] M. Ochsner, M. R. Dusseiller, H. M. Grandin, S. Luna-Morris, M. Textor, V. Vogel, and M. L. Smith. Micro-well arrays for 3d shape control and high resolution analysis of single cells. *Lab on a Chip*, 7:1074–1077, 2007.
- [132] S. Ujereh, T. Fisher, and I. Mudawar. Effects of carbon nanotube arrays on nucleate pool boiling. *International Journal of Heat and Mass Transfer*, 50(19):4023–4038, 2007.
- [133] W. M. Rohsenow. A method of correlating heat transfer data for surface boiling of liquids. Report, Cambridge, Mass.: MIT Division of Industrial Cooperation,[1951], 1951.
- [134] N. Zuber. *Hydrodynamic Aspects of Boiling Heat Transfer (thesis)*. Report, California. Univ., Los Angeles; and Ramo-Wooldridge Corp., Los Angeles, 1959.
- [135] A. Bejan and A. D. Kraus. *Heat Transfer Handbook*, volume 1. John Wiley & Sons, 2003.
- [136] H. Nair, H. J. J. Staat, T. Tran, A. van Houselt, A. Prosperetti, D. Lohse, and C. Sun. The leidenfrost temperature increase for impacting droplets on carbon-nanofiber surfaces. *Soft matter*, 10(13):2102–2109, 2014.
- [137] H. M. Kwon, J. C. Bird, and K. K. Varanasi. Increasing leidenfrost point using micro-nano hierarchical surface structures. *Applied Physics Letters*, 103(20):201601, 2013.
- [138] H. S. Ahn, N. Sinha, M. Zhang, D. Banerjee, S. Fang, and R. H. Baughman. Pool boiling experiments on multiwalled carbon nanotube (mwcnt) forests. *Journal of Heat Transfer*, 128(12):1335–1342, 2006.
- [139] V. Sathyamurthi, H. S. Ahn, D. Banerjee, and S. C. Lau. Subcooled pool boiling experiments on horizontal heaters coated with carbon nanotubes. *Journal of Heat Transfer*, 131(7):071501, 2009.
- [140] S. Vemuri and K. J. Kim. Pool boiling of saturated FC-72 on nano-porous surface. *International Communications in Heat and Mass transfer*, 32(1):27–31, 2005.

- [141] W. Wu, H. Bostanci, L. C. Chow, Y. Hong, M. Su, and J. P. Kizito. Nucleate boiling heat transfer enhancement for water and FC-72 on titanium oxide and silicon oxide surfaces. *International Journal of Heat and Mass Transfer*, 53(9):1773–1777, 2010.
- [142] S. Launay, A. G. Fedorov, Y. Joshi, A. Cao, and P. M. Ajayan. Hybrid micro-nano structured thermal interfaces for pool boiling heat transfer enhancement. *Microelectronics Journal*, 37(11):1158–1164, 2006.
- [143] C. Li, Z. Wang, P.-I. Wang, Y. Peles, N. Koratkar, and G. P. Peterson. Nano-structured copper interfaces for enhanced boiling. *Small*, 4(8):1084–1088, 2008.
- [144] Y. Im, Y. Joshi, C. Dietz, and S. S. Lee. Enhanced boiling of a dielectric liquid on copper nanowire surfaces. *International Journal of Micro-Nano Scale Transport*, 1(1):79–95, 2010.
- [145] B. S. Kim, G. S. Choi, S. Shin, T. Gemming, and H. H. Cho. Nano-inspired fluidic interactivity for boiling heat transfer: impact and criteria. *Scientific Reports*, 6:34348, 2016.
- [146] M. G. Cooper and T. T. Chandratilleke. Growth of diffusion-controlled vapour bubbles at a wall in a known temperature gradient. *International Journal of Heat and Mass Transfer*, 24(9):1475–1492, 1981.
- [147] A. Zou, D. P. Singh, and S. C. Maroo. Early evaporation of microlayer for boiling heat transfer enhancement. *Langmuir*, 32(42):10808–10814, 2016.
- [148] J. H. Lienhard and V. K. Dhir. Extended hydrodynamic theory of the peak and minimum pool boiling heat fluxes. Report, University of Kentucky, 1973.
- [149] S.A. Nada. Natural convection heat transfer in horizontal and vertical closed narrow enclosures with heated rectangular finned base plate. *International Journal of Heat and Mass Transfer*, 50(3):667 – 679, 2007.
- [150] Platzer Bernd. A. Bejan: Convection Heat Transfer. John Wiley & Sons, Hoboken, New Jersey, 4th ed., 2013. *ZAMM - Journal of Applied Mathematics and Mechanics / Zeitschrift für Angewandte Mathematik und Mechanik*, 94(9):729–729.

- [151] Acrivos Andreas. Combined laminar free- and forced-convection heat transfer in external flows. *AIChE Journal*, 4(3):285–289.
- [152] K. K. Prasad and V. Ramanath. Heat-transfer by free convection from a longitudinally vibrating vertical plate. *International Journal of Heat and Mass Transfer*, 15(6):1213–1233, 1972. n/a.
- [153] W. H. Besant. *A treatise on hydrostatics and hydrodynamics*. Bell Deighton, 1859.
- [154] S.J. Board and R.B. Duffey. Spherical vapour bubble growth in superheated liquids. *Chemical Engineering Science*, 26(3):263 – 274, 1971.
- [155] S. K. Kasimsetty, A. Subramani, R. M. Manglik, and M. A. Jog. Theoretical modeling and experimental measurements of single bubble dynamics from a submerged orifice in a liquid pool. (42762):9–17, 2007. 10.1115/HT2007-32088.
- [156] M. Zupančič, M. Može, P. Gregorčič, A. Sitar, and I. Golobič. Evaluation of enhanced nucleate boiling performance through wall-temperature distributions on pdms-silica coated and non-coated laser textured stainless steel surfaces. *International Journal of Heat and Mass Transfer*, 111:419–428, 2017.
- [157] X. Ye and L. Qi. Two-dimensionally patterned nanostructures based on monolayer colloidal crystals: controllable fabrication, assembly, and applications. *Nano Today*, 6(6):608–631, 2011.
- [158] J. Yu, C. Geng, L. Zheng, Z. Ma, T. Tan, X. Wang, Q. Yan, and D. Shen. Preparation of high-quality colloidal mask for nanosphere lithography by a combination of air/water interface self-assembly and solvent vapor annealing. *Langmuir*, 28(34):12681–12689, 2012.
- [159] G. D. Moon, T. I. Lee, B. Kim, G. Chae, J. Kim, S. Kim, J.-M. Myoung, and U. Jeong. Assembled monolayers of hydrophilic particles on water surfaces. *ACS Nano*, 5(11):8600–8612, 2011.
- [160] K. J. L. Geisler and A. Bar-Cohen. Nucleate pool boiling heat transfer in narrow vertical channels. In *Proceedings of the International Conference on Boiling Heat Transfer*, volume Section XII, page 5.

- [161] J. C. Passos, F. R. Hirata, L. F. B. Possamai, M. Balsamo, and M. Misale.
Conned boiling of FC72 and FC87 on a downward facing heating copper disk.
International Journal of Heat and Fluid Flow, 25(2):313 – 319, 2004.

Appendix A

Fabrication of passive nanopillar array on test substrate

The test substrates were made by a collaborate group in University of Pittsburgh, USA. Here we would like to present about their fabrication step and its advantage, so that we will have a better view on the surface properties.

The nanopillar silicon substrates are obtained by inductively coupled plasma reactive ion etching (ICPRIE). This process has an advantage that it directly modifies the surface without adding coating layers that may induce additional thermal resistance to the substrate [156].

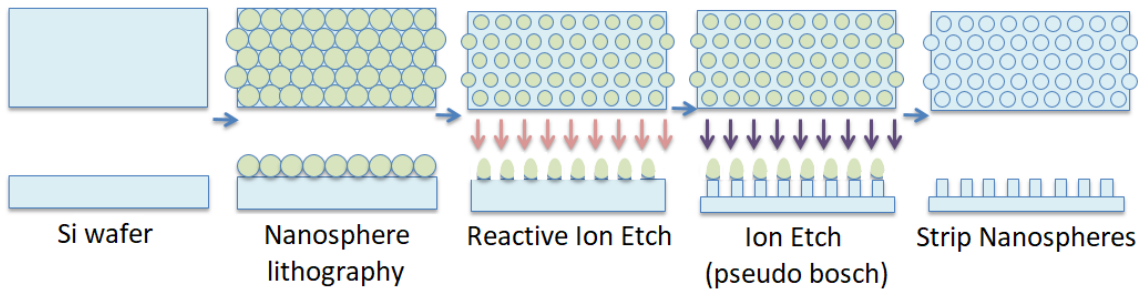


Figure A.1: The fabrication steps of silicon nanopillar pattern.

The fabrication process consists of three steps, (1) manufacture of the etching mask, (2) etching the underlying silicon by ICPRIE, and (3) removal of etching mask. (see Figure A.1.) Polystyrene (PS) nanospheres are utilised to generate the

etching mask. First, a monolayer of nanospheres with the diameter of 800 nm are self-assembled in the air-water interface [157–159]. Subsequently the monolayer is transferred to a P-type boron-doped (100) silicon substrate, which has been cleaned with acetone, methanol, isopropanol and then dried with nitrogen gas. After the substrate is dried in air at room temperature, reactive ion etching (RIE) with oxygen is applied to reduce the diameter of nanospheres to the required size (≈ 440 nm).

After the etching mask is manufactured, ICPRIE is used to etch the silicon substrate to fabricate silicon nanopillars with desired dimensions. During the process, SF_6 and C_4F_8 with optimal ratio of 33:82 are supplied. These gases respectively serve as the etching gas and passivation gas. Different height nanopillars are obtained by varying the duration of this step. It should be noted that when the time duration is longer than 5 minutes the PS mask is impacted and the nanopillar base diameter is different from the etching mask. When the etching is completed, the PS mask will be removed by ultrasonication in acetone for 5 minutes.

Appendix B

Validation of pool boiling data

The validation of boiling setup was made with the bare silicon substrate. It exhibited an average CHF of $15.8 \text{ W}\cdot\text{cm}^{-2}$ and was very close to the prediction (i.e., $15.4 \text{ W}\cdot\text{cm}^{-2}$) of Kutateladze–Zuber CHF model [134], which was calculated by $q_C = C_K \rho_v^{1/2} h_{fg} [g\sigma(\rho_l - \rho_v)]^{1/4}$, where C_K was 0.131 and all fluid properties were at 56°C and atmospheric pressure. The data points of nucleate boiling region also show a good fit with Rohsenow model [133], calculated for saturated boiling of FC-72 at 1 atm:

$$\frac{c_p \Delta T}{h_{fg}} = C_{sf} \frac{q}{\mu h_{fg}} \left(\sqrt{\frac{\sigma}{g(\rho_l - \rho_v)}} \right)^m \left(\frac{c_p \mu}{k} \right)^n. \quad (\text{B.1})$$

where C_{sf} is a coefficient which depends upon the nature of the heating surface–fluid combination. For silicon and FC-72 combination, $C_{sf} = 0.0055$ according to experimental result [160] of Geisler and Bar-Cohen or $C_{sf} = 0.0054$ according to simulation results [161] of Passos et al. The validation result of bare silicon substrate is shown in Figure 4.4, including similar result [132].

Appendix C

Uncertainty analysis for heat flux and wall temperature

The uncertainty of the heat flux measurement comes from three main sources: thermal conductivity of copper, the distance between thermocouples, and the temperature measurement using thermocouples. The heat flux and wall temperature are calculated using the formulae:

$$q = 0.5k_c(4T_2 - T_1 - 3T_3)\Delta x_c^{-1}. \quad (\text{C.1})$$

$$T = T_3 - q(\Delta x_c k_c^{-1} + \Delta x_g k_g^{-1} + \Delta x_s k_s^{-1}). \quad (\text{C.2})$$

The propagated error is therefore estimated as:

$$U_q = \sqrt{\sum_{i=1}^n \left(\frac{\partial q}{\partial a_i} U_{a_i} \right)^2}. \quad (\text{C.3})$$

where a_i is the measured quantity i , and U_{a_i} its uncertainty.

The relative uncertainty of heat flux is calculated as:

$$\frac{U_q}{q} = \sqrt{\frac{U_{T_1}^2 + 16U_{T_2}^2 + 9U_{T_3}^2}{(T_1 - 4T_2 + 3T_3)^2} + \frac{U_{kc}^2}{k_c^2} + \frac{U_x^2}{x^2}} \times 100\%. \quad (\text{C.4})$$

where U_{T_1} is the uncertainty of thermocouple type K at position 1 after careful calibration: $U_{T_1} = a_{thermocouple}/\sqrt{3} = 0.1/\sqrt{3} = 0.06\text{K}$.

Similarly, the uncertainties of thermocouple type K at positions 2 and 3 are $U_{T_2} = U_{T_3} = 0.06\text{ K}$. The uncertainty of thermal conductivity of copper, which depends on temperature, is $U_{kc} = 6\text{ W}\cdot\text{m}^{-1}\cdot\text{K}^{-1}$. The uncertainty of distance between thermocouples is $U_x = 0.01\text{ mm}$. The relative uncertainty of surface wall temperature can be derived using Eq. (C.2) and Eq. (C.3) as follows:

$$\begin{aligned} \frac{U_{T_w}}{T_w} = & \left(U_{T_3}^2 \left(\frac{3k_c R}{2x} + 1 \right)^2 + \left(\frac{U_{kc}\beta}{2x} \right)^2 \left(R - \frac{x_c}{k_c} \right)^2 + \frac{U_x^2\beta^2 + U_{T_1}^2 k_c^2 R^2}{4x^2} + \right. \\ & \left. + \frac{k_c^2 R^2}{x^2} \left(4U_{T_2}^2 + \frac{U_x^2\beta^2}{4x^2} \right) + \frac{k_c^2\beta^2}{4x^2} \left(\frac{U_{kg}^2 x_g^2}{k_g^4} + \frac{U_{ks}^2 x_s^2}{k_s^4} \right) + \frac{\alpha}{4x^2} \left(\frac{1}{k_g^2} + \frac{1}{k_s^2} \right) \right)^{1/2} \\ & \times 100\%. \end{aligned} \quad (\text{C.5})$$

where the thermal resistance of the material layers along heat transfer direction is:

$$R = \frac{x_c}{k_c} + \frac{x_g}{k_g} + \frac{x_s}{k_s}. \quad (\text{C.6})$$

The variable α and β respectively are:

$$\alpha = U_x^2 k_c^2 (T_1 - 4T_2 + 3T_3)^2. \quad (\text{C.7})$$

$$\beta = T_1 - 4T_2 + 3T_3. \quad (\text{C.8})$$

Here, the thicknesses of the thermal glue layer and silicon substrate are $x_g = 0.01\text{ mm}$ and $x_s = 0.5\text{ mm}$, respectively. The uncertainties of thermal conductivity of thermal glue and thermal conductivity of silicon substrate are $U_{kg} = 0.8\text{ W}\cdot\text{m}^{-1}\cdot\text{K}^{-1}$ and $U_{ks} = 18\text{ W}\cdot\text{m}^{-1}\cdot\text{K}^{-1}$, respectively. In Figure C.1, we show all the values of relative uncertainty of all substrates at different temperatures.

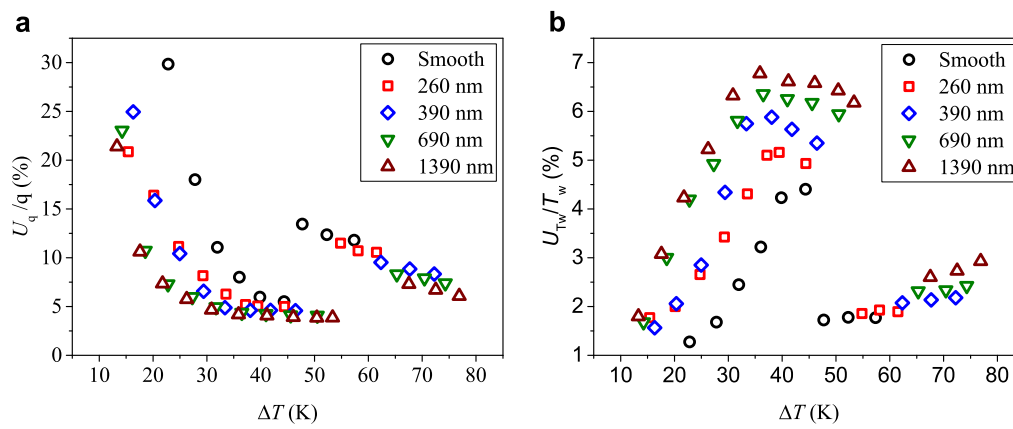


Figure C.1: Relative uncertainty calculated for heat flux (a) and wall temperature (b) at boiling regime.

Appendix D

Bubble departure diameter and releasing frequency at the onset of nucleate boiling

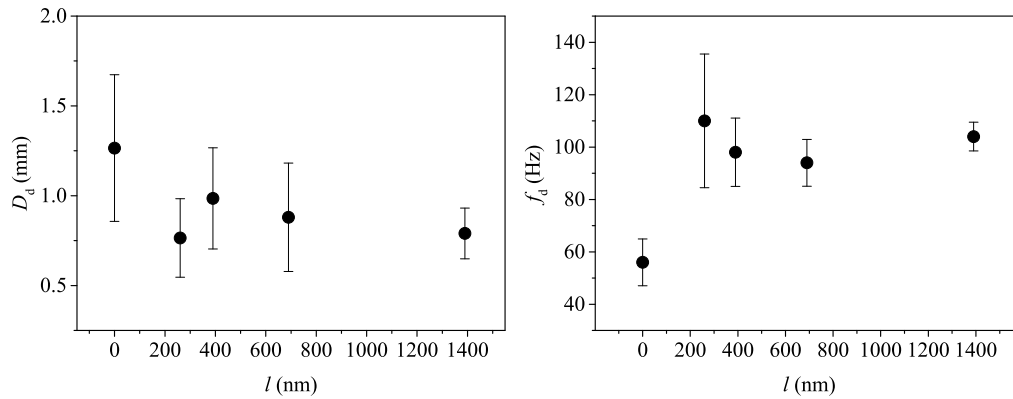


Figure D.1: Dependence of bubble departure diameter and releasing frequency on the height of nanostructures at the onset of nucleate boiling. For the smooth surface, $l = 0$. the departure diameter tends to be smaller for structured surfaces, while there is a significant jump in bubble releasing frequency from the smooth surface to the nanostructured surfaces.

Appendix E

Nanostructure sizes

Table E.1: Size of samples in the experiment with surface area enhancement ratio r calculated for each sample.

Substrate	Pillar height l (nm)	Pillar base diameter D (nm)	Pitch p (nm)	Surface enhancement ratio r
1	257	440	800	1.7
2	391	440	800	2.11
3	691	440	800	2.96
4	1390	440	800	3.52

Appendix F

Relation between the critical heat flux q_c and the spreading velocity

v_s

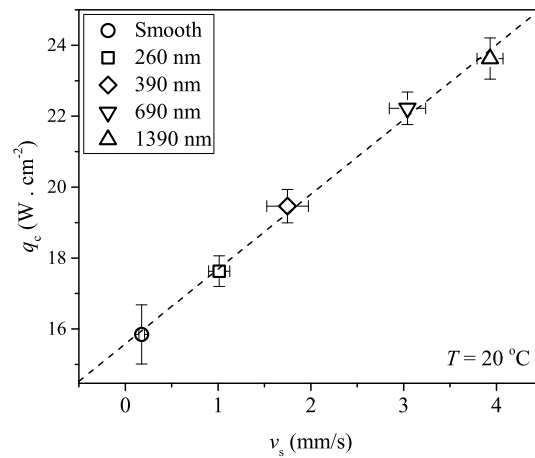


Figure F.1: Linear relation between the critical heat flux q_c and the spreading velocity vs highlighting that the spreading velocity could be used as a key parameter for predicting the critical heat flux for non-polar dielectric fluids with low surface tension, e.g., FC-72.

Appendix G

Extra experiment to measure spreading velocity v_s on heated substrates

In order to measure the spreading velocity v_s of FC-72 on heated substrate substrates, a simple setup has been built as in Figure G.1.

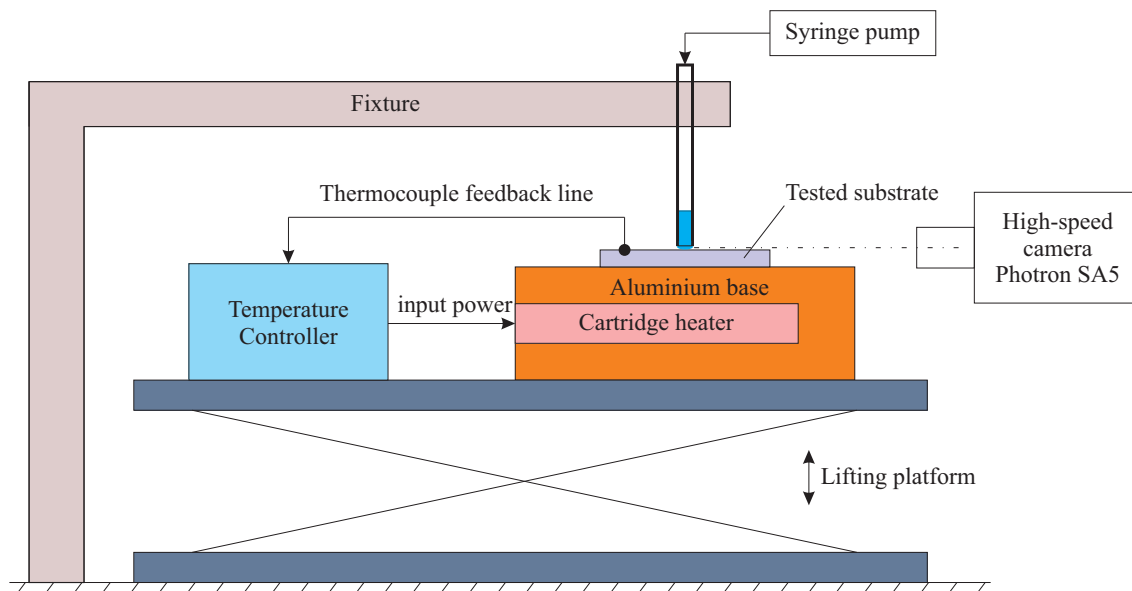


Figure G.1: Experiment setup to measure spreading velocity v_s on heated substrates

An aluminium base embedded by a cartridge heater is used as a heated base for the setup. The tested substrate is heated by this aluminium base and has its surface

temperature monitored by an attached thermocouple. The temperature controller controls the input power applied to the cartridge heater so that the temperature feedback from the thermocouple is kept constant as setting temperature. The whole heating module is putted on a lifting platform, which can be moved up and down during the experiment. On top of the substrate surface, there is a fixed capillary tube (with inner and outer diameter as $350\ \mu\text{m}$ and $500\ \mu\text{m}$ respectively), which is filled with a constant level of FC-72 ($\sim 5\ \text{mm}$) for each experiment by a syringe pump.

Once the substrate surface is stable at setting temperature, it is slowly raised to the capillary tube, which is holding the liquid by capillary effect and forming a pendent droplet on the bottom. When the surface contacts with the droplet, liquid would be spread on the substrate surface and the spreading of three-phase contact line is optically recorded by a high-speed camera (Photron SA-5) at 10000 fps. The recorded images, including position of three-phase contact line along with time, is then processed using Matlab to calculate the spreading velocity of each experiment case. In this experiment, each surface substrate is heated to various temperature levels (20°C , 30°C , 40°C and 46°C).

Appendix H

Uncertainty analysis for heat flux in heat loss measurement

In this section, we present the uncertainty analysis for heat flux in Eq. (3.1). The uncertainty of this measurement comes from three main sources: thermal conductivity of copper, the distance between thermocouples, and the temperature measurement using thermocouples. The average heat flux q_{12} between two thermocouples (at positions where temperature recorded as T_1 and T_2 respectively) is calculated using the formulas:

$$q_{12} = \frac{k_c(T_1 - T_2)}{\Delta x_c} \quad (\text{H.1})$$

The propagated error is therefore estimated as:

$$U_{q_{12}} = \sqrt{\sum_{i=1}^n \left(\frac{\partial q_{12}}{\partial a_i} U_{a_i} \right)^2}. \quad (\text{H.2})$$

where a_i is the measured quantity i , and U_{a_i} its uncertainty.

The relative uncertainty of heat flux q_{12} is calculated as:

$$\frac{U_{q_{12}}}{q_{12}} = \sqrt{\frac{U_{k_c}^2}{k_c^2} + \frac{U_{\Delta x_c}^2}{\Delta x_c^2} + \frac{U_{T_1}^2 + U_{T_2}^2}{(T_1 - T_2)^2}} \times 100\%. \quad (\text{H.3})$$

where U_{T1} is the uncertainty of thermocouple type K at position 1 after careful calibration: $U_{T1} = a_{thermocouple}/\sqrt{3} = 0.1/\sqrt{3} = 0.06\text{K}$.

Similarly, the uncertainties of thermocouple type K at position 2 is $U_{T2} = 0.06\text{ K}$. The uncertainty of thermal conductivity of copper, which depends on temperature, is $U_{kc} = 6\text{ W}\cdot\text{m}^{-1}\cdot\text{K}^{-1}$. The uncertainty of distance between thermocouples is $U_{\Delta x_c} = 0.01\text{ mm}$. In Figure H.1, we show all the values of relative uncertainty of heat flux q_{12} at different temperature for all substrates at boiling regime. The results show that uncertainty of this measurement is below 15% for all substrates at boiling regime.

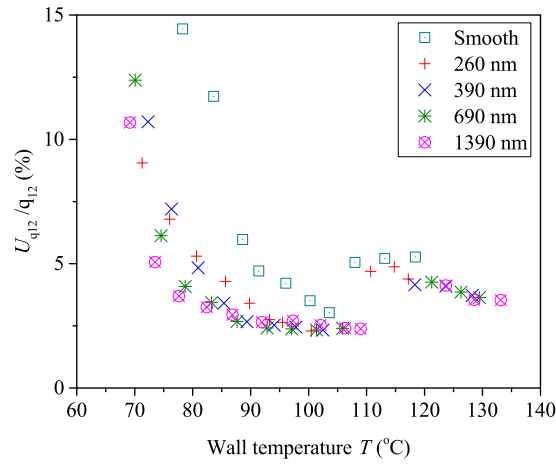


Figure H.1: Relative uncertainty calculated for heat flux q_{12} for all substrates at boiling regime.

Appendix I

Numerical verification for the method used to estimate heat loss

I.1 Method used to estimate heat loss.

In Chapter 3, the heat loss q_{loss} is estimated using the one-dimensional heat conduction model as in Eq. (I.1) to Eq. (I.3).

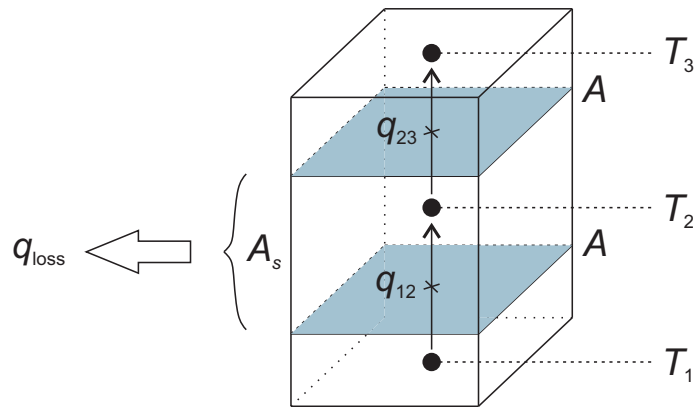


Figure I.1: Schematic drawing of the model: heat fluxes q_{12} and q_{23} are calculated on the shaded area A , whereas the heat loss q_{loss} is considered on four wall area A_s between the shaded area.

$$Q_{12} = k_c \frac{T_1 - T_2}{\Delta x_c} A. \quad (\text{I.1})$$

$$Q_{23} = k_c \frac{T_2 - T_3}{\Delta x_c} A. \quad (I.2)$$

$$Q_{loss} = Q_{12} - Q_{23}. \quad (I.3)$$

$$q_{loss} = \frac{Q_{loss}}{A_{side}}. \quad (I.4)$$

Substitute Eq. (I.1) to Eq. (I.3) into Eq. (I.4), we get the formula to calculate heat loss to the side using the temperature gradient at three points (T_1 , T_2 and T_3):

$$q_{loss} = \frac{k_c}{\Delta x_c} \frac{A}{A_s} (T_1 - 2T_2 + T_3). \quad (I.5)$$

where:

k_c : thermal conductivity of copper, $400 \text{ W}\cdot\text{m}^{-1}\text{K}^{-1}$.

Δx_c : distance between temperature probes, 0.007 m .

A : cross section area of the copper rod, $A = 0.01 \times 0.01 = 10^{-4} \text{ m}^2$.

A_s : total four side area around the copper rod, $A_{side} = 0.01 \times 0.007 \times 4 = 2.8 \times 10^{-4} \text{ m}^2$.

T_1, T_2, T_3 : the temperature at the centre line of the copper rod at different positions, measured by three embedded thermocouples.

I.2 Numerical method to validate heat loss calculation

In this section, we simulate the heat transfer process inside the copper rod with the present of heat loss using ANSYS workbench 19. This is a 3D heat transferring model with all boundary condition values taken from the real experiment (boiling of FC-72 on a bare silicon substrate). Considering a 3D model of the copper rod, these boundary conditions include bottom temperature T_h , heat flux q through the top surface and finally, heat loss q_{loss} to the side.

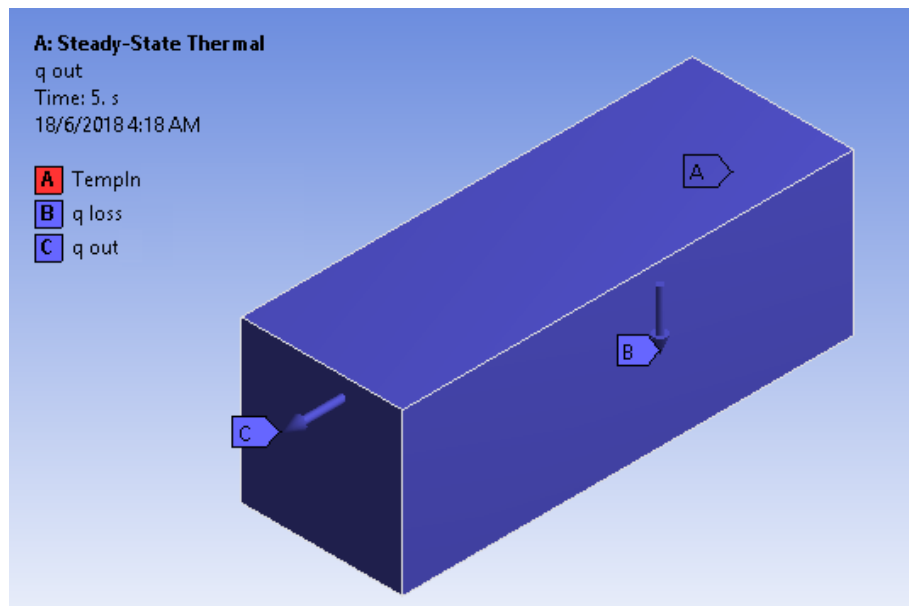
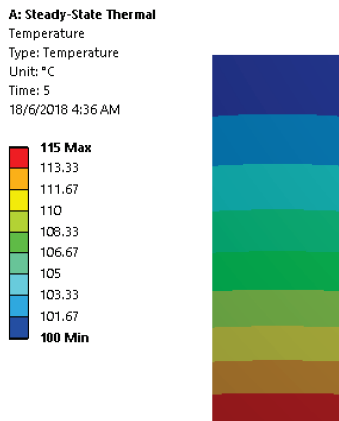


Figure I.2: 3D model of the copper rod with boundary conditions.

The simulation job is solved as a steady state thermal model. The temperature gradient (T_1 , T_2 , T_3) inside the copper rod is then extracted from the solution and is used to calculate heat loss q_{loss} , using the method described in the previous section. (Figure I.3.)

a



b

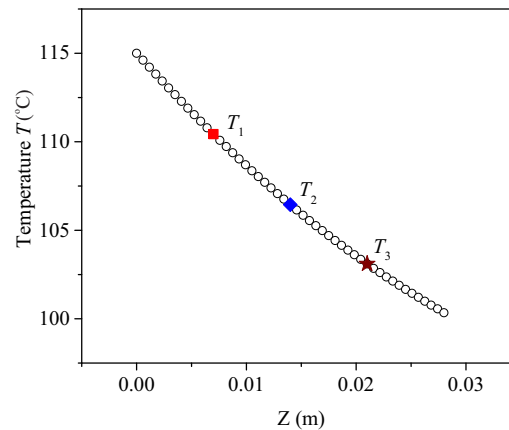


Figure I.3: Simulation result at critical heat flux condition for bare silicon ($q = 15 \text{ W}\cdot\text{cm}^{-2}$, $T = 100 \text{ }^\circ\text{C}$) (a) Temperature distribution on the copper rod; (b) Temperature along the centre line of the copper rod with highlighted T_1 , T_2 and T_3 .

The calculated value of heat loss q_{loss} from the simulation is then compared with the original heat loss inputted to the boundary condition. The results show a high consistency in value of the two quantities as in Figure I.4, which proved that the method used to estimated heat loss is reasonable.

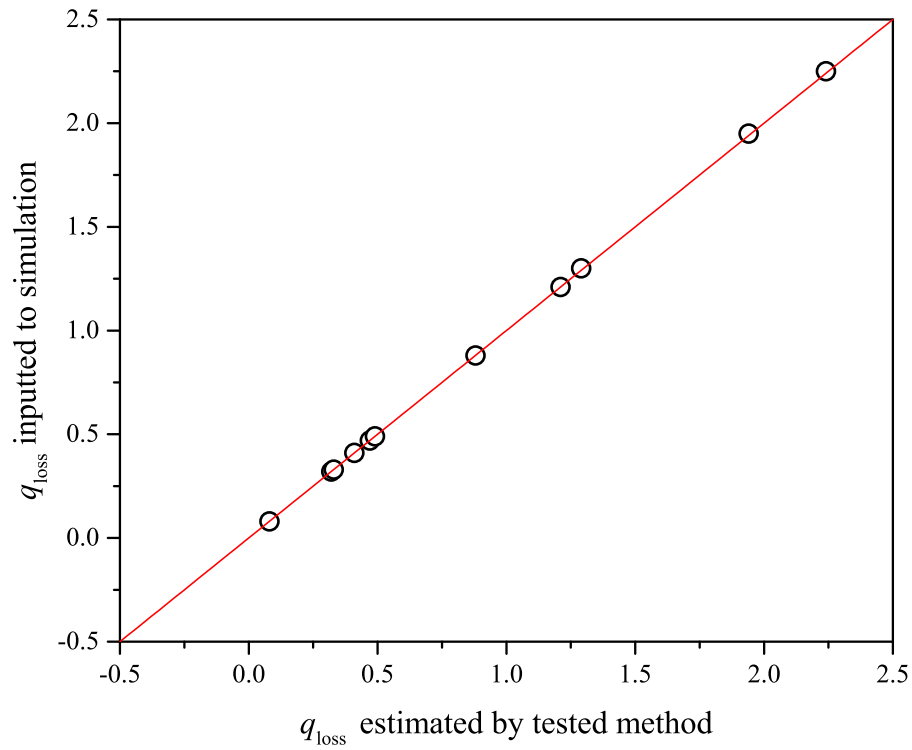


Figure I.4: Validation results for FC-72 on bare silicon substrate: heat loss of simulation model is plotted with heat loss calculated by tested method for various heating temperature.

Appendix J

Sputtering processes used to fabricate microheater

The heater was made by sputtering technique. Here are the detailed steps in the sputtering process:

First, the structures of the micro-heater were designed and printed out on a negative plastic mask. As for microheater design, the plastic mask includes leading wire pattern and micro-heater pattern.

The silicon wafer was prepared with a Plasma-Enhanced Chemical Vapour Deposition process (PECVD) to deposit a thin film of SiO₂ on the silicon surface. This SiO₂ layer allows the metallic film to be stable on the substrate surface. A layer of gold (for the leading wire) and platinum (for the heater) was then deposited on the SiO₂ surface using the Physical Vapour Deposition method (PVD).

The substrate was then spin-coated with a thin layer of SU-8 negative photoresist and was heated until the SU-8 layer is dry on top of the metallic layer. A UV light source was then used to shine through the designed mask onto the substrate coated with SU-8 layer. The SU-8 area on the substrate which is exposed to UV light will become crosslinked and stable. The rest area which was not developed will be easily washed away by acetone. The developed layer of SU8 forms a secondary mask that can be used as a mask to etch the residual metallic film area. The etching process was conducted using etching chemical (HF acid).

After the residual metallic area was etched down to the SiO₂ surface, SU-8 photoresist layer will be washed away by acetone again. Finally, another layer of SiO₂ was sputtering (PECVD) on the hold surface (except a part of the leading

layer) to form a protective layer.

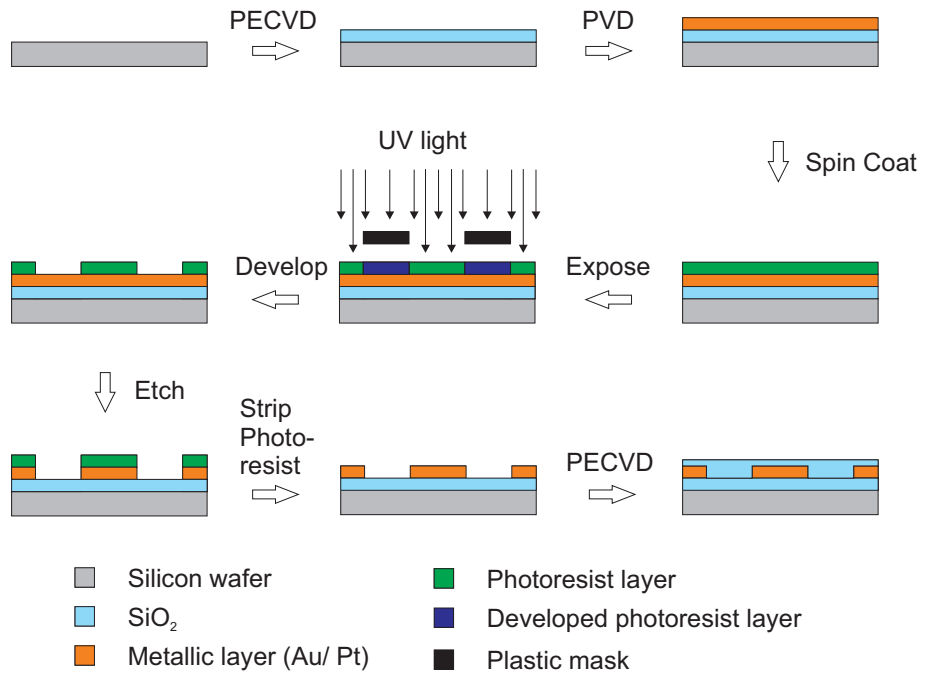


Figure J.1: Sputtering processes used to fabricate microheater.

Appendix K

Fabricating of the microcavity

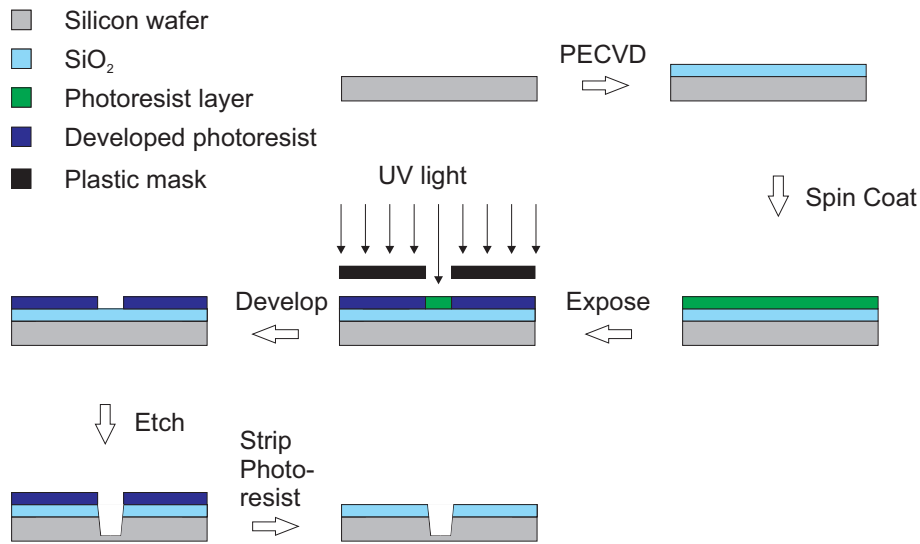


Figure K.1: Etching processes used to fabricate micro-cavity.

The shape of the cavity is an entrusted conical shape due to the etching method. The etching process consists two main steps: mask coating and chemical etching. The mask coating step is similar to that step of sputtering process:

- Design a plastic mask.
- Coat a layer of photoresist (SU-8) onto the substrate surface.
- Shine UV light onto the coated surface through the plastic mask.
- Wash away the unstable layer of SU-8 that is exposed to the UV light.

After that, the substrate with the SU-8 secondary mask will be etched by HF acid. The longer the HF acid is in contact with the substrate, the deeper the cavity

is. If the etching time is too long, the substrate right below the mask will be etched out, that is called over-etching. Due to the nature of the process is corrosion from the top to the bottom of the cavity, its side wall will be tilted a little, making the bottom diameter to be a bit smaller than the top one. Therefore, the shape of the cavity is like an entrusted conical shape, which has a very small tilting angle of the side wall.